DEVELOPMENT OF AN INFRARED THERMOGRAPHY SYSTEM TO MEASURE BOUNDARY LAYER TRANSITION IN A LOW SPEED WIND TUNNEL TESTING ENVIRONMENT

A Thesis

presented to

the Faculty of California Polytechnic State University,

San Luis Obispo

In Partial Fulfillment

of the Requirements for the Degree

Master of Science in Aerospace Engineering

by

Damien L. Horton

March 2021

COMMITTEE MEMBERSHIP

TITLE:	Development of an Infrared Thermography System to Measure Boundary Layer Transition in a Low Speed Wind Tunnel Testing Environment
AUTHOR:	Damien L. Horton
DATE SUBMITTED:	March 16, 2021
COMMITTEE CHAIR:	Aaron Drake, Ph.D. Professor of Aerospace Engineering
COMMITTEE MEMBER:	Paulo Iscold, Ph.D. Associate Professor of Aerospace Engineering
COMMITTEE MEMBER:	David Marshall, Ph.D. Professor of Aerospace Engineering
COMMITTEE MEMBER:	Theodore Garbeff, M.S. Instrumentation Engineer at NASA Ames

ABSTRACT

Development of an Infrared Thermography System to Measure Boundary Layer Transition in a Low Speed Wind Tunnel Testing Environment

Damien L. Horton

The use of infrared thermography for boundary layer detection was evaluated for use in the Cal Poly Low Speed Wind Tunnel (LSWT) and recommendations for the successful use of this technique were developed. In cooperation with Joby Aviation, an infinite wing model was designed, manufactured and tested for use in the LSWT. The wing was designed around a custom airfoil profile specific for this project, where the nearly-flat pressure gradient at a zero pitch angle would delay the chordwise onset of boundary layer transition. Steady-state, RANS numerical simulations predicted the onset of transition to occur at 0.75 x/c for the design Reynolds Number condition of 6.25×10^5. The wing was manufactured from 3D printed aluminum, with a wall thickness of 0.125 inches and a chord length of 13.78 inches. Two central rows of static pressure taps were used, each with 12 functional chordwise locations. The taps were able to generate strong correlation to the numerically predicted pressure coefficient distribution.

The use of an infrared camera visualized and confirmed the presence of boundary layer transition at the chordline location anticipated by the early simulations. To do so, the model was pre-heated such that the differential cooling properties of laminar and turbulent flow would generate a clear temperature gradient on the surface correlating to boundary layer transition. Adjustment of the model's pitch angle demonstrated a change in the onset location of boundary layer transition during the infrared testing. The change of onset location was seen to move forward along the chordline as the aerodynamic angle of attack was increased. Testing with a Preston Tube system allowed for the interpolation of local skin friction coefficient values at each static tap location. Application of both laminar and turbulent empirical assumptions, when compared to numerical expectations, allowed for the qualitative assessment of boundary layer transition onset. Overall, the wing model developed for this research proved capable of producing quality and repetitive results for the experimental goals it was designed to meet. The model will next be used in continued tests which will further explore the use of infrared thermography.

ACKNOWLEDGMENTS

This page is for my family who gave a lifetime worth of work to allow me to be in this position and get as far as I have. Without them, nothing like this would have been possible. To each of my friends, for their support and motivation throughout the past years here at Cal Poly. Dr. Aaron Drake, of course, for willing to take me on as a graduate student and help guide this project in finding success every step throughout. A thank you to Dr. Paulo Iscold for the mentorship you provided in the lab to help foster my growth as a student. To Ted Garbeff, for going out of the way to help advise this project and for the resources you provided throughout. The guys at Joby Aviation—Gregor, Connor and Will—for the collaboration and technical aid to provide the tools and budget to even make this project possible in the first place. I owe a massive chunk of my academic career to the opportunities your group has hosted here at the Low Speed Wind Tunnel. Lastly, a special credit to Cody Thompson for his boundless wisdom and assistance in the development of the model and in keeping our labs together.

TABLE OF CONTENTS

Page

LIST OF TABLES ix

LIST OF FIGURES x

CHAPTER

1 INTRODUCTION 1

2 BACKGROUND 2

2.1 Aerodynamic Fundamentals 2

2.1.1 Laminar v. Turbulent Boundary Layers 2

2.1.2 Natural v. Forced Transition 4

2.1.3 Variation of Coefficient of Friction 5

2.1.4 Heat Transfer Properties 6

2.1.5 Free-Stream Influences 6

2.1.6 Pitch Angle Variation 7

2.2 Principles of Infrared Thermography 8

2.2.1 Functionality of Infrared Cameras 9

2.2.2 Material Properties 10

2.2.2.1 Emissivity 10

2.2.2.2 Thermal Conductivity 11

2.2.2.3 Thermal Capacity 13

2.2.3 Generating Temperature Differentials 13

2.2.4 Image Post-Processing 14

2.3 Experimental Design Methods 17

2.3.1 Factors of Model Design 17

2.3.1.1 Material Selection 18

2.3.1.2 Thermal Capacity 19

2.3.1.3 Internal Geometry 20
2.3.1.4 Applying Heat 21
2.3.1.5 Geometric Designs 23
2.3.2 Visual Measurements 25
2.3.3 Results Validation 26

3 RESEARCH OBJECTIVES 28

4 PAST USE OF INFRARED THERMOGRAPHY IN THE CAL POLY LSWT 30
4.1 The Validation Model 30
4.2 The Ducted Nacelle Model 33
4.3 Shortcomings and Lessons Learned 36
4.3.1 The Use of Insulative Surface Coatings 36
4.3.2 Heating Applications 37
4.3.3 Using the Infrared Cameras 38

5 DESIGN APPROACH 39
5.1 Project Origins 39
5.2 Aerodynamic Profile 40
5.3 Material Selection 41
5.4 Heating Application 42
5.5 Pressure Measurement Validation System 42

6 PRELIMINARY SIMULATIONS 44
6.1 Simulation Build & Settings 44
6.2 2-D Static Pressure Coefficient Distribution 46
6.3 2-D Skin Friction Coefficient Distribution 47

7 MODEL DESIGN 49
7.1 Mechanical Design Goals 49
7.2 Printed Profile 50

7.3 Static Pressure Tap Distribution 51
7.3.1 Chordwise Distribution 51
7.3.2 Spanwise Distribution 53
7.4 Assembly Division 54
7.4.1 Printed Aluminum Sections 54
7.4.2 Cork Thermal Insulators 56
7.4.3 Plastic End Pieces 57
7.5 Test Section Layout 58
7.6 Heating Element Placement 59
7.7 Insulative Coating 61
7.8 Support and Structure 62
7.9 Model Mounting & Pitch Adjustment 65
7.10 Preston Tube for Skin Friction Measurement 66
7.11 Infrared Camera Interior Mount 68

8 MODEL MANUFACTURING 70
8.1 Printed Parts Deformation 70
8.2 Expanding the Aluminum 71
8.3 Support Machining 72
8.4 Static Pressure Tap Repair 75
8.4.1 Static Tap Drilling & Alignment 76
8.4.2 Barb Cutting, Cleaning & Installation 78
8.4.3 End Result 80
8.5 Pressure Line Adapters 82
8.5.1 Part Design 82
8.5.2 Printing & Assembly 83
8.5.3 Quality Check 84
8.6 Center Section Assembly 85
8.6.1 Heating Pad Installation 85

8.6.2 Pressure Tubing Arrangement 88
8.6.3 Bonding Together 89
8.7 Surface Preparation 89
8.8 Vinyl Layup 90
8.9 Cork Insulator Preparation 92
8.10 Mounting & Alignment 93
8.10.1 Alignment Templates 93
8.10.2 Rotating Support 95
8.11 Static Pressure Tap Inspection & Cleaning 96
8.12 Preston Tube Assembly 98
9 DESIGN VALIDATION & CHARACTERIZATION 100
9.1 3-D Scanning 100
9.1.1 Airfoil Profile Comparison 101
9.1.2 Center Section Deflection 102
9.2 Surface Roughness Quantification 103
9.3 Vinyl Layer Thickness 105
9.4 Internal Element Heat Distribution 106
10 TEST METHODOLOGY 108
10.1 Adjusting Pitch Angle 108
10.2 Visual Surface Markings 109
10.3 Infrared Imaging Process 110
10.3.1 Pre-Heating the Model 111
10.3.2 Image Collection Process 111
10.3.3 Image Enhancement & Annotation 113
10.4 Pressure Measurement Process 114
10.4.1 Sampling Configuration 115

10.4.2 Collection Pattern 116
10.5 Use of the Preston Tube 117
11 RESULTS & ANALYSIS 119
11.1 Infrared Thermography Testing 119
11.2 Static Pressure Distribution 122
11.3 Estimating Local Skin Friction Coefficient 124
11.4 Miscellaneous Infrared Imaging 128
12 CONCLUSION 132
13 FUTURE IMPACT 133
REFERENCES 135

LIST OF TABLES

Table		Page
1	Comparison of Objectives between the Two Previously Unaffiliated Research Projects	39
2	List of Mesh Settings Used for the Two-Dimensional Simulations	45
3	List of Solvers and Settings Used for the Two-Dimensional Simulations	46
4	The Chord Station Positions of Each Static Pressure Tap Location	52
5	Comparison of Surface Roughness for Different States of the Wing Model Material Surfaces	104
6	Example Table of Values Recorded for Each Run During Infrared Thermographic Testing	113
7	Sequence of Data Collected for Each Mechanical Configuration Tested	117

LIST OF FIGURES

Figure		Page
1	The Infrared Thermography Wing Model Developed to Study Boundary Layer Transition	1
2	Two-Dimensional Representation of Laminar and Turbulent Boundary Layer Velocity Profiles and Growth Over a Flat Plate	3
3	Illustration of Turbulent Wedges (Right) Forming Due to a Surface Imperfection (Left) on a Finite Wing Model [9]	5
4	Infrared Images of a Finite Wing at 9^{o} Angle of Attack Being Testing at Three Incremental Reynolds Number Conditions [11]	7
5	Infrared Images of Boundary Layer Transition on a Finite Wing with Increasing Angle of Attack [10]	8
6	Block Diagram of an Infrared Sensor's Measurement-to-Signal Conversion Process [13]	9
7	Examples of Microbolometer Sensor Arrays as Installed to Various Infrared Cameras [13]	10
8	Simultaneous Infrared Visualization of an Unpainted (Left) and Painted (Right) Set of Steel Wings Being Tested at M=0.7 [2]	11
9	Black Silicone Rubber Insulator Coating Applied to the Exterior Surface of an Aluminum Wing Model to Increase the Emissivity and Lower the Thermal Conductivity of the Model [9]	12
10	Variation in Infrared Image Clarity as Surface Heat Differential is Increased from Left-to-Right [6]	14
11	A Generic Example of Pixel Remapping to Various Color Schemes (a) Grayscale (b) Cool (c) Hot (d) Hue Saturation Intensity (e) Spring (f) Summer (g) Autumn (h) Winter [13]	15
12	Linear Contrast Enhancement (Left) and Local Histogram Equalization (Right) Applied to the Infrared Image of a Delta Wing Canard Test Model in Mach 1.3 Flow [3]	16
13	Example of Artifacts Created by Advanced Post-Processing Methods Applied to a Delta Wing Canard Model at Mach 1.3 Flow [3]	17
14	An Example Exterior Layup Method Which Blends a Foam Structure with Composite Laminates for Structure, Additional Foam for Insulation and Paint for Emissive Correction [18]	19
15	Infrared Images Showing the Effect of Inducing Additional Surface Roughness (Right) to Accelerate Transition Forward of its Natural Occurrence (Left) [6]	20
16	An Aluminum Infinite Wing Model with Flexible Silicon Rubber Heating Elements Bonded to the Interior of its Exterior Wall [9]	22
17	Comparison of Infrared Images from Use of Heating (Left) versus Cooling to Achieve Temperature Differentials [11]	22

18 (Left) Simple Airfoil Model Developed by the German Aerospace Center DLR for Low Speed Infrared Thermographic Testing [10] (Right) Infrared Thermographic Boundary Layer Trip Testing on the Nose of a Generic Launch Vehicle Model [3] 24

19 Infrared Images of Complex Model Geometries Including a Full Wing Profile from the Chinese Aeronautical Establishment Aerodynamic Validation Model [4] (Left) and a Full Aircraft Model Tested at the NASA Ames Unitary Plan Wind Tunnel [2] (Right) 25

20 Model with Reflective Markers [4] (Left) and a Model with Plaster Markers [21] (Right) 25

21 CFD Illustration of How Flow Around the Validation Model Was Predicted to Forcefully Transition After the Inflection Point 31

22 The Validation Mounted in the Cal Poly LSWT Test Section Using the Same Mounting Arm as the Ducted Nacelle Model. The View Port for the Infrared Camera was Located Above the Model 32

23 White-Hot Infrared Image of the Validation Model Demonstrating Boundary Layer Transition at the Anticipated Location 33

24 The Final Iteration of the Ducted Nacelle Model 34

25 White-Hot Infrared Image of the Ducted Nacelle Model Visualizing the Turbulent Disturbances Generated By a Set of Trip Dots But Lacking Conclusive Evidence of a Laminar Boundary Layer 35

26 Forced Boundary Layer Transition Visualized on the Pre-Heated Nacelle Body (White-Hot Region) Under the Influence of the Internal Ducted Fan 36

27 The Airfoil Profile Designed by Joby Aviation for Use in the Infrared Wing Model Design 40

28 Domain Size and Boundary Specifications of the 2D CFD Simulations 44

29 Local View of the Two-Dimensional Mesh Generated Around the Airfoil Part 45

30 The Static Pressure Coefficient Distribution Along the Suction Side of the Airfoil for 0^o, 2^o & 4^o Angles of Attack 47

31 The Local Skin Friction Coefficient Distribution Along the Suction Side of the Airfoil for 0^o (Left) & 2^o (Right) Angles of Attack 48

32 The Cross-Sectional Profile of the Wing Model 51

33 The Chordwise Distribution of Static Pressure Taps and their Respective Numbering 52

34 Prediction of Static Pressure Tap Measured Coefficient of Pressure Distribution Based on Interpolating CFD Data at the Sixteen Known Static Tap Locations 53

35 The Spanwise Distribution of Static Pressure Taps and their Span Station Positions 54

36 Trigonometric Measurement of the Wing Model When Swept at a 45^o Angle Used to Determine Maximum Allowable Span of the Aluminum Center Section 55

37 Division of the Wing Model Showing the Six Aluminum Center Pieces, the Two Thin Cork Insulators and the Two Plastic End Wedges Used for the 0^o Sweep Configuration 56

38 Conceptual Illustration of the Replacement of Plastic End Pieces to Adjust Sweep Angle 58

39 Schematic of the Wing Model, Infrared Camera and Pitot-Static Probe within the Cal Poly LSWT 59

40 Position and Sizing of Internal Heating Elements within the Aluminum Center Section 60

41 Three-Dimensional Representation of the Model Material Stack-Up Representing the Aluminum Wall, the Internal Heating Elements and the External Vinyl Wrap 61

42 Representative Drawing of the Primary Support Rods 63

43 Representative Drawing of the Secondary Support Rod Extensions 63

44 Comparison of Secondary Rod Lengths Based on the Plastic End Pieces Being Used 64

45 Multi-View Representation of the Preston Tube Mount and Assembly Design 67

46 Focused View of the Two Sections of the Preston Tube Mount Body 68

47 The Plastic Printed Part Used to Mount the Infrared Camera Inside the Test Section 69

48 Visualization of the Inconsistency between the Cross-Sectional Profile of the Raw Aluminum Printed Parts 70

49 Profile Mismatch between End Profiles of the Raw Aluminum Printed Parts 71

50 The Turnbuckle Mechanism Used to Forcefully Expand the Aluminum Parts and Remove the Discontinuity Created When Joining Them Together 72

51 Center Boring the Central Steel Support Rods 73

52 Testing the Fit and Length of the Primary Steel Support Rods 73

53 The Final Manufactured Result of the Concentric Threaded Design of the Primary Support Rod and the Interchangeable Secondary Rod Extension 74

54 The Setup Used to Statically Load the Wing Model's Structural Support Rods 75

55 The Static Pressure Tap Barbs Printed Into the Structure of the Aluminum Center Section Parts 76

56 The Rotating Assembly Jig Used to Drill Pressure Tap Holes Normal to the Part Surface 78

57 The Insertion of the Safety Wire into the Interior Thickness of the Stainless Steel Tube 79

58 Visualization of the Loosening of the Safety Wire from Grinding the Second Side of the Stainless Steel Tube 80

59 Distribution of Functional (Green) Versus Irreparable (Red) Static Pressure Taps at All Four Spanwise Locations 81

60 Cross-Sectional Drawing of the Custom-Made Plastic Adapter Body 82

61 Drilling the Central Through Hole in the Plastic Adapter Body Using a Custom Made Jig to Keep the Part Secured in Place and Aligned with the Drill Press 83

62 Sealing the Bottom Union of the Plastic Adapter Body and the Stainless Steel Barb with Glue 84

63 Checking the Pressure Adapter for Blockage by Passing Compressed Shop Air Through It 84

64 Checking a Pressure Line Adapter for Leakage Using a Hand-Held Vacuum Pump 85

65 The Placement of the Internal Heating Element within an Individual Aluminum Print Part 86

66 Final Internal Heating Element Wiring Scheme 87

67 Image of the Revised Wiring Arrangement Being Connected Through the 3-Prong Plug and Tested for Maximum Attainable Steady-State Heat Capacity 87

68 The Arrangement of Pressure Tubing, Adapters and Heating Pad Wires Before Bonding the Aluminum Print Sections into the Unified Center Section 88

69 The Vixen File Visible with the Aluminum Center Section at the Early Stages of the Coarse Material Removal Process 89

70 The Final Exterior Quality of the Aluminum Center Section after Filing and Sanding 90

71 The Crease in the Second Vinyl Layer That Formed on the Leading Edge of the Model ... 91

72 The Wing Model With the Vinyl Coating Applied and All Accessory Parts Installed 91

73 Image of the Cork Insulators After Being Produced by the Laser Cutting Machine 92

74 Organization of the Electrical Wiring and Pressure Tubing Through the Perforations in the Cork 93

75 The Trailing Edge Pitch Angle Markers Made on the Test Section Floor Using a Plastic Template 94

76 The Final Design of the Rotating Support on the Top of the Test Section with the Electrical Connection and Pressure Tubing Routed Outside the Model through its Central Cavity 95

77 The Tape Marking Which Identified Where the Vinyl Coating Was Cut to Expose the Static Taps 97

78 The Exposure of Static Tap Row 2 Following the Removal of the Vinyl Covering in That Area 97

79 The Final, Operation Distribution of Functional (Green) Versus Inoperable (Red) Static Pressure Taps at the Central Two Spanwise Locations 98

80 Tabletop Assembly Used to Flow Test the Internals of the Preston Tube 99

81 The Final Assembly of the Preston Tube 99

82 The Setup Used to Take 3D Scan Measurements of the Aluminum Center Section 100

83 Image Taken During the Process of Scanning the Aluminum Center Section Using the Hand-Held Sensor Provided Alongside the Rendering Software 101

84 Comparison of the Measured Airfoil Profile (Dashed) to the Original Design Profile (Solid) 102

85 Characterization of the Spanwise Deflection of the Aluminum Center Section Based on the 3D Scan Measurements 102

86 The Mitutoyo SJ-210 Surface Roughness Sensor Seen During its Calibration Procedure Using the Precision Sample Provided Alongside It 103

87 Use of the Surface Roughness Meter to Measure the Raw Printed Aluminum (Left) and the Vinyl Covered Aluminum (Right) of the Wing Model Center Section Parts 104

88 Measuring the Layer Thickness of the Exterior Vinyl Wrap Coating 105

89 Infrared Image Taken Approximately 30 Seconds After Powering On the Internal Heat Elements..... 107

90 The Measurement Method Used to Mark the 0.05 x/c Indicators on the Model Surface .. 110

91 Infrared Thermographic Test Setup As Seen from Within the Control Room..... 112

92 Comparison of a Raw Image (Left) to a Contrast Enhanced Image (Right)..... 114

93 Digital Pressure Transducer Connection Scheme for the Static Pressure Distribution Testing 115

94 View of the Pitot-Static Probe Installed in the Test Section Floor Near the Wing Model .. 116

95 Preston Tube Secured to the Surface of the Wing Model 117

96 Close-Up Image of the Preston Tube Mounted with the Probe Tip Above a Static Pressure Tap..... 118

97 Infrared Thermographic Image of the Wing Model at an Effective Aerodynamic Pitch Angle of 0^o..... 120

98 Infrared Thermographic Image of the Wing Model at an Effective Aerodynamic Pitch Angle of 2^o..... 121

99 Infrared Thermographic Image of the Wing Model at an Effective Aerodynamic Pitch Angle of 4^o..... 121

100 Distribution of Coefficient of Pressure Along the Upper Surface of the Wing Model at an Effective Angle of Attack of 0^o..... 123

101 Distribution of Coefficient of Pressure Along the Upper Surface of the Wing Model at an Effective Angle of Attack of $+2^o$..... 123

102 Comparison of Data Using Static Pressure References from the Wind Tunnel Inlet Versus the Floor Mounted Pitot-Static Probe at 0^o (Left) and 2^o (Right) Effective Angle of Attack 124

103 Distribution of Local Skin Friction Coefficient Along the Upper Surface of the Wing Model at an Effective Angle of Attack of 0^o..... 127

104 Distribution of Local Skin Friction Coefficient Along the Upper Surface of the Wing Model at an Effective Angle of Attack of 2^o..... 127

105 Infrared Image of the Wing Model with the Trip Dot Added to the Upper Surface 129

106 Infrared Image of the Wing Model with the Preston Tube On the Upper Surface Forward of Transition Onset (Left) and Behind Transition Onset (Right) 130

107 Infrared Image of the Wing Model with the Two Strips of Vinyl Cut to Expose the Pressure Taps..... 131

Chapter 1

INTRODUCTION

The Cal Poly Low Speed Wind Tunnel (LSWT) has been a consistent source for aerodynamic research and testing throughout the past few decades. Such projects include the exploration of new measurement techniques in addition to supporting corporate-sponsored research endeavors. The intent of this thesis research project was to expand on the methodologies available for future students to measure boundary layer transition in a low-speed wind-tunnel testing environment. In cooperation with Joby Aviation, a wind tunnel model was developed to utilize infrared thermography as a means of measuring boundary layer transition: an experimental practice which utilizes infrared imaging system to visualize boundary layer interactions. This process would be accomplished by measuring the surface temperature differential generated by the varied heat transfer rates between laminar and turbulent flow. The initial focus of the project was aimed at developing the methodology around a model with known boundary layer transition properties. With that, the next step would be to use the model to apply the lessons learned in order to study a more complex, unknown aerodynamic phenomenon.

Figure 1: The Infrared Thermography Wing Model Developed to Study Boundary Layer Transition.

Chapter 2

BACKGROUND

As the exploration of reliable measurement techniques of boundary layer transition on aerodynamic bodies continues to grow, the use of infrared thermography allows for non-invasive and indiscreet detection of boundary layer flows. However, the application of the technique in a low speed wind tunnel testing environment is yet to be thoroughly documented. In order to understand how infrared thermography finds its utility, it is necessary to review the fundamental aerodynamic principles that drive boundary layer transition followed by the distinguishing variables between laminar and turbulent flow. Details were reviewed to gain a stronger understanding infrared thermographic process as well as the factors of mechanical design which allow for the highest degree of image clarity obtainable. Lastly, prior work relating to the use of infrared thermography in wind tunnel-based testing environments is covered to show which achievements are worth building upon in addition to those which are still yet to be proven.

2.1 Aerodynamic Fundamentals

2.1.1 Laminar v. Turbulent Boundary Layers

The boundary layer is defined as the region of fluid flowing over a surface where the velocity relative to the body is below that of the free-stream flow. This effect is commonly visualized through the analysis of a two-dimensional velocity profile that spans from an object's surface up until the free stream region above. The theory of the boundary layer assumes that the lowest point of molecular contact rests stationary at zero velocity relative to the surface of the object. As vertical separation from the surface gradually increases, the velocity of the fluid flow will subsequently increase until a height is reached where the velocity at that vertical profile returns to the free stream velocity of the surrounding flow. This is illustrated in Figure 2 below. The region where the vertical velocity profile above the object surface is less than that of local edge velocity is defined as the boundary layer. The nominal height of a boundary layer is commonly referred to the distance where the local fluid flow velocity has reached 99% that of the

far-field free stream velocity. That point in the profile where the free-stream flow merges with the boundary layer is how the shear layer of the fluid generates, enacting a local tangential stress on the surface of the body.

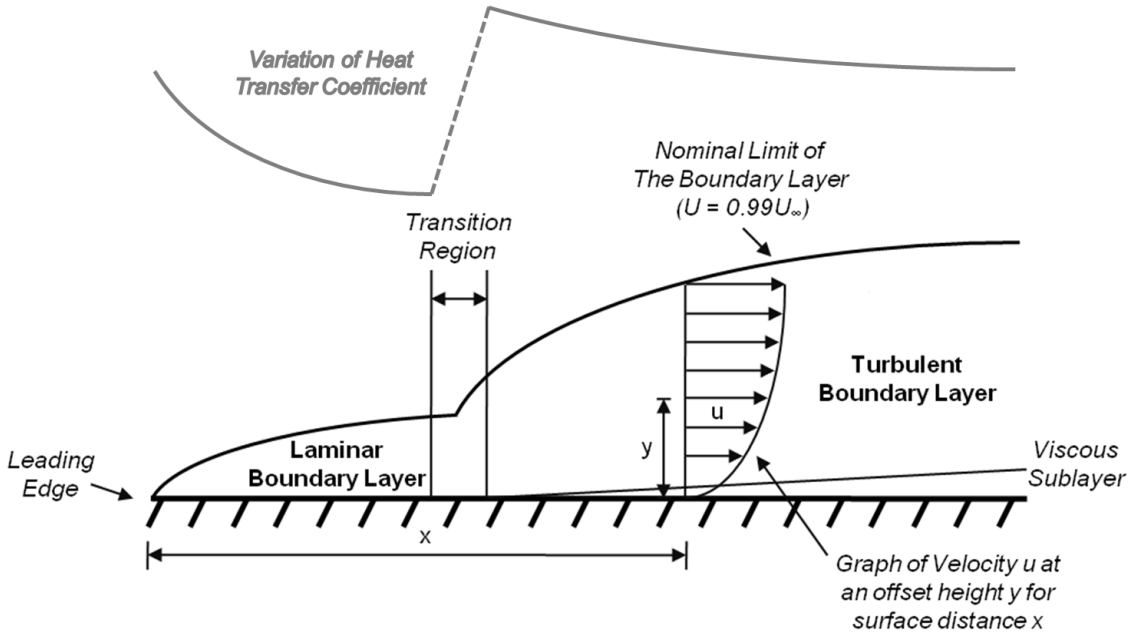

Figure 2: Two-Dimensional Representation of Laminar and Turbulent Boundary Layer Velocity Profiles and Growth Over a Flat Plate.

The effective height of a boundary layer increases as a rate of the length by which it travels along a surface. For engineering practices, empirically-derived equations are used to quantitatively analyze the height of a boundary layer after a certain length traveled, where factors such as the Reynolds number of the flow and the coefficient of friction of the material surface directly influence rate of growth [8].

As the boundary layer continues to develop over an increasing length traveled, the pressure fluctuations within the boundary layer will destabilize and eventually grow large enough to influence the entire height profile, entering a turbulent state [12]. This change is referred to as transition and is not considered to be an instantaneous effect [22]. Instead, the boundary layer will have an intermediate region where the fluid is not yet fully de-stabilized—past the point of purely laminar state but not developed fully enough to become fully turbulent either. The rate by which a

boundary layer develops from laminar to turbulent is mainly dependent on Reynolds number and the coefficient of friction at the surface, as increases in both values will accelerate the rate by which the fluid flow becomes fully turbulent and subsequently decreasing the distance where transition occurs.

From a practical engineering perspective, measuring the location of boundary layer transition onset can be important in aerodynamic design [8]. The performance benefits of laminar flow stem from its relatively lower shear properties which in turn correlate to a lesser friction force exerted on a solid surface, more often known as viscous drag force. To have the tools to predict and measure the location of boundary layer transition can help an engineer better design the aerodynamics of their system to maintain laminar flow along more of the body's surface area and thus decrease the scale of viscous aerodynamic drag being encountered.

2.1.2 Natural v. Forced Transition

Boundary layer flow can be allowed to naturally transition from laminar to turbulent flow if left to develop over a smooth object without any detrimentally adverse pressure gradients. However, a boundary layer is frequently brought to transition through external influence, allowing for the flow to accelerate the onset of turbulent de-stabilization. This process is referred to as forced transition and occurs both through the direct intent of engineers or by uncontrolled means. The most common method of unintentional forced transition is through physical discontinuities on the surface on which the boundary layer is forming. This could be exemplified by dents and scratches on the object's exterior, the collection of ice and other debris particulate, vibrations or even through the influence of upstream aerodynamic structures [22].

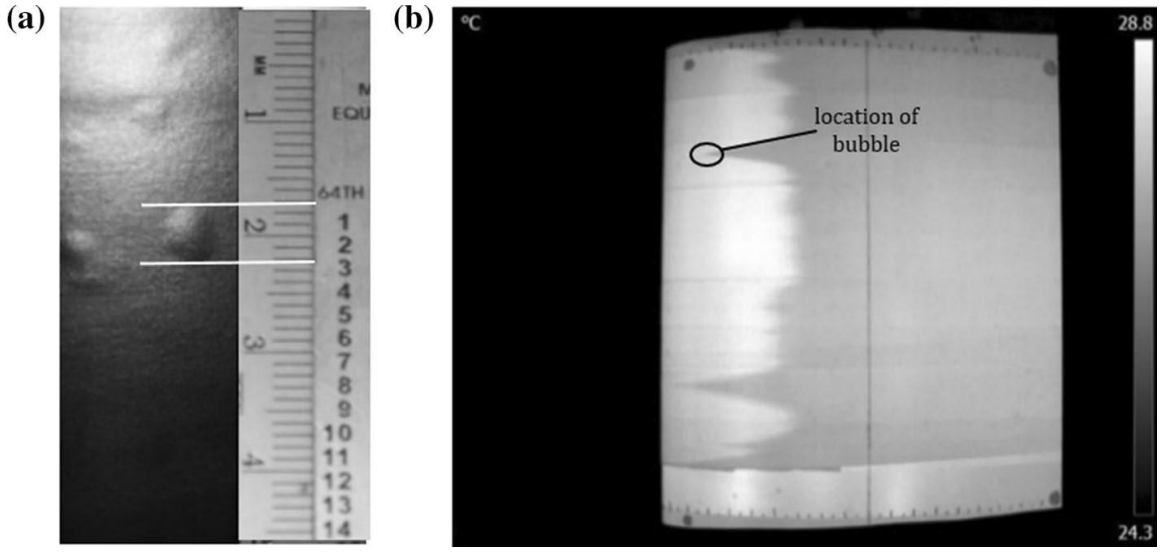

Figure 3: Illustration of Turbulent Wedges (Right) Forming Due to a Surface Imperfection (Left) on a Finite Wing Model. [9]

It is also a common experimental practice to intentionally force boundary layer transition to accelerate the onset of turbulent flow. The most prominent method is through flow tripping, where surface discontinuities are intentionally added to transition boundary layer flow to a turbulent state in a known location. Reasons for doing so might be to delay separation or to increase combustive performance in propulsive systems. The distinction between natural and forced boundary layer transition plays an important role in the use of experimental infrared thermographic systems, as forcing transition can help validate results which indicate the observed presence of natural transition.

2.1.3 Variation of Coefficient of Friction

The defining reason for why laminar and turbulent boundary layers have different drag properties is due to the difference in local skin friction forces generated by the two flow states [12]. The region of transition in a boundary layer creates a large increase in local skin friction forces, which then gradually reduce in magnitude throughout the remainder of the turbulent region. The average skin friction coefficient within turbulent boundary layer flow can be nearly ten times in magnitude relative to laminar flow [12].

When it comes to optimizing a system's aerodynamic performance, the desire to maximize the region of laminar boundary layer flow is often an important priority. The less surface area being wetted by a turbulent boundary layer, the less drag the system as a whole will experience and ultimately improve operating factors such as fuel efficiency or maximum travel speed. The goal of optimizing the location of boundary layer transition is often how infrared thermography finds it usage in the experimental realm. The following section will delve into the logic behind correlations of coefficient of friction and thermal observation.

2.1.4 Heat Transfer Properties

When it comes to experimental infrared thermographic methods, visibly differentiating a laminar boundary layer from a turbulent boundary layer is accomplished through relative surface temperature differentials. This is made possible due to the different convective properties of laminar flow compared to turbulent flow. The local shear stresses of turbulent flow are greater in magnitude relative to laminar flow as it travels over a surface. The increased shear forces result in turbulent flow having an increased convective heat transfer coefficient, as illustrated prior in Figure 2. For that reason, a boundary layer flowing over a heated surface will convect energy from the body at a quicker rate than a laminar boundary layer would. In simpler terms, the difference in the convective heat transfer properties of laminar and turbulent flow allows for an infrared camera to visualize the turbulent region of the boundary layer as a different temperature relative to the laminar region.

2.1.5 Free-Stream Influences

The simplest factor with a predictable influence on boundary layer transition is the Reynolds number of the free stream flow. Classical aerodynamics describes that higher velocity flows will become increasingly more turbulent in nature to the eventual limit where the flow is fully turbulent and the occurrence of boundary layer transition is no longer possible. For flow regimes where the velocity is low enough to still allow for laminar boundary layer flow, a decrease in speed will correlate to a delay in the point of transition. As such, a theoretical flat plate in low speed flow will experience boundary layer transition at a farther length down steam.

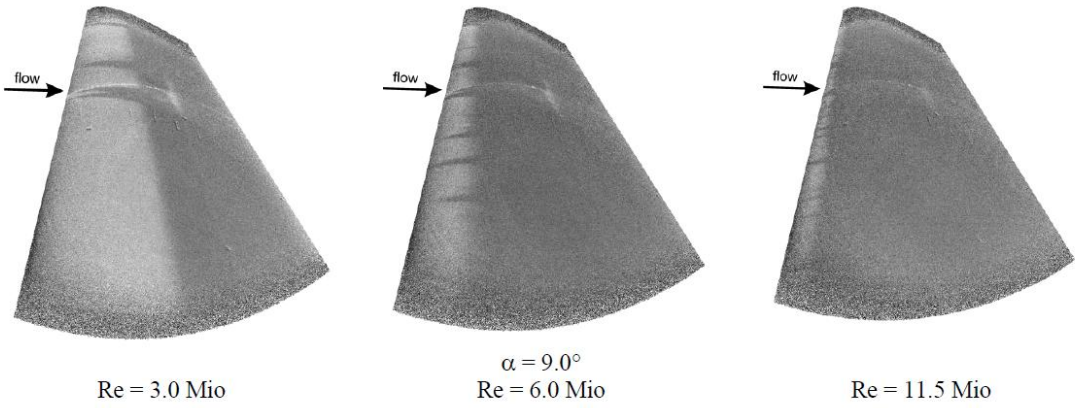

Figure 4: Infrared Images of a Finite Wing at 9^{o} Angle of Attack Being Testing at Three Incremental Reynolds Number Conditions. [11]

Another important factor which characterizes free stream flow is turbulence intensity. Intuitively, an increase in free stream turbulence intensity will have a direct correlation to the increasingly early development of boundary layer transition on the same theoretical flat plate model discussed previously [14]. Both of these factors are important to the successful measurement of boundary layer transition as an excess of just one of the two variables can result in a boundary layer which initializes fully turbulent and has no opportunity to experience transition.

2.1.6 Pitch Angle Variation

For a simple two-dimensional finite wing, the location of boundary layer transition is often a straightforward prediction based on the vast history of published experimental research and analytical modeling. Translations along the pitch axis to change the free stream angle of attack will also have predictable effects on transition: moving the location further forward along the span as the pressure gradient over the leading edge increases in intensity [1].

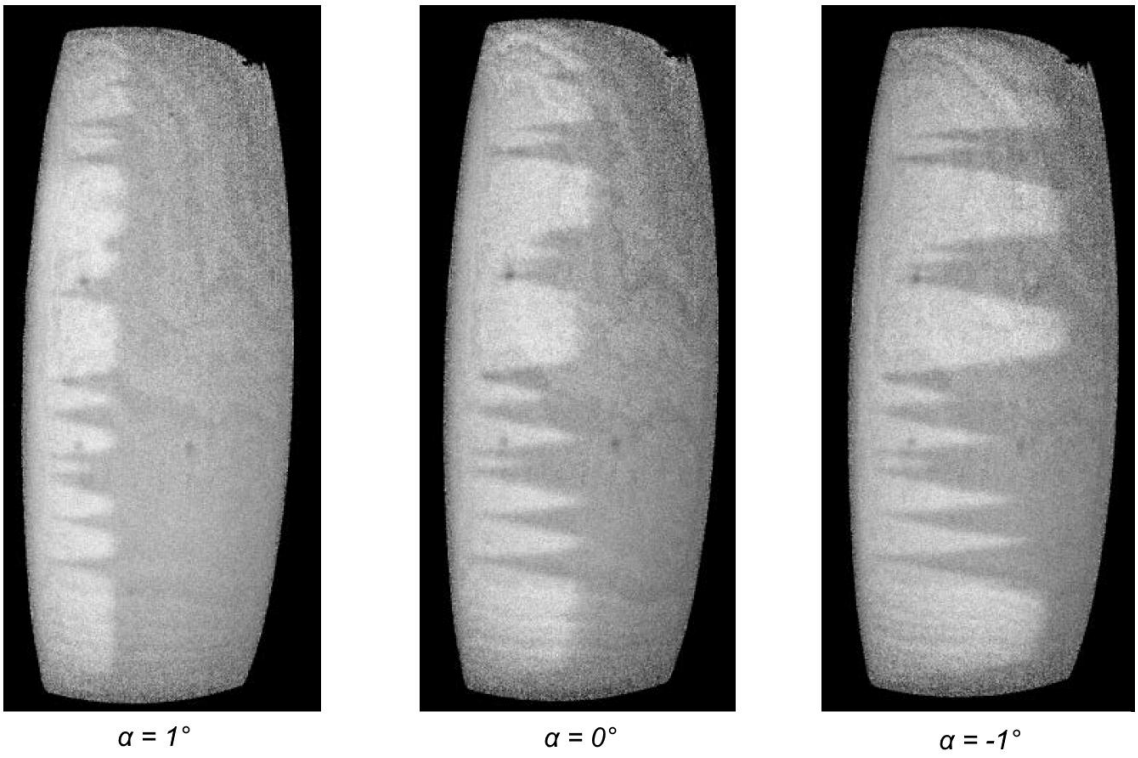

Figure 5: Infrared Images of Boundary Layer Transition on a Finite Wing with Increasing Angle of Attack. [10]

Translations in yaw, also known as sweep variation, has less studied effects on transition. As the boundary layer begins to see influence from cross-flow effects, transition will begin to become more than a simple one-dimensional linear effect [14]. Coupling those factors with other increasingly complex geometric properties such twist or non-constant wing profile sections will only complicate the development and structure of boundary layer transition. Those conditions are often featured in full-scale vehicles where the means to reliably predict transition begin to lose confidence. This is where infrared thermography finds its place in the experimental aerodynamics world—to provide a robust, non-intrusive method for studying boundary layer transition in complex flow fields.

2.2 Principles of Infrared Thermography

The infrared thermography process requires the coordination of multiple elements in order to produce desirable results. The selection of infrared cameras and the thermal properties of the model under study all have important influences on the success or failure of the testing

process. In order to better understand the impact of each element in the process, it is Imperative to review and understand their thermodynamic functionality.

2.2.1 Functionality of Infrared Cameras

Unlike traditional imaging cameras, infrared cameras are designed to capture light on the infrared spectrum (700nm – 1,000nm) rather than within the visible range (380nm – 740nm). To do this, the sensors utilized by most commercial infrared cameras measure changes in reflected infrared energy indirectly through variations of electrical resistance. Each individual sensor within a camera's array is a resistor with a small heat capacity and a high negative temperature coefficient of resistivity.

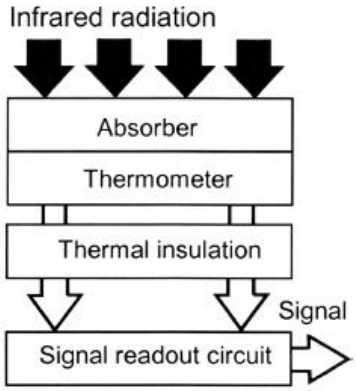

Figure 6: Block Diagram of an Infrared Sensor's Measurement-to-Signal Conversion Process. [13]

As infrared radiation impinges the surface of the resistor, the transfer of heat directly influences the electrical resistance of the element, traditionally made of a thin metallic foil. The lower the material's heat capacity, the more sensitive it will be to increasingly more subtle variations in infrared radiation exposure. These specific types of sensors are referred to as microbolometric detectors and are common for most commercial infrared camera systems. When implemented into a digital imaging system, microbolometers are used in a large array where each element is responsible for capturing each pixel of the final two-dimensional image.

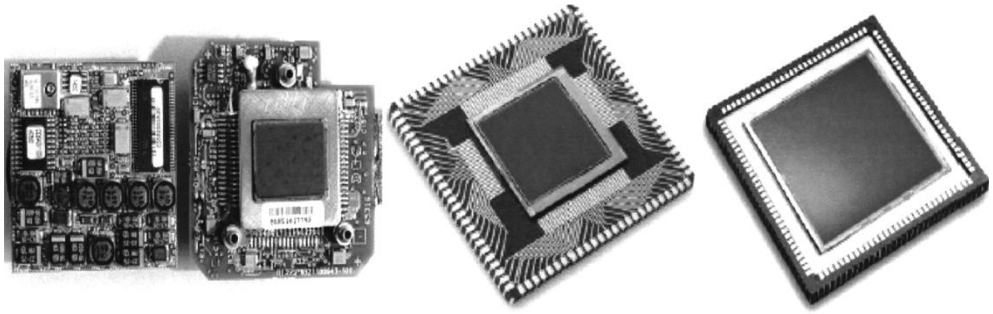

Figure 7: Examples of Microbolometer Sensor Arrays as Installed to Various Infrared Cameras. [13]

2.2.2 Material Properties

Thermodynamic qualities of different materials are already a well-studied set of knowledge that is highly influential on infrared thermographic measurement processes. Just as visible cameras are rely on the reflection of visible light off the surface of a material for its sensors to render an image, infrared cameras rely on a material's ability to radiate infrared energy in the equivalent form of heat energy. Different classes of materials possess different variations of the major thermal properties favorable to infrared thermographic imaging. Metals, organics, polymers and ceramics will all exhibit favorability in some conditions over others relative to the other classes. For usage of infrared thermography in experimental aerodynamic applications, the most important material thermal properties are emissivity, thermal conductivity/diffusivity and thermal capacity [3].

2.2.2.1 Emissivity

The emissivity (ε) of a material is a quantitative measure of the ratio of thermal energy is radiated by the surface (M) relative to the total amount of radiation energy interacting with the material surface (M_B). Emissivity is defined on a range from 0 to 1, where a theoretically perfect black body material that emits all energy absorbed as thermal radiation is defined as having an emissivity of 1 [13]. The property can be considered a near-direct inverse of thermal reflectivity, where a theoretically perfect shiny mirror that reflects all energy with none in the form of absorbed thermal radiation will have an emissivity of 0. For a material to be suitable for use in infrared thermographic studies, high emissivity values are preferred since the effectiveness to emit

thermal radiation will produce temperature variations that are easier for bolometric sensors to discern and, as a result, create clearer digital images.

$$\varepsilon_\lambda = \frac{M(T)}{M_B(T)} \tag{1}$$

Methods for increasing the emissivity of materials used in experimental aerodynamic studies often comes in the form of applying non-reflective surface coatings or by also adding insulating materials on the outer layer [3]. For example, metallic materials almost exclusively used to manufacture high-speed aerodynamic models due to its superior structural properties. However, with emissive values <0.10 for polished metals such as aluminum and stainless-steel alloys, their use with infrared cameras becomes challenging [13]. The addition of non-reflective paint coatings or anodization can reduce the thermal reflectivity of the material and in turn increase its emissivity, allowing for a higher degree of thermal contrast when observed by an infrared camera.

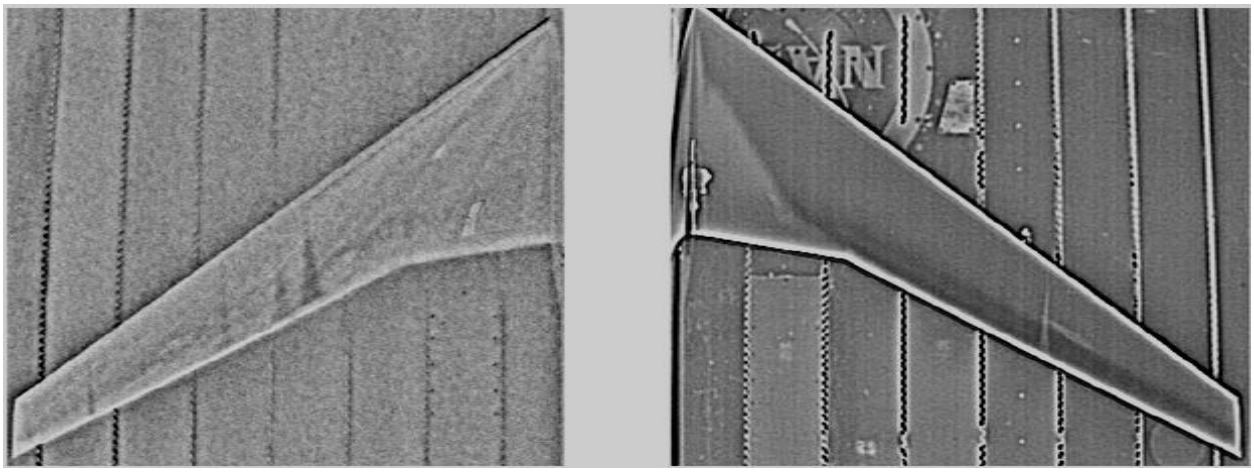

Figure 8: Simultaneous Infrared Visualization of an Unpainted (Left) and Painted (Right) Set of Steel Wings Being Tested at M=0.7. [2]

2.2.2.2 Thermal Conductivity

Thermal conductivity (k) is a more commonly known material property which defines how quickly heat is absorbed (q) by a substance from an energy source. For experimental

aerodynamic applications, the desire for a model to have a low total thermal conductivity is a variable as critical as emissivity. For the purpose of infrared thermography specifically, the benefit of low thermal conductivity comes from the ability to resolve changes in flow features beyond short time spans. When initializing the flow around a model, the temperature differential on the surface which allows for transition to be identified will require some time for the convective properties of the boundary layer to reach a steady-state balance [19]. A model with high thermal conductivity will disperse its stored heat energy too quickly and result in the temperature differential on the model to return back to ambient conditions before quality images can be captured [3].

$$q = -k\nabla T \tag{2}$$

Methods to decrease thermal conductivity are similar to those discussed for increasing surface emissivity. The application of an insulative coating allows for the temperature differential to better manifest on the surface of the model while letting heat disperse into the free stream at a slower rate. The effectiveness of the surface coating is directly related to the thickness of the material as a more voluminous layer will be slower to diffuse heat from the model to the exterior [3]. In addition, materials such as paint layers or polymer layups that natively posses low thermal conductivities will have a similar effect in decreasing the overall thermal response rate.

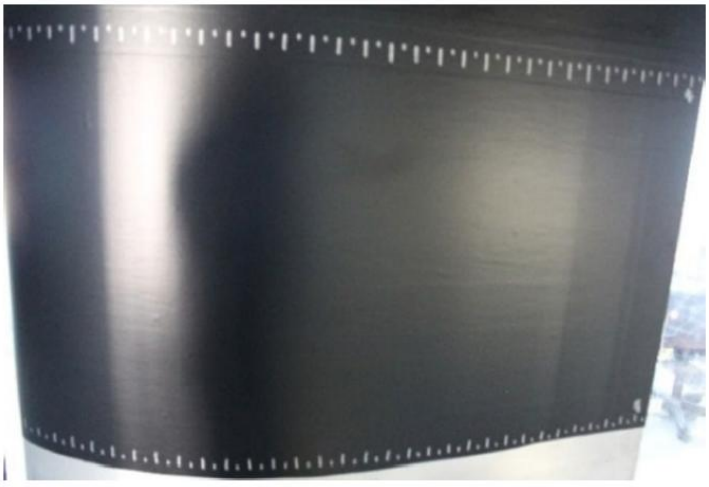

Figure 9: Black Silicone Rubber Insulator Coating Applied to the Exterior Surface of an Aluminum Wing Model to Increase the Emissivity and Lower the Thermal Conductivity of the Model. [9]

2.2.2.3 Thermal Capacity

While the thermal conductivity of a model used in infrared thermographic studies is a major factor in the image acquisition process, the negative effects of higher thermal conductivity can be alleviated through the use of materials with high thermal capacities (C). In essence, a material capable of internally storing large amounts of heat can still continue to provide temperature differentials even when quickly diffusing that energy into the free stream flow [9]. Metallic materials prove ideal for these situations due to their already well-known qualities for high heat capacity. The thickness of the surface layer directly correlates to an increase in thermal capacity due to the upward scaling of volume capable of storing heat.

$$C = \lim_{\Delta T \to 0} \frac{\Delta Q}{\Delta T} \tag{3}$$

Ideally, solid models with no internal open space allows for the greatest degree of thermal capacity. However, if the material has a slow thermal diffusivity rate, then an opposite reaction can occur where the surface layer of the model cools at a faster rate than the internal layers can conduct heat in return. Overall, a fine balance has to be decided when manufacturing models for use in infrared thermographic studies to maximize thermal capacity or, if not a possibility, to offset it with low thermal conductivity rates. Both of those design approaches are ultimately intended to allow the model to retain a temperature differential using its stored internal heat for as long as possible.

2.2.3 Generating Temperature Differentials

In situations of high velocity testing, the flow of air around a model generates enough friction force to naturally heat the model's surface. Coupled with the different viscous properties between laminar and turbulent flow, this process allows for the model to easily show a temperature differential on its surface where boundary layer transition occurs when observed by an infrared camera. However, there is a point when the velocity of the free stream flow becomes low enough where the friction force of the air cannot naturally create a prominent enough heat gradient to obtain usable images [9].

As a result, a test seeking to utilize infrared thermography for low speed testing will require a source of artificial heat to bring the model to a temperature far above that of the ambient background. With a pre-heated model, the convective properties of the boundary layer flow will allow a temperature differential to form on the surface of the model and subsequently indentify transition. In principle, the larger the temperature differential created on the surface of the model relative to ambient conditions the better [1]. This helps boost the signal-to-noise ratio in image data collected by the cameras, as smaller deviations in temperature are harder to discern without post-processing and can be fully obscured by features of greater variation [12].

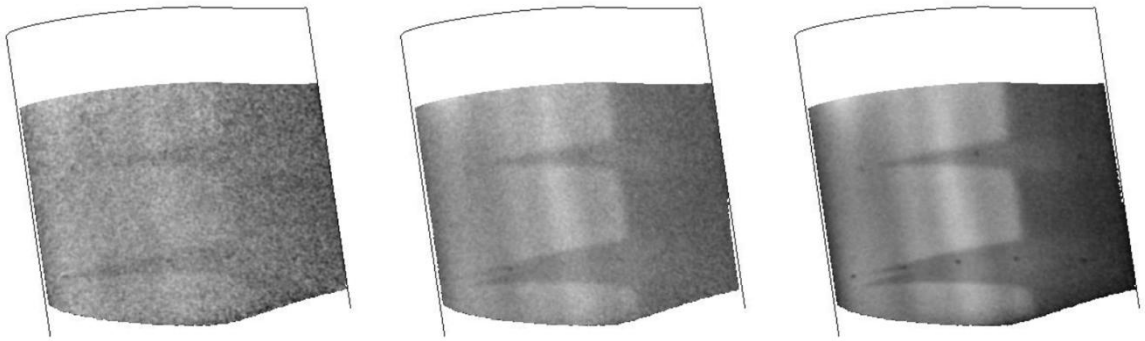

Figure 10: Variation in Infrared Image Clarity as Surface Heat Differential is Increased from Left-to-Right. [6]

For infrared imaging to work in an experimental aerodynamic setting, a temperature differential has to be achieved relative to the ambient environment for the camera to detect differences in boundary layer flow. However, the temperature differential doesn't have to be created by means of model heating—it can also be accomplished through cooling as well [7]. While cryogenic cooling of the model of conditioning of the free stream airflow has been trialed, the vast majority of infrared thermography experiments rely on heating methods instead. This is mostly due to the natural heating tendencies of high speed flow regimes as well as the general availability and ease of use associated with heating technology relative to cooling technology.

2.2.4 Image Post-Processing

Similar to any scientific imaging method, the raw outputs created by a camera might not be sufficient enough for final use. To remedy that, post-processing methods are used to artificially

manipulate the image data to best optimize its outputs for the respectively desired goals. In the case of infrared thermography used in aerodynamic studies, the ultimate goal is to create an image which can clearly identify the smallest flow features on the model possible [2]. While the physical design and heating process bears most of the weight in that process, post-processing methods may still be necessary to enhance the contrast of smaller temperature differentials and remove reflections showing through the surface of the model.

The necessity for post-processing on infrared images occurs in situations where a low emissivity and/or high thermal conductivity of the model results in a less than ideal signal-to-noise ratio of the data collected by the camera's sensors [2]. The signal-to-noise ratio for an infrared camera is influenced by the range of temperatures being detected by the camera where a large difference between the maximum and minimum within the total field of view will out-scale relatively smaller temperature differentials created by flow features on the surface of the model [12]. As the sensitivity range of temperatures presented in the image is scaled upwards to fit the maximum and minimum values detected, the finer differences in between that range will be indistinguishable. This issue is further accentuated when the camera data, natively written as an array of 14-bit integers is compressed to an 8-bit file type that is more conventional for display.

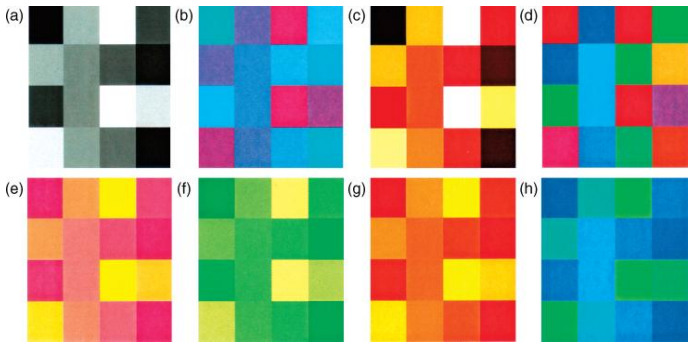

Figure 11: A Generic Example of Pixel Remapping to Various Color Schemes (a) Grayscale (b) Cool (c) Hot (d) Hue Saturation Intensity (e) Spring (f) Summer (g) Autumn (h) Winter. [13]

A common method for infrared image post-processing is to apply contrast enhancement techniques. These are designed to adjust the overall temperature scale of the image to a bound which better captures readings on solely the surface of the model—remapping the 14-bit data to

8-bit data without sacrificing those finer details. The simplest method is to perform a linear remap of the pixel data to apply contrast uniformly through the entire image and shifting away from either the minimum or maximum bounds of the temperature scale. For models of 0.88 emissivity values or higher, a linear contrast enhancement method should provide a more than satisfactory impact [3]. Increasingly sophisticated methods such as cumulative distribution functions or local histogram distributions offer additional mathematical schemes to methodically scale the image data and produce the most detailed final product possible. For models with a specifically low emissivity of 0.60 or less [3], the subtraction of wind off reference images can also be of benefit as long as the temperature of the ambient background does not chance much during the test run.

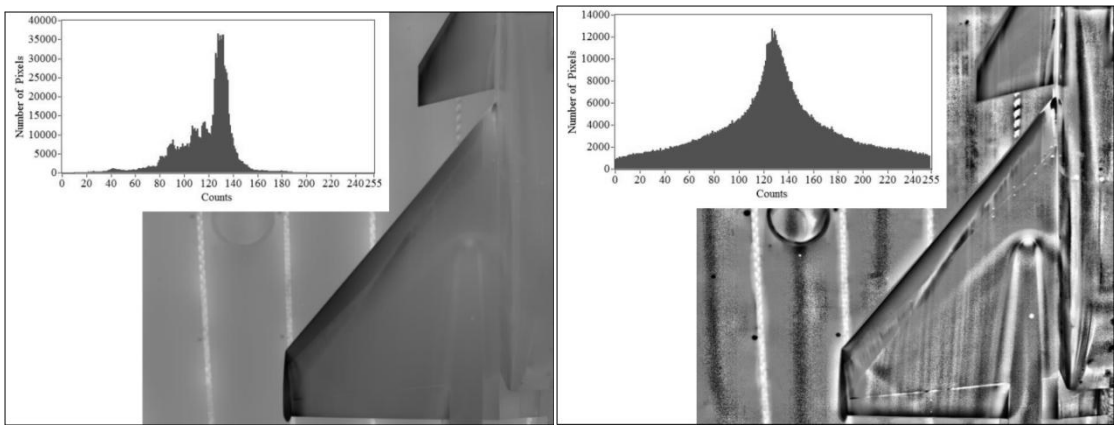

Figure 12: Linear Contrast Enhancement (Left) and Local Histogram Equalization (Right) Applied to the Infrared Image of a Delta Wing Canard Test Model in Mach 1.3 Flow. [3]

A major issue associated with the aforementioned methods is that the artificial shifting of pre-collected sensor data can create artifacts within the final image that represent features absent in the reality of the test [3]. Such an effect can create misleading images that suggest the presence of non-existent flow phenomenon that was only a by-product of post-processing techniques not fit for the situation at hand. However, if the image processing methods are executed properly, the benefits of the effort can be well worth the investment. Nearly all professional infrared thermographic testing relies on post-processing of some sort to gain valid results, although the level of intricacy required will always vary from test to test.

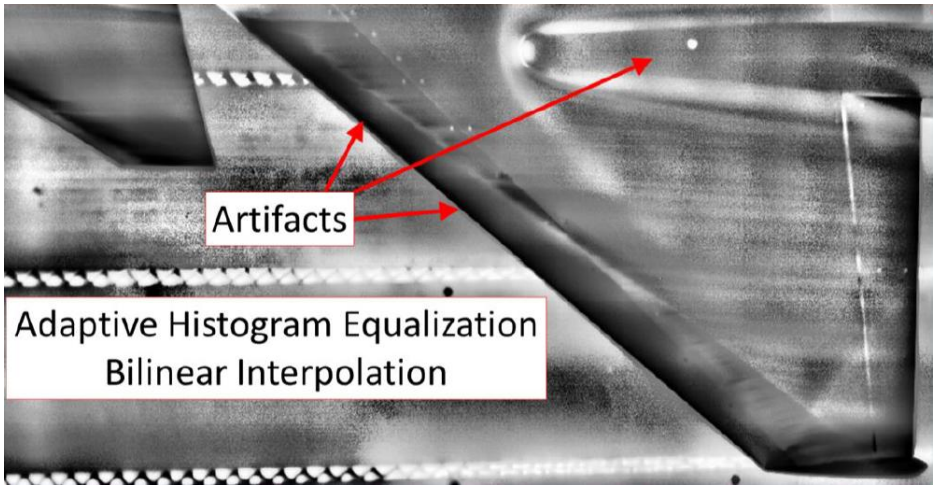

Figure 13: Example of Artifacts Created by Advanced Post-Processing Methods Applied to a Delta Wing Canard Model at Mach 1.3 Flow. [3]

2.3 Experimental Design Methods

2.3.1 Factors of Model Design

The design of a wind tunnel model intended for use with infrared thermography is susceptible to a slew of factors which can make or break its successful use with the method. The development and manipulation of boundary layers is already a complicated subject on its own where variations of free stream and geometric qualities can drastically influence the development of transition and potentially remove its occurrence all together. Additional factors related to the design of the model are also numerous in quantities. Material selection, surface preparation and even the internal geometry has to be considered for its potential effects on the infrared camera. The method by which a temperature differential is instilled in the model as well as the post-processing and results validation techniques used during testing are further important factors in the process. Overall, the development of a model design and testing setup for infrared thermographic applications is a delicate process which requires the attention and balance of a wide variety of variables at every stage of the process. Although some are more consequential to the process compared to others, the successful use of infrared thermography nonetheless depends on thorough planning in all regards.

2.3.1.1 Material Selection

Models used for high speed testing are almost exclusively made from metallic components, specifically aluminum or stainless steel. This is largely due to the structural loads associated with testing in high speed flow regimes and thus the stiffness and strength benefits that metals can offer. However, models designed for testing in low speed conditions allows for a more diverse list of suitable build materials. Without considering constraints of model geometry or manufacturing limits, candidates for model construction include woods, composites as well as polymer plastics or resins. When designing a low-speed wind tunnel model, the selection of a primary build material will be an important part of the infrared thermographic process. As discussed in Section 2.2, factors such as emissivity, thermal conductivity and thermal capacity will vary greatly depending on the material used and can make or break the quality of infrared images produced during testing. Additional considerations for material survivability due to structural and thermal loads will also be factors to balance throughout the design process.

For example, a model printed of plastic from stereo lithographic methods may have low rates of thermal conductivity but will deform when heated and ultimately be rendered unusable for testing. Composite builds would alleviate the structural concerns posed by polymer-based materials but then in turn would suffer from a high thermal conductivity and a thermal capacity, making the image acquisition process difficult if not unsustainable due to rapid heat loss. The ideal model design for use in infrared thermographic processes would achieve a delicate balance of high emissivity and low thermal conductivity to maintain a temperature differential greater than the ambient environment and in turn reduce the overall signal-to-noise ratio detected by the camera [21]. Current research has proven that nearly every testing scenario requires a hybrid blend of build materials and surface coatings to reliably achieve that goal of creating a suitable platform for infrared thermographic research.

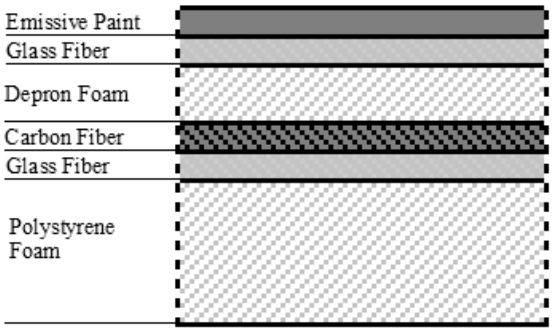

Figure 14: An Example Exterior Layup Method Which Blends a Foam Structure with Composite Laminates for Structure, Additional Foam for Insulation and Paint for Emissive Correction. [18]

2.3.1.2 Thermal Capacity

Although heat retention is a vital part of a successful infrared thermographic operation, the basic aerodynamics of the model also needs to receive a similar level of planning and care. A model made with a surface quality riddled with discontinuities or a particularly high roughness will disrupt the aerodynamic qualities required for a boundary layer to naturally experience transition. As typical in wind tunnel testing, turbulent effects should be driven primarily by the geometry of the model alone to allow the results to resemble that of a full-scale prototype as closely as possible. Deviations in surface preparation such as a coarse, unpolished exterior finish as well as the presence of unplanned recessions or protrusions on the order of over 25 micro-inches [2] will influence the boundary layer enough to accelerate transition at any earlier point than where it would normally occur [6]. Any model being developed for use in infrared thermography will have to maintain a precise and carefully treated exterior in order to produce boundary layer transition effects that are dependent solely on the geometry of the model and not its construction processes.

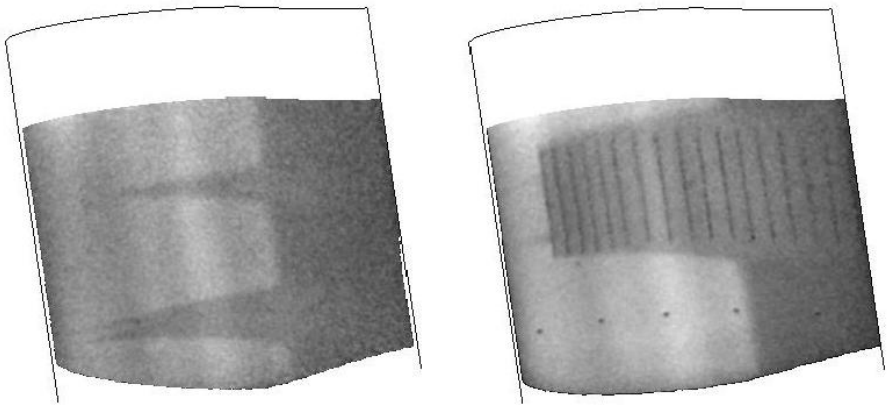

Figure 15: Infrared Images Showing the Effect of Inducing Additional Surface Roughness (Right) to Accelerate Transition Forward of its Natural Occurrence (Left). [6]

2.3.1.3 Internal Geometry

Although aerodynamic effects are only visible on the exterior of a model, infrared cameras have sensitivities high enough to be able to differentiate thermal variations from the internals of a model as well. Take a structural cross-brace, for example. At a vertical projection where an infrared camera is pointed, the surface of a model (assuming some degree of hollowness) will have a uniform wall thickness in all areas except for where the cross-brace is located. The effective wall thickness of that specific region is far greater than that of the surrounding body. As a result, heat will diffuse through the model and out the surface at a non-uniform rate. This effect will visualize itself very clearly to the camera where it will be able to see a discontinuity in the thermal gradient where the cross-brace lies despite not being visible from the exterior.

That type of effect can become problematic for infrared imaging as physical entities lying within the internals of a model might influence the thermal image being captured by the infrared camera [1]. These artifacts, when introduced into an image, can be mistaken for non-existent flow features. In addition, should a real flow feature overlap the discontinuous region, the issue can pose for a difficult and unclear visualization of that flow feature. Design methods which prevent internal geometries from becoming visible through the model's exterior surface closely correlate

to the methods which assist with heat retention. An increase in surface wall thickness allows for a slower conductive rate while also making it difficult for heat from internal geometries to diffuse through to the surface. The use of materials with low thermal conductivity or the addition of insulating layers can also further prevent the visualization of internal features by the camera.

2.3.1.4 Applying Heat

A wide variety of methods have been experimented with to pre-heat models for use in infrared thermographic testing. The two main sub-sets of these methods are direct-contact conductive heating elements and external convective heating arrays. Due to the prevalently minor use of cooling methods to generate a less-than-ambient temperature differential, only active heating will be discussed in this section. In addition, the necessity of these heating methods assumes that the free-stream velocity is not high enough for free stream flow to naturally act as its own heat source.

The most efficient heating method of the two is through the use direct-contact conductive elements. The large majority of models developed for infrared thermographic testing that require active heating utilize a sort of built-in element which can preheat the model before runs. The simplest form of the elements includes silicon-rubber heating elements, which are essentially large flat resistors that generate heat from an applied electrical current [9]. These are often seen to be placed directly under the surface of the model in the region of interest. Additional methods include a carbon nanotube paint layer which allows the outer coating of the model to become a unified, highly-conductive heating element. Similar to the silicon-rubber heating elements, the carbon nanotube paint generates heat by means of electrical resistance when supplied a steady current [11]. Other models accomplish a similar process where the metallic structure is supplied an electrical current directly to warm it by means of the Joule effect [20]. Overall, the most important factor aside from the intensity of heat being generated is also the uniformity of the heating layer.

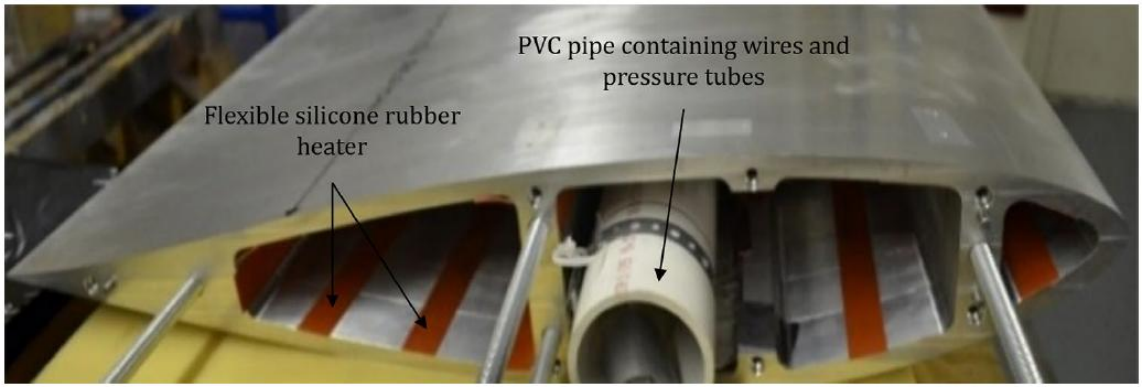

Figure 16: An Aluminum Infinite Wing Model with Flexible Silicon Rubber Heating Elements Bonded to the Interior of its Exterior Wall. [9]

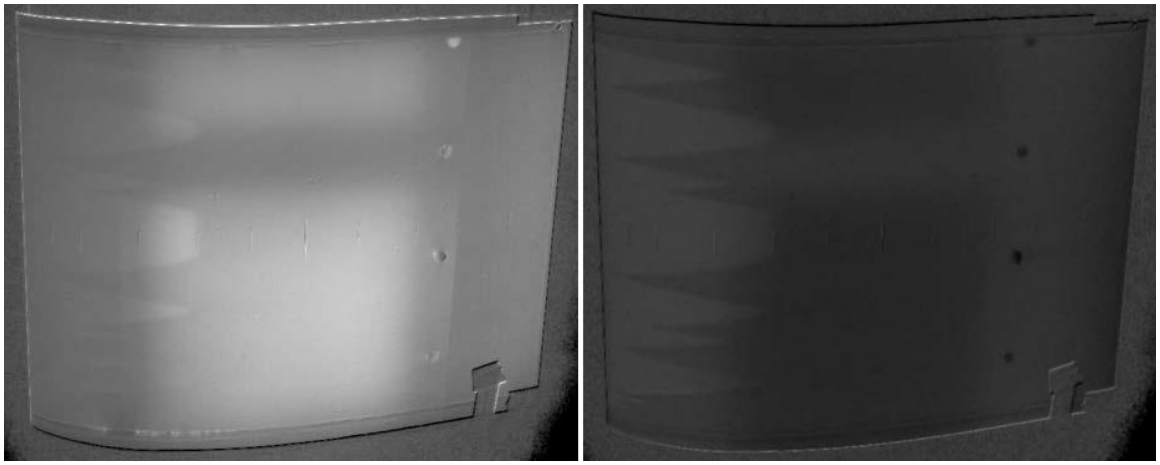

Figure 17: Comparison of Infrared Images from Use of Heating (Left) versus Cooling to Achieve Temperature Differentials. [11]

Naturally, as the camera identifies variations in surface flow based on heat differentials on the model surface, a non-uniformly applied heat layer will clearly be distinguishable by the camera during testing. Similar to the issues posed by internal geometric elements as discussed in Section 2.3.1.3, a non-uniformly heated model will either create temperature differentials which could be mistaken for flow features or possibly even obfuscate features that are actually present. Even with an evenly applied heat layer, a non-uniform outer wall thickness or a discontinuity between materials may also impact the temperature gradient observed by the camera and again posing a similar set of issues. Avoiding these issues requires a careful balance of multiple design variables in order to achieve the best outcome possible.

The opposite method to direct-contact conductive heating is to utilize indirect convective heating methods. Such a process effectively simulates the natural heating effect of high speed flows by artificially conditioning the free stream flow by heating it and allowing it to convect that heat into the model's surface. Due to the different heat convection properties of laminar and turbulent boundary layer flow, this process is still effective as the rate by which the pre-heated air will heat the model differently before and after a region of transition. The equipment used to create this process is often an array of high wattage heating elements which allows heat to be convect into the free stream air prior to reaching the model. A secondary approach to convective heating is to use a similarly high wattage heating element to instead radiate heat directly to the surface of the model, rather than relying on air to transmit the heat from a source far upstream of the model. The convective methods show their disadvantage in terms of efficiency, where the majority of heating power being expended by the elements will not be emitted by the model. However, they do pose a positive benefit of serving as a non-invasive heating method which does not require additional structural or packaging concerns to be factored into the model design process.

2.3.1.5 Geometric Designs

As with any wind tunnel test, the external geometry of the model being used will be fully dependent on the goals of the test being performed. Since infrared thermography is still a somewhat novel development in the experimental aerodynamic community, the diversity of model geometries being published in research is still limited. The vast majority of these models tend to be simple, two-dimensional finite wing elements which have known boundary layer transition effects and can be simple to manufacture. Additional model types include simple axisymmetric bodies where the pressure gradients induced by deviations in the exterior curvature are used to induce transition within the boundary layer. Both of those model types benefit from simplicity due to their intended use of studying and improving upon the process of infrared thermography.

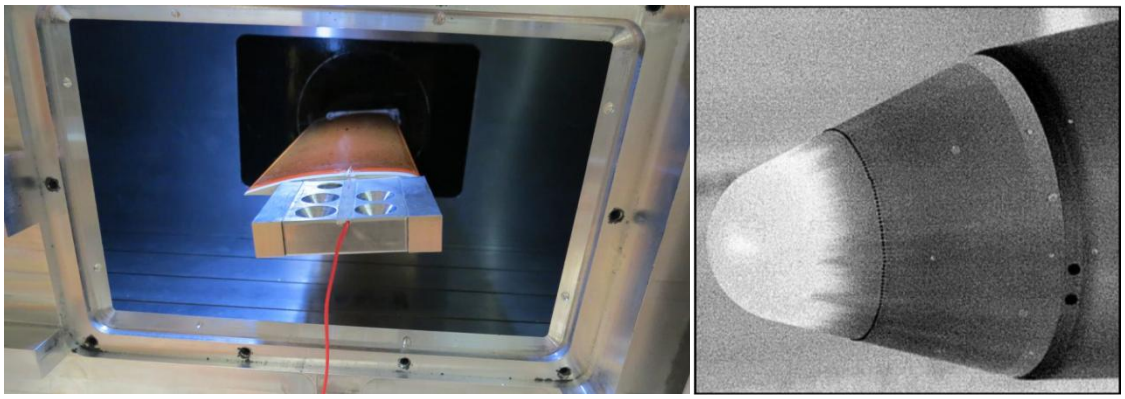

Figure 18: (Left) Simple Airfoil Model Developed by the German Aerospace Center DLR for Low Speed Infrared Thermographic Testing [10] (Right) Infrared Thermographic Boundary Layer Trip Testing on the Nose of a Generic Launch Vehicle Model. [3]

Models of more complex geometries, such as those which resemble the complex geometry of an aircraft wing or even an integrated wing-body assembly representing the full aircraft itself, appear less commonly within the research domain of infrared thermography. While models of this geometric complexity are able to offer more sophisticated aerodynamic flow features they also require significantly more resources to manufacture and integrate to a wind tunnel to the extent of infeasibility for research purposes. To add onto that, the majority of complex model geometries being tested with infrared thermography likely contain proprietary data that the contractor is not looking to publicly disclose, hence the absence in the domain of public research. Models of complex geometry that have been featured in research articles have been near-exclusively standardized models that are developed with the intent of being shared for use among various testing facilities or to act as a well-understood baseline used for internal process development. The eventual goal of all facilities interested in infrared thermography is to apply it towards complex models which resemble systems being developed for actual flight. However, the development and usage of simpler models in order to validate the measurement technique and research the process is an important intermediate step towards achieving that long-term goal.

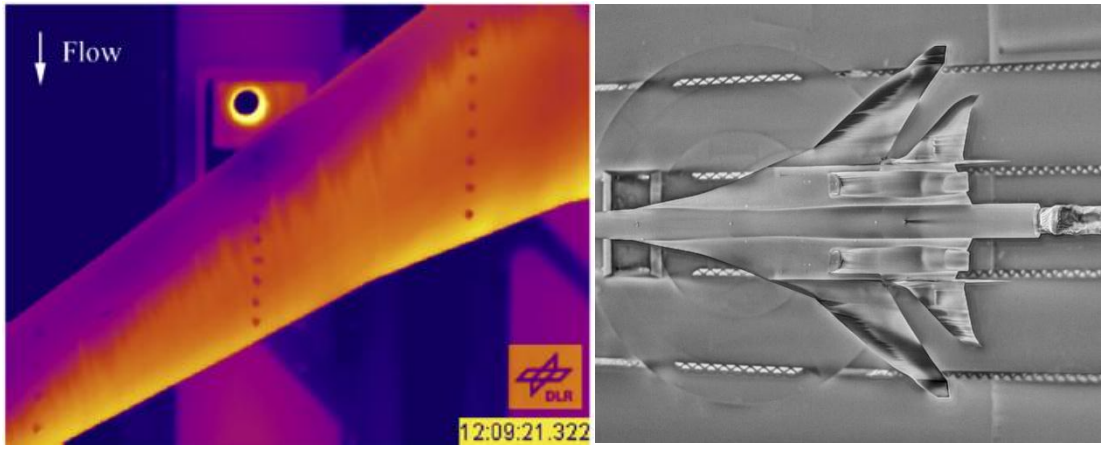

Figure 19: Infrared Images of Complex Model Geometries Including a Full Wing Profile from the Chinese Aeronautical Establishment Aerodynamic Validation Model [4] (Left) and a Full Aircraft Model Tested at the NASA Ames Unitary Plan Wind Tunnel [2] (Right).

2.3.2 Visual Measurements

One concern during the process of identifying transition is to develop a method of being able to measure an exact span-wise location on the model where it occurs. Options for accomplishing that can be done by adding markers made from highly-reflective material or even by filling holes with plaster which allow become visible due to their difference in thermal conductivities relative to the model's body.

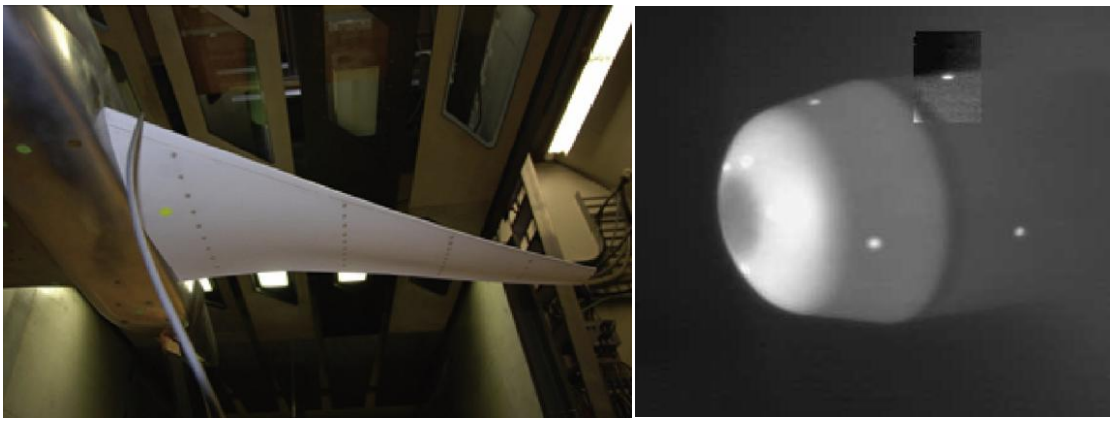

Figure 20: Model with Reflective Markers [4] (Left) and a Model with Plaster Markers [21] (Right).

Since aerodynamic studies only rely on infrared thermography to produce general heat differentials between the model and ambient conditions, cameras do not require any sense of temperature calibration to reach their end goal. The only necessity in calibrating the infrared camera to gather precise temperature measurements is for supersonic and hypersonic studies where reading the heat flux provided by the free stream to the model is desired [7]. For low speed number flows, however, this process is ultimately unnecessary since temperature differentials can be read at any scale given enough contrast relative to the background.

2.3.3 Results Validation

Due to the degree of variability and uncertainty associated with the images acquisition process in infrared thermography, additional means of results validation are a necessity. Factors such as slow thermal response times, presence of infrared reflections off the model surface, visibility of internal geometric features and even artifacts induced by post-processing are all potential sources of error and uncertainty associated with a test. Results validation seeks to perform additional tests under the same operating conditions to definitively confirm identification of aerodynamic features observed during the base testing process.

The most common method for this involves flow tripping, where the boundary layer transition is forced to occur forward of the expected region to validate sightings of natural transition. The principle is that, should boundary layer transition be naturally occurring at some point on the model's surface then the introduction of a flow tripping device forward of that region should remove the presence of the temperature differential originally indicating natural transition. An alternative method to flow tripping, where a variation is introduced on the model's surface, is to instead vary the operating condition of the model itself. This can come in the form of adjusting the free stream velocity (reference Section 2.1.5) or by adjusting the effective angle of attack of the model overall (reference Section 2.1.6). Since the adjustment of variables like velocity and free stream angle of attack have predictable effects on the location of boundary layer transition, they can be utilized as a means of validating initially obtained results.

Alternative methods for validating the identification of natural boundary layer transition include the use of additional sensors to sample the state of the boundary layer independently of the infrared camera. Various types of pressure sensors serve as a simple means for accomplishing this process since a thorough sampling of a boundary layer across multiple flow-wise locations can produce a robust data set capable of differentiating a laminar boundary layer from a turbulent one. The least effort-intensive method would be to use a Preston tube setup where static pressure port data can be coupled with at-surface total pressure measurements to derive wall shear stress directly from dynamic pressure [17]. Specifically in using the works of Poll [16] and Patel [15], this process correlates to the different wall shear stress properties of laminar and turbulent boundary layer flow as discussed in Section 2.1.3. The use of boundary layer rakes adds a vertical component to the sampling process, allowing for measurement of velocity profile growth along the span of the surface from pressure measurement alone. The same goal can be also accomplished with hotwire anemometer probes with the intent of sampling turbulent intensity rather than pressure deviations [18]. The downside of anemometry associates with the complexity for proper usage and analysis required to develop reliable and accurate turbulence intensity measurements.

Acoustic devices, mainly microphones, can accomplish a similar effect as the pressure probes. The use of microphones to listen to sound intensity, a direct correlation to the intensity of pressure fluctuations, can be utilized to differentiate laminar and turbulent regions of a boundary layer [12]. Sublimation techniques or oil film interferometry, similar to surface oil flow visualization, are additional methods design to allow for the measurement of surface skin friction to analyze laminar versus turbulent boundary layer development. Of course, the feasibility of those additional experimental methods will always be dependent on the limitations of the model being used as well as the resources of the facility being tested in. Nonetheless, some sort of validation technique must be utilized to gain absolute confidence in the results being produced from infrared thermographic methods.

Chapter 3

RESEARCH OBJECTIVES

The approach for this research was to design a system capable of using infrared thermography to measure boundary layer transition in a low speed wind tunnel environment, specifically the Cal Poly LSWT. The overarching outcome was solely to expand upon the setup and execution of the methodology rather than exploring any sort of specific unknown aerodynamic phenomenon. Success criteria of this project would be evaluated through the development and expanded understanding of two different aspects of the infrared thermographic process. The first would be the integration of a single heat-generation method which would need to be more robust and uniform than techniques used in prior Cal Poly LSWT infrared tests. The second aspect would be the implementation of a single results validation system which would be capable of qualitatively supporting the conclusions made by the infrared camera.

The geometry of the model would need to be simple and predictable, such that the only unknowns of the research would solely be the performance outcome of the methodology in focus. Should the experimental observations match the expectations provided by preliminary simulations, as well as generating agreement through the use of the chosen validation process, the objectives of this research would be considered fulfilled. For that, an extruded airfoil geometry with known boundary layer transition location would be utilized. The location of boundary layer transition onset would be controllable through pitch angle adjustments—a simple mechanical process with well defined aerodynamic implications.

Testing with the airfoil model would be performed at a constant free-stream velocity condition in order to minimize the amount of dependent variables influencing boundary layer transition. Therefore, the testing process would revolve around configuration changes where only the pitch angle of the model would need to be adjusted in order to vary the onset of boundary layer transition. With the infrared thermographic testing series completed, the implementation of the results validation system would follow, repeating the same test conditions utilized prior to maintain comparability between the two sets of results.

With a goal of allowing this research to influence the success of future infrared thermography projects at Cal Poly, the tools and systems used for the research must be readily available for future students. That is, the methods by which the model would be manufactured and the instrumentation implemented should mostly be based on what is already accessible within the Cal Poly LSWT. An objective to keep the scope of the project tightly-bound to the limitations of the lab would help maintain the relevance and accessibility of this research outcome to be referenced and utilized by other students in the future.

Chapter 4

PAST USE OF INFRARED THERMOGRAPHY IN THE CAL POLY LSWT

Infrared thermography has been used in the Cal Poly LSWT only on two occasions prior to the onset of this project. While it is still relatively novel in this setting, the other projects were able to successfully implement the process to visualize the onset of boundary layer transition, once where it was known to exist at the design conditions and another where the presence of laminar flow was not guaranteed. The shortcomings and lessons learned from those projects helped set a stronger starting point for this thesis—exposing the areas which needed improvement and the aspects by which inspiration could be drawn from proven success.

4.1 The Validation Model

The Validation Model was created with specific, known aerodynamic properties which would diagnose the relative success of the current approach to implementing infrared thermography. The project was started when another, the Ducted Nacelle Model, was struggling to visualize boundary layer transition and sought the use of a known-performance reference model. So although this project does not chronologically precede the one described in Section 4.2, its development was vital to successfully overcoming the issues which prevented the infrared thermography system on the Ducted Nacelle Model from properly functioning.

Designed with the sole intent of validating the infrared measurement process, this model was shaped to induce known and predictable aerodynamic effects. With this, the only unknown would be the ability of its operators to accurately observe the presence of those effects. The model is a simple body of rotation where it was turned at the center to create a “hill and valley” profile, where boundary layer flow will initiate as laminar and then be forced to transition following the first inflection.

The pressure gradient at that point was designed to be adverse enough at a Reynolds Number of 4.8×10^5 such that the boundary layer would be forced to transition at that location, hence providing the model's known aerodynamic properties. A simple CFD prediction of that effect is shown in Figure 21: a scalar view which correlates the presence of turbulent kinetic energy to the onset of forced boundary layer transition.

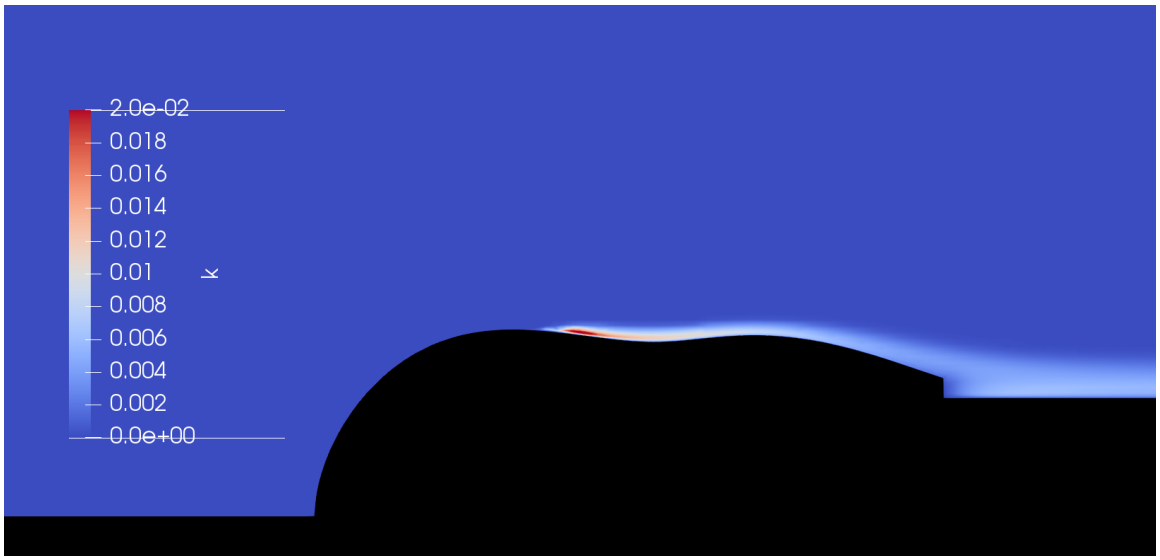

Figure 21: CFD Illustration of How Flow Around the Validation Model Was Predicted to Forcefully Transition After the Inflection Point.

Joby Aviation, the company who sponsored the test campaign of the Ducted Nacelle Model, fronted the design and manufacturing of this model for it to be tested at the Cal Poly LSWT. The 9.5 inch-long part was manufactured by turning a solid aluminum billet to shape and covering it with two layers of matte black vinyl wrap. Those specific materials were chosen to best reflect the construction of the Ducted Nacelle Model, which had an aluminum structure and was covered in an identical surface wrap. The similarity in thermal and emissive properties between the Validation Model and the Ducted Nacelle Model was purposefully intended to provide better comparability to the measurement processes used between them.

Figure 22: The Validation Mounted in the Cal Poly LSWT Test Section Using the Same Mounting Arm as the Ducted Nacelle Model. The View Port for the Infrared Camera was Located Above the Model.

One of the biggest improvements discovered during tests with the Validation Model was the approach by which the model was pre-heated. Previously, a hot air gun was used to convectively warm the surface of models before running the tunnel. This would provide only a small temperature differential from ambient conditions on top of the issue that the uniformity of distribution was notably poor. Testing with this model led to the use of a silicon-rubber heating blanket which was instead used to conductively pre-heat the model. This yielded the capacity for a higher starting surface temperature which proved to be critical in the infrared camera observing boundary layer transition. Following the use of the improved heating method—as well as some small tweaks to the camera's imaging settings—the Cal Poly team was able to successfully identify boundary layer transition at the design-anticipated location. The results seen by the camera were later validated through the use of external boundary layer trip devices as well as surface oil flow visualization.

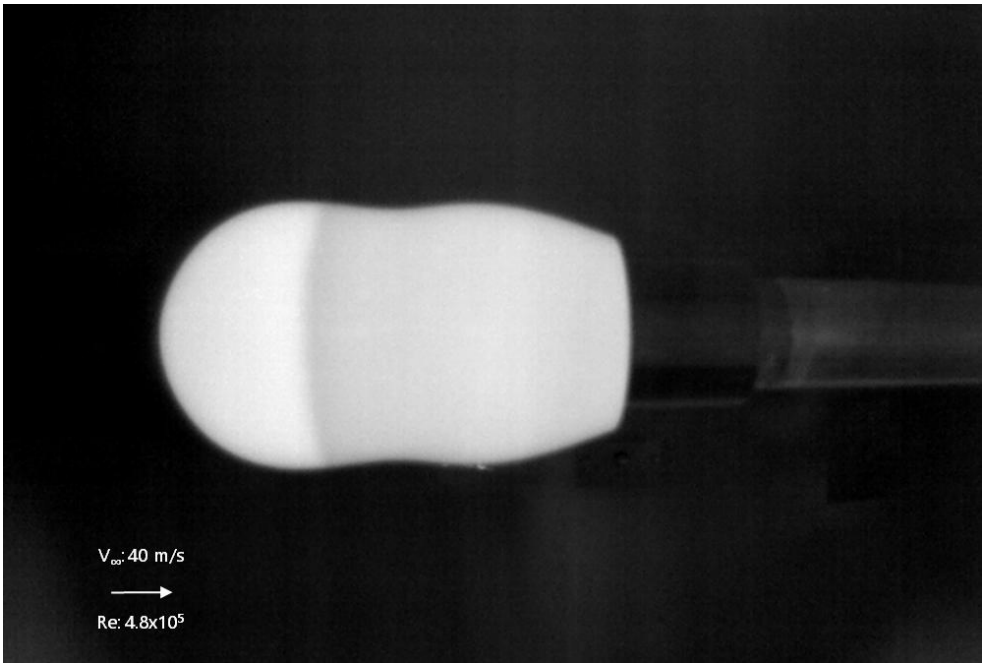

Figure 23: White-Hot Infrared Image of the Validation Model Demonstrating Boundary Layer Transition at the Anticipated Location.

4.2 The Ducted Nacelle Model

Since the acquisition of infrared cameras by the Cal Poly LSWT, the Ducted Nacelle Model was the first project to explore their use in the context of infrared thermography. This project was coordinated through Joby Aviation, who contracted with the lab to develop a model representative of the engine nacelle and propeller cone for their in-development electric aircraft. The main feature of interest on the model was the ducted inlet located in between the propeller cone and the nacelle body—a feature implemented on the aircraft to act as a cooling duct for the motors driving the propellers. Joby Aviation's interest with the testing campaign was to see if the cooling duct could be dual-purposed to ingest the boundary layer from the propeller cone and restart a new, laminar one on the nacelle body intended to reduce drag generated by the system.

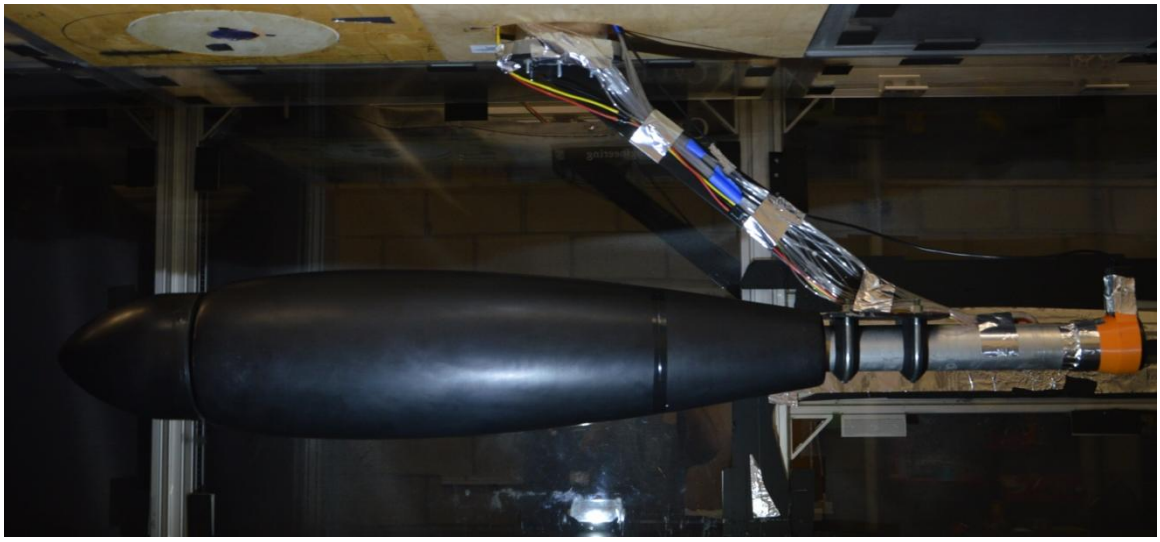

Figure 24: The Final Iteration of the Ducted Nacelle Model.

The Ducted Nacelle Model was designed with a large, hollow aluminum structure which would serve as the region of interest for the infrared thermography process. Aluminum was selected for its known thermal conductivity properties where—coupled with a uniform-thickness shell—heat retention and distribution could be best managed. Initial testing of the model yielded results which were unable to provide conclusive evidence of the presence of laminar flow over the nacelle body aft of the inlet gap, although such effects were visualized on the plastic propeller cone forward of the inlet gap. The model was coated with a layer of matte black vinyl wrap in hopes that the high-reflectivity and low-emissivity of the aluminum shell was disrupting the infrared camera's visualization process. While this proved beneficial in unlocking the ability to visualize the higher-energy turbulent structures from trip dots, boundary layer transition was still yet to be identified.

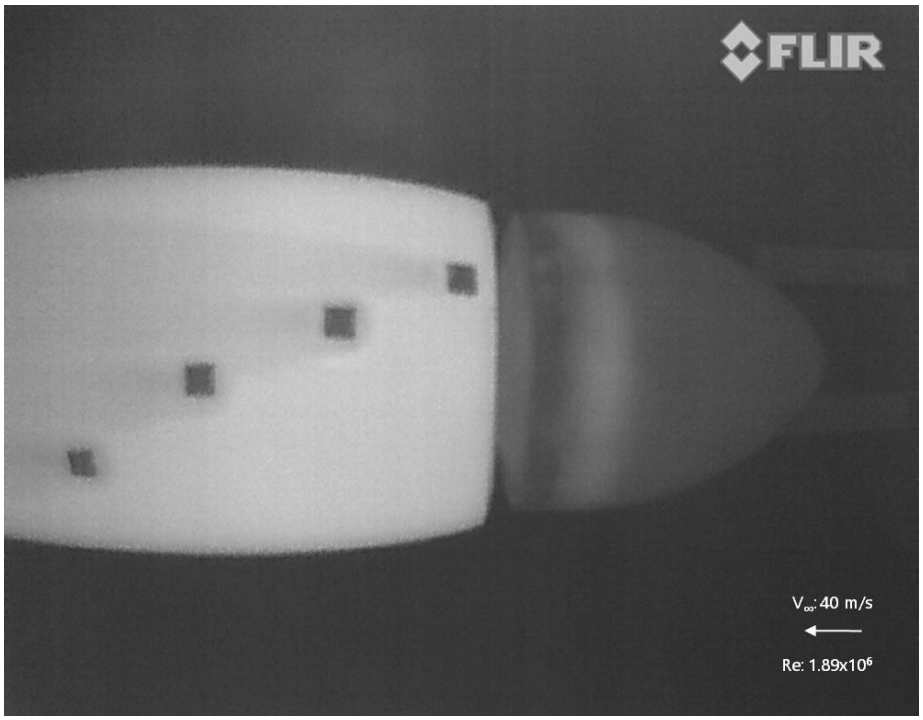

Figure 25: White-Hot Infrared Image of the Ducted Nacelle Model Visualizing the Turbulent Disturbances Generated By a Set of Trip Dots But Lacking Conclusive Evidence of a Laminar Boundary Layer.

At that time, it was unsure whether the model was unable to generate the anticipated aerodynamic effects or if the Cal Poly team's measurement process was incapable of observing the effect in the first place. This dilemma is what initiated the development and testing of the Joby Aviation Validation Model, aforementioned in Section 4.1. Testing of the Validation Model revealed the biggest shortcoming of the process was the method by which the models were being pre-heated. The improved solution involved the use of a silicon-rubber blanket, which could generate higher temperature differentials relative to ambient conditions. Use of this process, where the Ducted Nacelle Model was pre-heated to roughly 100^{o}F, proved sufficient in allowing boundary layer transition to manifest on the nacelle body through sight of the infrared camera (reference Figure 26). This was only distinguishable when the internal ducted fan was operational and ingested the boundary layer shearing off the propeller cone. Without the fan running, no evidence of laminar flow could be visually discerned. This became the necessary proof to conclude that the ducted inlet system was capable of restarting a laminar boundary layer on the nacelle body.

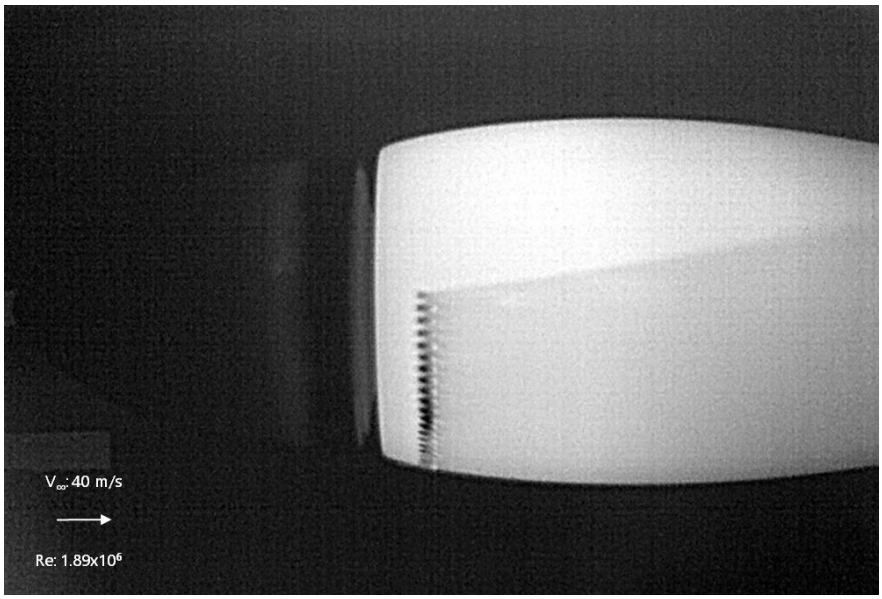

Figure 26: Forced Boundary Layer Transition Visualized on the Pre-Heated Nacelle Body (White-Hot Region) Under the Influence of the Internal Ducted Fan.

4.3 Shortcomings and Lessons Learned

The infrared thermography tests conducted in the past brought forth valuable design and methodology improvements which influenced the design and eventual outcome of the research covered in this document. This section touches upon some of those details which concern the use of insulative surface coatings, improved heating applications and some notes regarding the use of the cameras available to the Cal Poly LSWT.

4.3.1 The Use of Insulative Surface Coatings

One of the most immediate lessons learned from the two infrared thermography tests was the necessity of a proper insulation layer on the surface of a model used for infrared thermography. The vinyl wrap was able to provide a more emissive and less reflective surface for the camera to observe, allowing it to better focus on the thermal profile of only the model rather than the noise of the surrounding environment. In addition to the visual clarity provided by the vinyl layer, it also served as an important thermal buffer between the aluminum and the surrounding airflow. As discussed in Section 2.2.2.2, a material with high thermal conductivity will diffuse heat too quickly for any sort of temperature gradient to form on its surface. Therefore, as

the laminar and turbulent boundary layers try to convect heat at different rates, the stored thermal energy in the aluminum will equalize before that temperature differential can be noticed by an observing camera. While more advanced image processing techniques might be able to circumvent the issue of reflectivity, the addition of the vinyl provided more direct solution instead.

The addition of the vinyl allows for that differential to manifest within the vinyl—a less conductive material—without being diffused out too quickly to be noticed. When testing the Ducted Nacelle model with a bare aluminum surface, the high-energy turbulent wake of trip dots could not be visualized by the infrared camera. However, following the addition of the vinyl, those features became visible as the insulating layer could capture the differential cooling of the generated turbulence. Those two factors alone are the primary explanations for why the addition of the vinyl wrap on the Ducted Nacelle Model was able to create such an impactful difference, even before the changes in heat application were introduced.

4.3.2 Heating Applications

Prior to the development of the Validation Model and Ducted Nacelle Model, there was no precedent as to how much heat was required for infrared thermography to succeed in the Cal Poly LSWT. The use of the conductive heat blanket produced immediate improvements to the infrared thermographic process compared to what was achieved during the unsuccessful use of the hot air gun. The conductive method could heat the models heated upwards of 100^{o}F on their surface, generating a temperature differential great enough to produce enough contrast to visualize boundary layer transition. The expectation there after was that the greater a model can be pre-heated (within the limits of the materials in use), the better the results would appear.

Although the external heat blanket was able to generate more heat than its predecessor method, the Cal Poly team noticed that it was not very efficient at uniformly heating the entire region of interest on the model. Going forward with the next infrared thermography process, the heat application process would need to both follow and improve from the techniques practiced during the Validation Model and Ducted Nacelle Model testing.

4.3.3 Using the Infrared Cameras

An examination of the images shown in Figures 23 and 26 will notice that the infrared images presented are seemingly out of focus. The infrared cameras in possession by the Cal Poly LSWT are systems originally designed for use in aerial applications: long-wave, un-cooled sensors paired with far-focus lenses capable of capturing a wide range of infrared signatures over from a distance. A consequence of using aerial imaging systems in a wind tunnel testing environment is that the set focal distance of the cameras is significantly greater than desired. The camera used for the Validation Model and Ducted Nacelle Model tests does not have the ability to optically adjust its focus and consultation directly with FLIR has revealed that there is no possible way to reconfigure the specific camera in concern. As such, the images captured by the camera—when used in the LSWT—will always appear slightly out of focus. Unfortunately the issue is currently unavoidable however the knowledge of the shortcoming was at least able to become prior knowledge before further projects commenced. Future student groups, however, could benefit from exploring methods for calibrating the cameras prior to testing. This would help alleviate the issues provided by the implementation of the camera into the wind tunnel while also allowing for more comprehensive data analysis.

Chapter 5

DESIGN APPROACH

5.1 Project Origins

Following the successful completions of the Validation Model and Ducted Nacelle Model testing campaigns, another infrared thermography project was commissioned for the Cal Poly LSWT. The primary objective of the project would be to use infrared thermography as the primary means of observing how boundary layer transition behaves as a function of wing sweep.

However, since the objectives set forth for this research were only focused on developing the methodology of infrared thermography, no specific requirement was in place to limit the model selected for use. An overlap in research objectives was quickly noticed between the two projects, as presented in Table 1. As such, an arrangement was made where the responsibility of the model's development would be inherited for use in this thesis research.

Table 1: Comparison of Objectives between the Two Previously Unaffiliated Research Projects.

Infrared Model Design Objectives	
Thesis Research	**Joby Aviation**
Explore the Use of Infrared Thermography to Study Boundary Layer Transition	Explore the Use of Infrared Thermography to Study Boundary Layer Transition
Utilize Materials and Sensors Readily Usable within the Cal Poly LSWT	Study the Behavior of Boundary Layer Transition as a Function of Wing Pitch & Sweep Angle
Utilize a Model with Known Aerodynamic Properties	Learn the Behavior of a Model with Unknown Performance Qualities
Explore and Improve Methods for Heat Application	
Implement a Secondary Validation System	Implement a Static Pressure Measurement System

The resulting agreement was shaped such that the model's design would be adjusted to meet the requirements of this thesis project while maintaining a capacity to fulfill the original requirements of Joby Aviation's interests. Once a final design was completed and agreed upon by both parties the model would be first be used to fulfill the research objectives of the thesis project before finding utility in the original swept angle testing campaign.

The details surround the final design features and development of this model is outlined in the following sections and chapters. In addition, this document solely conveys the experimental outcomes pertinent to the objectives of this thesis alone. Only the final status of the model will be discussed within the context of the non-swept angle testing. It is also worth crediting the undergraduate students who contributed to this project and some of the design decisions that were employed to develop the final model and experimental setup.

5.2 Aerodynamic Profile

From the onset of this project a specific airfoil profile was set for use in the final model. The airfoil, as illustrated in Figure 27, is relatively low camber throughout its span spare the cusped region on the pressure side near the trailing edge. It was custom designed by Joby Aviation specifically to accommodate the flow characteristics of the Cal Poly LSWT. The intent was to generate natural boundary layer transition at a Reynolds Number 9.2×10^5. No other requirement for a specific coefficient of lift or such variables was necessary, as the only emphasis of the project concerned studying boundary layer transition.

This airfoil was designed primarily to generate natural boundary layer transition between the 75% chordwise station and the trailing edge. This would apply for the upper (suction) side of the airfoil, as the bottom (pressure) side of the airfoil would not be a region of interest during testing. At a zero pitch angle, a near-zero pressure gradient was expected to develop along the majority of its chord length. The delayed inflection in pressure gradient would in turn delay the onset of boundary layer transition. The specific static pressure distribution that represents that design philosophy is explored in Section 6.2.

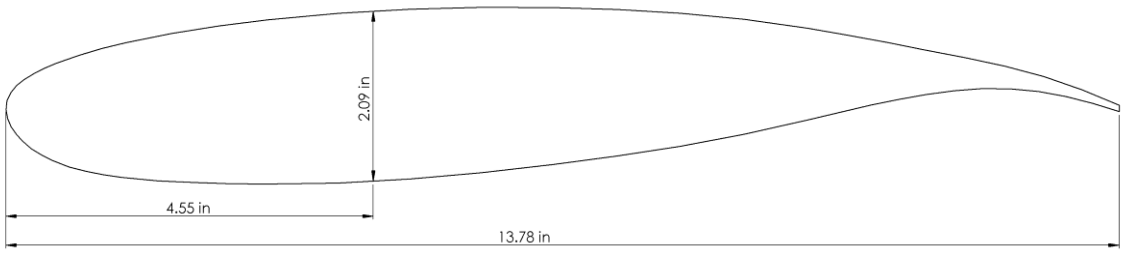

Figure 27: The Airfoil Profile Designed by Joby Aviation for Use in the Infrared Wing Model Design.

A requirement of the final model's design would be to manufacture the airfoil profile to its full chord length of 13.78 inches as it would produce the designed pressure gradient at the Reynolds Number per length matching the wind tunnel's maximum speed (40 m/s). The point of maximum thickness occurs at a chord station of 0.33 x/c where the airfoil has a thickness of 2.09 inches. The thickness of the airfoil profile was an important metric during the manufacturing process of the model, where internal space would become a difficult accommodation.

With an airfoil profile decided, an infinite wing setup was chosen, where the profile shown in Figure 27 would be extruded through the full height of the Cal Poly LSWT. This was done to match the research objective of utilizing a model with known aerodynamic performance. With no sweep angle, the onset of boundary layer transition was expected to occur at a known chordwise location which would become an important basis for reference when reviewing experimental measurements. However, the implementation of sweep would change the known qualities of the model, allowing for compliance with the other set of objectives.

5.3 Material Selection

The decision was made to use aluminum 3D printing to manufacture the wing model for this project. As discussed in Section 2.2.2.3, infrared thermography works best with materials that have a high thermal conductivity and a high capacity for thermal energy storage. Metals, specifically aluminum, are best suited for fulfilling those needs.

Use of an additive manufacturing method also provided the guarantee of a tight-tolerance, uniform wall-thickness. Infrared thermography, as stated prior in Section 2.3.1.4, finds the clearest results with high temperature differentials generated on uniformly-heated surfaces. Having a variable thickness outer wall would result in the infrared camera seeing it expressed as a non-uniform heat gradient and consequentially obscure the interpretation of the imaging results.

In the context of traditional subtractive manufacturing techniques, the process of generating an internal cavity with an emphasis on uniform wall thickness would've been an equally tedious process to undertake. Such a process was in fact exemplified by the

manufacturing of the previous Cal Poly LSWT infinite wing model [23] where only a small portion of the model span was resultantly aluminum. For the context of infrared thermography, such a compromise would not be viable. The combination of aluminum's favorable properties and the availability of an aluminum-powder selective laser melting (SLM) machine resulted in the final decision to use 3D printed aluminum as the primary structure of the wing model.

5.4 Heating Application

A series of silicon-rubber heating pads were bonded to the inside surface on the wing model and wired to a single electrical connection on the outside, where a power supply could simply be turned on or off in order to pre-heat the model. This approach was derived from the solution used by a similarly-purposed aluminum infinite wing model which found success in the method. As an added benefit, control of the power supply would be the only action required between tests with the wing model to prepare it for another run if this approach would be taken. Not only would the permanent placement of internal elements improve the uniformity of heat distributed but it would also alleviate the burdens of using a temporary wrap as was done prior.

5.5 Pressure Measurement Validation System

The other primary objective of this thesis research was to explore the use of a secondary validation system. Various options for this approach exist, whether be a quantitative sensor measurement or a qualitative flow visualization technique, as discussed in Section 2.3.3. To stay in line with the design objective of using materials and equipment readily available to future students of the Cal Poly LSWT, a pressure-based system was selected for the purpose of this research. Like any proper wind tunnel model, the wing model would be designed to incorporate a set of static pressure taps along its chordline, the placement and design of which are highlighted in Sections 7.2 and 9.4 respectively. These static taps would be designed with the intent of confirming that the model's pressure distribution qualities match airfoil's simulated expectations as well as assisting with pitch and sweep angle alignment.

The implementation of a Preston Tube would serve to fulfill the objective of including a secondary results validation system. The Preston Tube, as discussed in Section 2.3.1.4, is a total pressure probe which sits on the surface of the model—fully submerged in the boundary layer—coupled with a corresponding static pressure tap in order to approximate local skin friction coefficient. Ultimately, it was agreed upon that the infrared wing model would be designed with a Preston tube system capable of traversing the chordline in order to detect the variation in local skin friction coefficient between laminar and turbulent boundary layer flows.

Chapter 6

PRELIMINARY SIMULATIONS

Numerical simulations were performed at the onset of this project using the Siemens Star-CCM+ package. Two-dimensional (2D) steady-state RANS simulations were performed using an import of the outer aerodynamic profile to predict its performance in the Cal Poly LSWT at the designed operating conditions. The results shown in the following sections discuss the methods utilized to build the simulations as well as the impact the information had on the eventual design of the model and its instrumentation.

6.1 Simulation Build & Settings

The first simulations performed, which comprise of the majority of CFD work performed for this project, focused on a 2D analysis of the airfoil profile designed for use in the wing model (reference Section 5.2). The first simulations performed focused on getting predictive data on the pressure distribution of the airfoil for the angles of attack it would be operated at. The results from the simulations would be used as a baseline comparison for the experimental data collected by the wing model during its wind tunnel testing.

A rectangular domain was generated with a vertical constraint that matched the width of the Cal Poly LSWT test section. Sufficient forward and rearward distance was provided to allow for the dissipation of the pressure field and turbulent effects generated by the model before reaching the inlet and outlet boundary conditions. The domain extends 2L forward the leading edge of the airfoil and 3L behind, where L is equal to the 421 cm length of the Cal Poly LSWT test section (reference Figure 28).

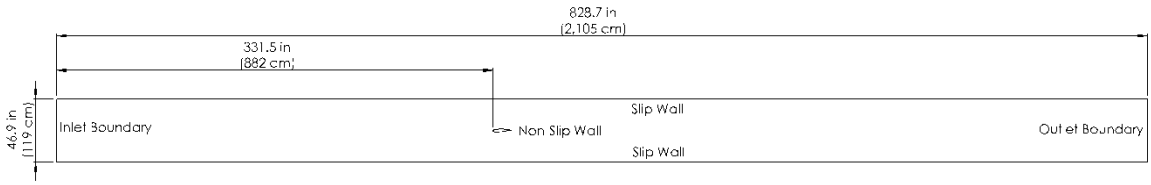

Figure 28: Domain Size and Boundary Specifications of the 2D CFD Simulations.

The mesh was generated with triangular cells and a prism layer around the airfoil body to better capture boundary layer effects. The prism layer was given additional refinement—both in spanwise distribution and in vertical resolution—to increase the quality and quantity of cells generated. Additional region refinements were added as a conical zone around and behind the airfoil part to help better resolve any wake effects it might generate. Overall, the 2D mesh was generated with a sum total 485,000 cells, allowing it to be well-structured yet easily solved on a home computing system. The specific settings used to build the mesh, illustrated locally around the airfoil in Figure 29, are outlined in Table 2. With this mesh, no location around the airfoil part's surfaces exceeded a Wall Y+ value of 2.5.

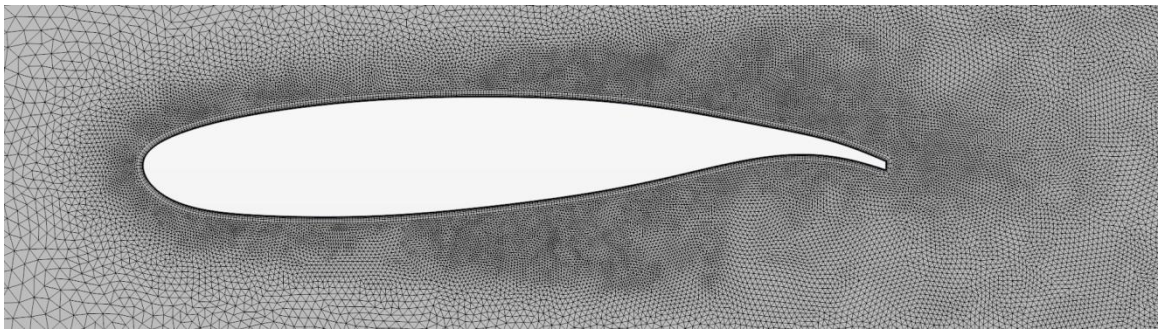

Figure 29: Local View of the Two-Dimensional Mesh Generated Around the Airfoil Part.

Table 2: List of Mesh Settings Used for the Two-Dimensional Simulations.

Base Settings			
Meshers	Triangular, Prism Layer		
Base Size	1.0 in	**Surface Growth Rate**	1.1
Target Surface Size	1.0 in	**Number of Prism Layers**	10
Minimum Surface Size	0.1 in	**Prism Layer Stretching**	1.5
Surface Curvature	36 points/circle	**Prism Layer Thickness**	0.125 in
Custom Control			
Target	Airfoil Part Body		
Target Surface Size	0.05 in	**Wake Control Spread**	0.1 radian
Minimum Surface Size	0.025 in	**Wake Absolute Size**	0.1 in
Wake Control Distance	8 ft	**Wake Growth Rate**	1.2

The airfoil was simulated with all-turbulent conditions to gather the static pressure coefficient distribution results. The k-ε turbulence model was implemented under the assumptions of a constant-density flow regime while using a steady, coupled solver. A 2% free-stream turbulent intensity was applied to represent the best known characterization of the Cal Poly LSWT's flow quality. The solvers selected, as well as the specific settings provided to each, are listed below in Table 3. The inlet boundary was given a flow specification of 40 m/s velocity magnitude and a turbulence intensity of 0.02.

Table 3: List of Solvers and Settings Used for the Two-Dimensional Simulations.

Solvers Selected			
Space	Two-Dimensional		
Time	Steady	**Equation of State**	Constant Density
Material	Gas	**Viscous Regime**	Turbulent
Flow	Coupled	**Turbulence Equations**	k-ε Turbulence
Coupled Implicit Settings			
Courant Number	5.0		
k-ε Turbulence Settings			
Under-Relaxation Factor	0.8		

6.2 2-D Static Pressure Coefficient Distribution

Using the mesh and solver settings listed in Section 6.1, the airfoil was simulated at angles of attack of 0^o, 2^o & 4^o. A short run time of only 500 iterations was required for each of the simulations to achieve convergence. The static pressure coefficient values extracted along the upper surface of the airfoil are shown below in Figure 30. These values were non-dimensionalised using the input velocity of 40 m/s and an air density of 1.19 kg/m^3, the typical ambient readout at the Cal Poly LSWT.

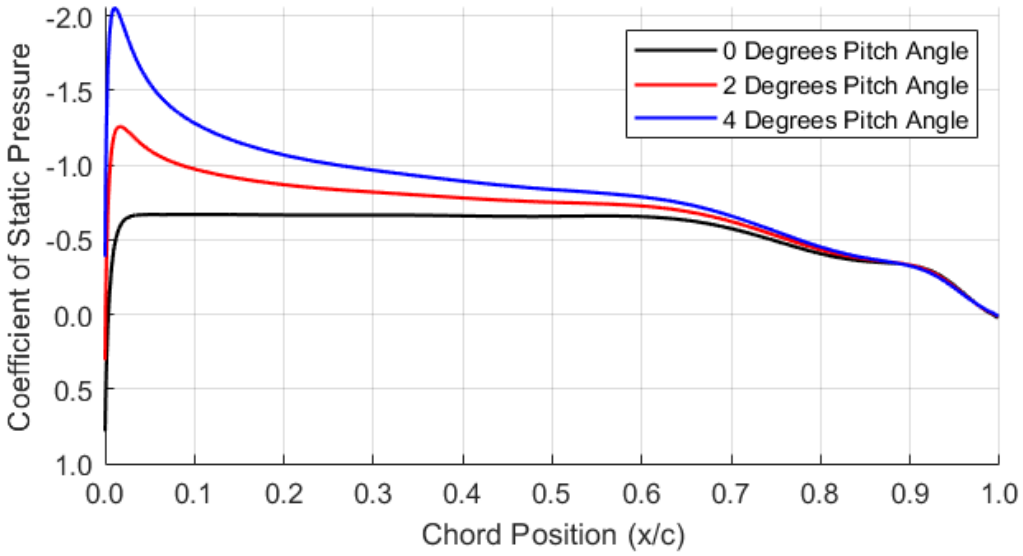

Figure 30: The Static Pressure Coefficient Distribution Along the Suction Side of the Airfoil for 0^o, 2^o & 4^o Angles of Attack.

As anticipated, the airfoil profile produces a near-zero pressure gradient at its zero-angle condition between the chord locations of 0.05 x/c and 0.60 x/c. This couples with the criteria and expectations that fed into the design of the airfoil profile originally. As such, visualizing this effect in the simulation results confirms that it is accurately capturing the aerodynamic details that the airfoil is designed to exhibit.

6.3 2-D Skin Friction Coefficient Distribution

Using the simulations described and configured in Section 6.1, the distribution of local skin friction coefficient was collected alongside the static pressure coefficient distribution. These values will be vital in the analysis performed in Section 12.3, where the data from the Preston Tube setup is used to validate the results assumed by the infrared camera's images. Similar to the information presented prior in Figure 30, the following figure compares the distribution of local skin friction coefficient alongside the upper surface of the airfoil for the conditions of 0^o and 2^o angles of attack. The 4^o condition is not shown here for the reasons explained in Section 12.3. The following plot, Figure 31, displays the data collected for both an all-turbulent and an all-laminar simulation condition.

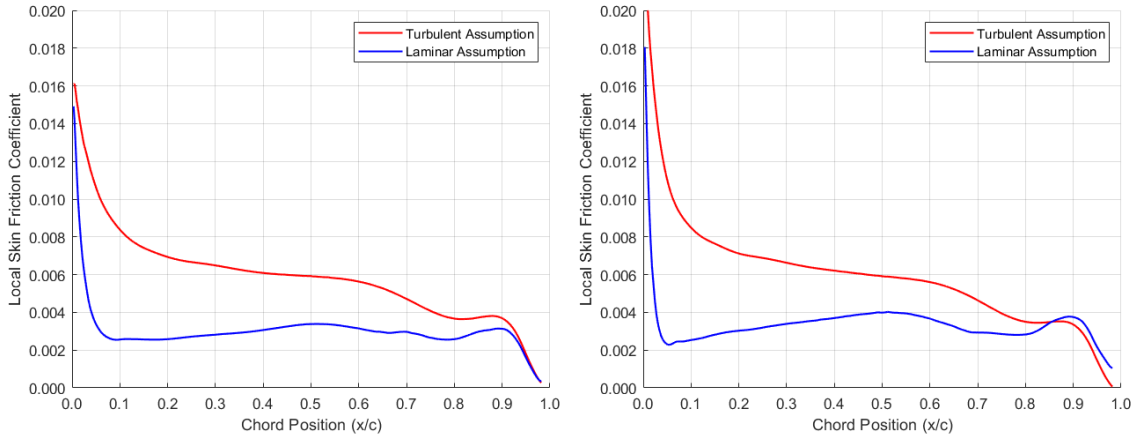

Figure 31: The Local Skin Friction Coefficient Distribution Along the Suction Side of the Airfoil for 0^o (Left) & 2^o (Right) Angles of Attack.

In order to obtain data from simulations with an all-laminar flow field, some of the solver settings previously listed in Table 3 had to be modified. As one could anticipate, the viscous regime was set to 'Laminar' and no subsequent turbulence model equation set was selected. However, the prior settings used for the Coupled Implicit solver were giving was to an unstable solution which would only diverge in error. To help stabilize the solution, the Courant Number was bumped up to a value of 10.0. In addition, the Star-CCM+ specific features 'Expert Initialization' and 'Solution Driver' were enabled to further restrict the deviance of the solved solutions.

The implementation of these features was expected to heavily dampen the output of the solution, likely producing a converged result that is not too closely representative of real life conditions, but was necessary in order to obtain a stable solution within the short working time frame available at the time. Since the focus of this research was never concerned with generating high-fidelity CFD predictions, this outcome was deemed sufficient enough to satisfy the experimental outcomes. The use of a program such as XFOIL, which is much more robust and validated in producing pressure coefficient and skin friction coefficient data, would have been better suited for the nature of this project. Future research learning from these experiences should follow such a route to save on time spent and benefit from higher quality data up front.

Chapter 7

MODEL DESIGN

7.1 Mechanical Design Goals

Configurability was the driving goal for the mechanical design of this wing model and its accessories. This originates due to the fact that the model had to be designed for two different testing campaigns in mind. As such, the needs of each set of objectives would simultaneously influence the individual design qualities of the model. Configurability would be the means of ensuring the same model could be used to satisfy all of its necessities through rapid and simple mechanical adjustments.

Since the span of the model would have to change with each sweep angle tested, a requirement was set that the metallic center section of the model would need to be re-usable with every configuration. Therefore if the mechanism is designed properly, the bulk of the model—the most tedious and difficult to manufacture assembly—would be re-used for each geometric configuration and instrumentation scheme possible.

Following the testing objectives outlined in Chapter 3, a derived requirement was set such that the model must be able to configure for pitch angles ranging from 5^{o} to -5^{o} as well as sweep angles from 0^{o} to upwards of 55^{o} maximum. Another critical feature of the design process would be the necessity for all heating devices to be pre-installed in the model and not require additional configuration once the wing is installed to the wind tunnel. This stems from the shortcomings endured during prior infrared thermographic testing (reference Section 4.3). The time invested into designing a model which could be plugged in and ready to use would make a substantial difference in the time required to test the model during the experimental phase.

As for instrumentation, the pressure taps integrated to this model would need to be functional for both the research objectives of both testing campaigns. The process to balance the impact of that both sets of testing goals weighed in on the model will be evident in the design steps outlined in the following sections.

7.2 Printed Profile

Given the aerodynamic profile provided in Section 5.2, it had to be converted into a cross-sectional profile compatible with the 3D printing process planned for use (reference Section 5.3). Keeping the parts hollow was a necessity due to provisions such as the heating pads and static pressure taps.

The design tradeoff with the aluminum printed parts was to pick a wall thickness that maximizes thermal capacity but minimizes the cost of manufacturing—an aspect which was already at a high starting point for the chosen process. A thicker wall retains more heat and allows the model to hold its temperature gradient for longer time durations while testing but would consume more of powder during printing. In addition, a wall that is too thin would risk the inability to generate a stable temperature gradient before all its heat is convected away by the free stream flow. In the end, a wall thickness of 0.125 inches (3mm) was selected. That value was determined through the use of rudimentary thermal simulations which continually reduced the wall thickness implemented by the Ducted Nacelle Model until the thermal capacity would be superseded by the convection rate of the free stream flow.

After selecting a wall thickness, the internal cavity of the profile was created to free up as much internal space as possible. There was a point at the trailing edge which the airfoil profile height became thinner than the 6mm combined wall thickness and had to be kept solid. This occurred around a chordwise position of 0.84 x/c. The last feature added to the print cross-section was two protrusions with 0.3125” through holes in the center. These are where the structural support rods (as described in Section 7.7) would be accommodated. The diameter and location of the rods was determined by Finite Element Analysis (FEA) predictions which indicated the system would suffice for the aerodynamic loads anticipated by CFD simulations. These protrusions were placed on the interior of the bottom surface of the airfoil, to ensure that the interior upper surface would have as much undisrupted space possible to accommodate whatever size heating elements were to be selected.

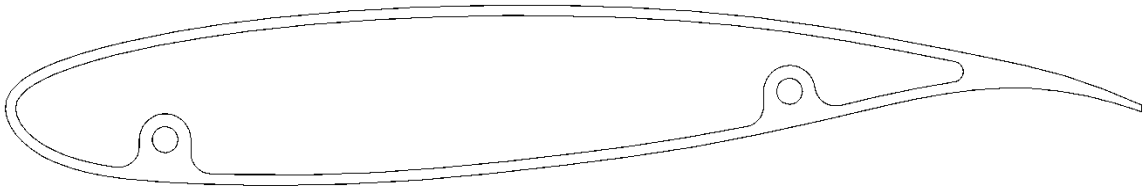

Figure 32: The Cross-Sectional Profile of the Wing Model.

7.3 Static Pressure Tap Distribution

The location of the static taps on the wing model was distributed based on CFD predictions to best capture the areas where the highest pressure gradients would occur. This was done in planning for the Preston Tube setup such that its placement would find more resolution at the chord stations where boundary layer transition would naturally occur. The spanwise distribution of the pressure rows was bound by two factors: the maximum port capacity of the Cal Poly LSWT's digital pressure transducer and the division of parts based on manufacturing limitations (reference Section 7.4.1).

7.3.1 Chordwise Distribution

The chordwise distribution of static pressure taps on the model was determined based on the predicted static pressure data reviewed in Section 6.2. The original estimate for the model was that four rows of static taps would be implemented with each row containing 16 taps overall. All together, this would fill up the 64 available spaces on the Scanivalve ZOC33 digital transducer used by the Cal Poly LSWT. Those 16 taps were spaced with concentration towards the leading and trailing edge of the model, since that's where the CFD predicted the static pressure gradient would be at its highest, as illustrated previously in Figure 30.

Five taps were placed at the leading edge within the first 7% of the chord line, with one of those five placed at the zero-angle stagnation point and another below. Seven of the sixteen taps were concentrated at the trailing edge, equally spaced within the last 16% of the chord line. The benefit of using an additive manufacturing process was that tap routing could be designed into the solid wall thickness of the trailing edge, allowing for more resolution at the rear than otherwise possible. The last remaining four were placed along the center-chord of the airfoil where the zero-

angle pressure gradient was expected to be near-zero. For that reason, tap resolution was the least important, hence why each individual one of those four taps functionally covers nearly 19% of the chord line.

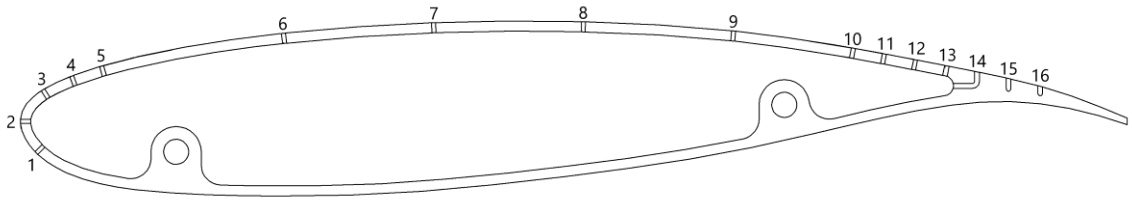

Figure 33: The Chordwise Distribution of Static Pressure Taps and their Respective Numbering.

Table 4: The Chord Station Positions of Each Static Pressure Tap Location.

Port 1	**Port 2**	**Port 3**	**Port 4**	**Port 5**	**Port 6**	**Port 7**	**Port 8**
0.014 x/c	0.000 x/c	0.020 x/c	0.046 x/c	0.073 x/c	0.232 x/c	0.363 x/c	0.493 x/c
Port 9	**Port 10**	**Port 11**	**Port 12**	**Port 13**	**Port 14**	**Port 15**	**Port 16**
0.624 x/c	0.753 x/c	0.782 x/c	0.809 x/c	0.837 x/c	0.864 x/c	0.893 x/c	0.922 x/c

The locations of the chosen static pressure taps were mixed with the CFD prediction data shown in Figure 30 to see how the distribution would appear if it were measured only at the discrete locations of the taps. The resultant agreement was strong and reassured that the selected tap locations should be able to distinguish between angles of attack within 1^{o} of variation, as visualized in Figure 34 below.

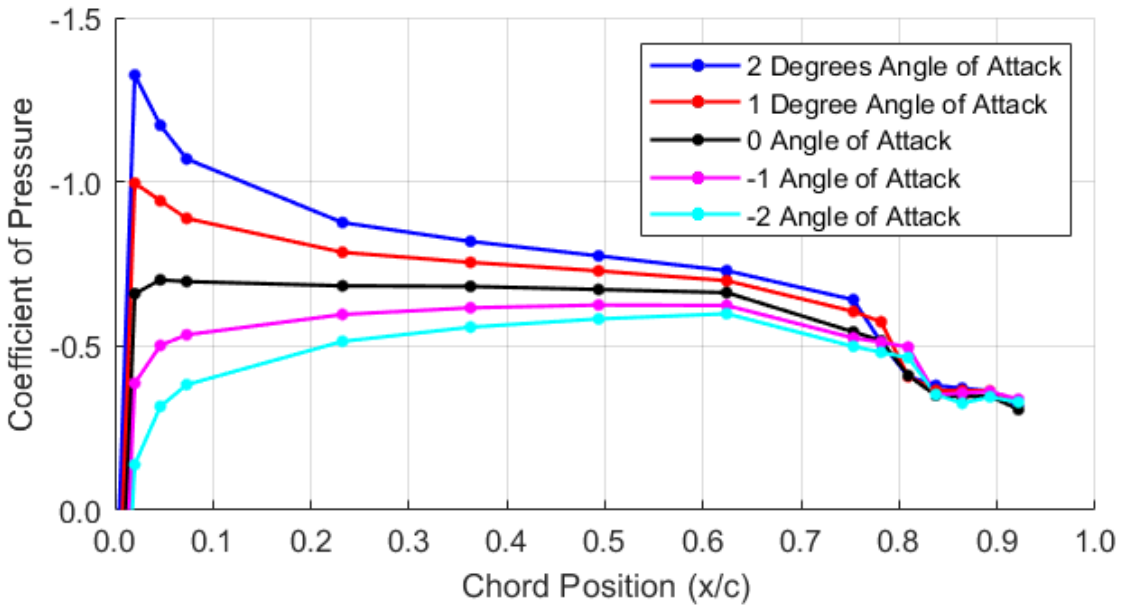

Figure 34: Prediction of Static Pressure Tap Measured Coefficient of Pressure Distribution Based on Interpolating CFD Data at the Sixteen Known Static Tap Locations.

7.3.2 Spanwise Distribution

The static pressure tap rows illustrated in Section 7.2.1 were incorporated into the model at four different spanwise locations. That was selected in part for two reasons. The first driving factor was that the volume limitation of aluminum powder printing beds necessitated that the model be divided into smaller sub-sections, as described in further detail Section 7.4.1. The second factor was, although not necessary for the testing required by this thesis, the model had a requirement to measure pressure distribution under positive sweep to allow for correlation with CFD predictions. Implementing multiple rows of taps would add better insight into the flow quality along the entire model span, rather than at just one discrete station.

Another design trade-off occurred from this process where the decision to concentrate more pressure taps in each row—better for chordwise resolution—was weighed against the increased spanwise distribution of taps which would favor swept-angle CFD correlations. The ultimate resolution to strike a balance between those two aspects was to implement four rows of static taps with 16 taps each, resulting in the chordwise and spanwise distributions shown in Figure 33 and 35 respectively.

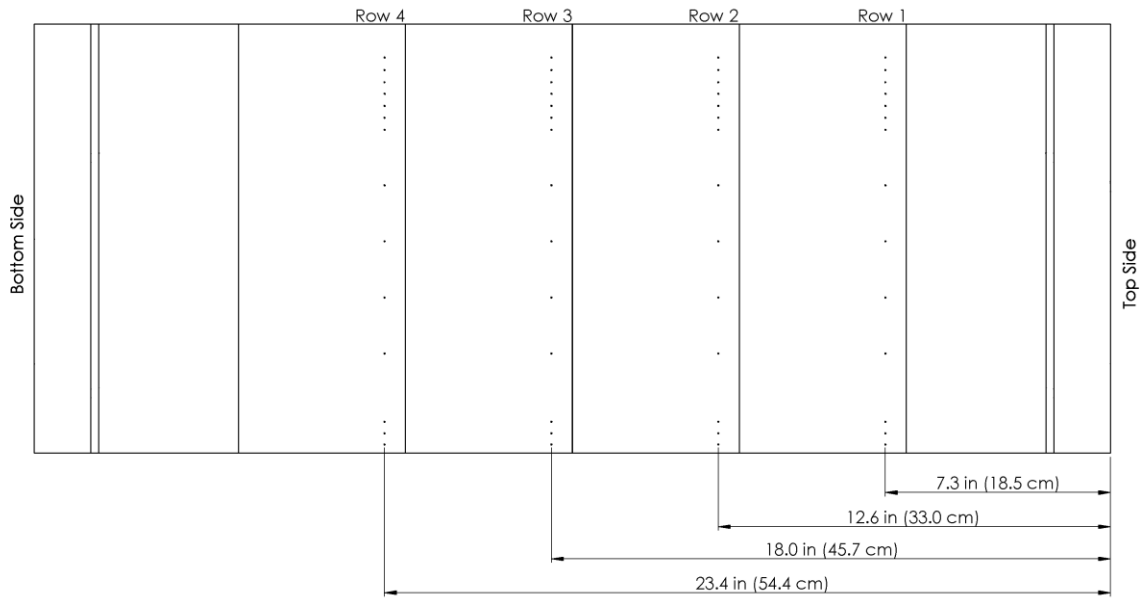

Figure 35: The Spanwise Distribution of Static Pressure Taps and their Span Station Positions.

7.4 Assembly Division

Due to the limitations that were present in manufacturing budget and timeline, printing the aluminum center section as a single piece was not feasible. In addition, further complications would be introduced regarding the necessity for interior access in the model, as required by the accessories and instrumentation planned to be rigged within the hollow cavity. As such, the 36.7 inch (88 cm) span of the model was divided into multiple sub-sections of different material type and function. Overall, the final model assembly would consist of a large aluminum center section, plastic end pieces and cork insulators separating the other two. The design and details of those respective sub-sections are described in the following text.

7.4.1 Printed Aluminum Sections

As discussed in Section 7.1, a driving aspect of the design of the model was the necessity for it to be modifiable to allow for a positive sweep angle upwards of 55^{o}. That became the bounding factor which sized the span of the aluminum center section. To clarify, the center section would have to be small enough to fit within the vertical constraints of the Cal Poly LSWT height of 34.7 inches (88 cm) when rotated to engage a positive sweep angle. Figure 36

illustrates the trigonometry which determined the span limitation of the center section, where the height of the test section was set with the model opposed at a 45^{o} relative angle. The perpendicular distance between the diagonal corners of the model, with space accommodated for two 0.25 inch thick cork insulators, would equal the maximum allowable span.

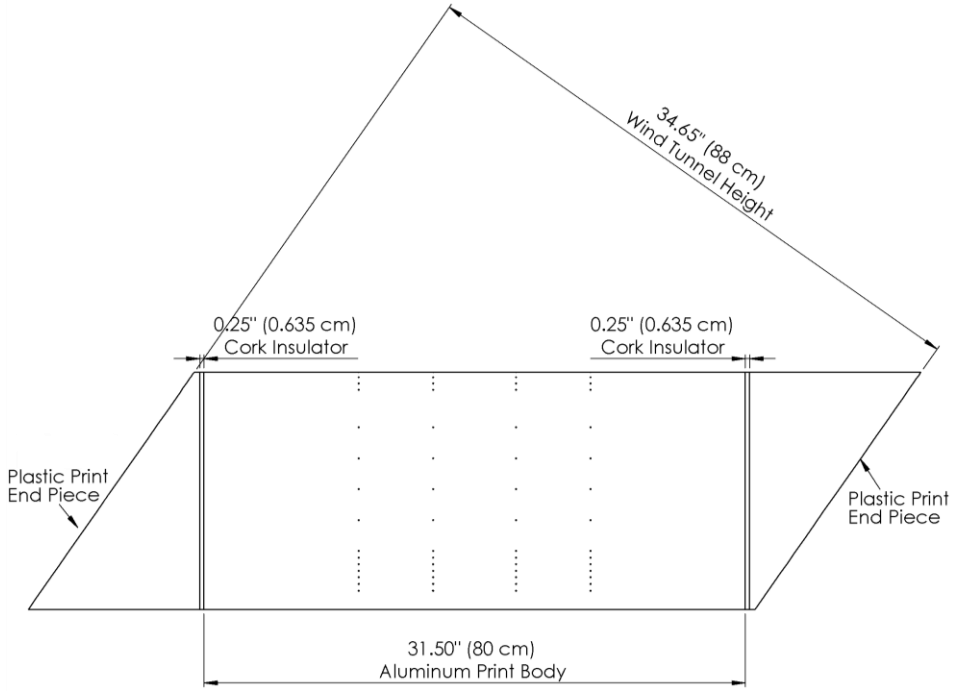

Figure 36: Trigonometric Measurement of the Wing Model When Swept at a 45^{o} Angle Used to Determine Maximum Allowable Span of the Aluminum Center Section.

Based on the measurements illustrated in Figure 36, a maximum allowable span of 31.5 inches (80 cm) was deduced for the aluminum center section. That span was divided into six sections with overall parts of two different types: sections with static pressure taps and sections without. Each static pressure tap row would be allocated its own equally-wide section of the overall span. Two other aluminum parts would be printed with a bare exterior for the function of filling in the remaining space at either end of the span. Figure 37 below illustrates the final division into the six aforementioned parts.

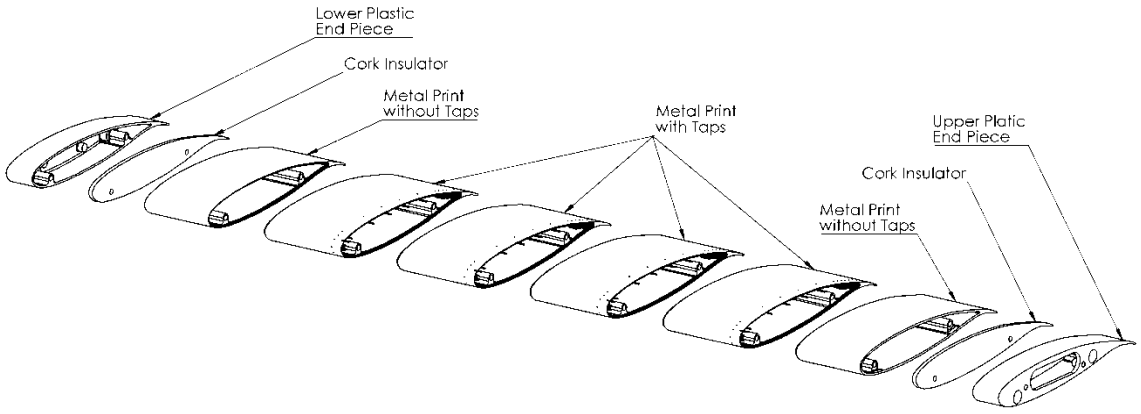

Figure 37: Division of the Wing Model Showing the Six Aluminum Center Pieces, the Two Thin Cork Insulators and the Two Plastic End Wedges Used for the 0^{o} Sweep Configuration.

The four parts that would incorporate the static tap rows would be printed with an individual span of 5.4 inches (13.7 cm) while the outer two parts would have an individual span of 4.95 inches (12.6 cm). The partitioning of the aluminum center section would ultimately drive the sizing and placement of the internal heating elements, as reviewed in Section 7.5. Eventually, the six printed aluminum parts would be fixed together and permanently bonded to create a single entity through the future.

7.4.2 Cork Thermal Insulators

Aluminum was selected as the primary structural material of the wing model due to its favorable thermal capacity and conductivity characteristics. In order to perform an infrared thermographic test, the model has to be set to a temperature beyond ambient conditions to allow for the boundary layer flow to differentially cool the model. For this model specifically, a heating method with a design temperature upwards of 180^{o}F was selected based on the power output of the silicon-rubber heating elements planned for use. This created a design dilemma where the potential for the heated aluminum to deform the plastic end pieces could potentially happen. For reference, the plastic end pieces are the interchangeable part of the model which will provide the ability for sweep angle to be introduced. More details about their function and design are described in Section 7.3.4 below.

Since the glass transition temperature of the plastic being used for the end pieces was researched to be below the 180^{o}F design target, an intermediate insulator was required to prevent the plastic from being damaged or deformed by the pre-heating process. Cork was eventually settled on due to its affordability and low coefficient of thermal conductivity. Simple thermal simulations performed by the original undergraduate design team suggested a thickness of 0.125 inches (0.32 cm) was sufficient to protect the plastic parts. However, for practicality sake, the cork insulators were bumped up to a final design specification of 0.25 inches (0.64 cm) in thickness to further reduce the risk of damage to any parts used within this project.

7.4.3 Plastic End Pieces

Since the wing model had to be designed with an accommodation for introducing sweep angle, the aluminum center section was bound to a maximum span to ensure it would always fit within the geometric bounds of the Cal Poly LSWT. The maximum span, as discussed prior in Section 7.4.1, was determined to be 31.5 inches (80cm). To fill in the extra span necessary to continue the airfoil profile from wall to wall, plastic end pieces were incorporated into the design. In addition to filling in the aerodynamic profile of the model, these pieces were designed to be interchangeable to allow the model to be oriented with a positive sweep angle. This mechanical approach to adjusting sweep was deemed to be the simplest and most cost-effective approach available. Figure 38 exemplifies how swapping one set of the plastic end pieces allows for the effective sweep of the model to be varied.

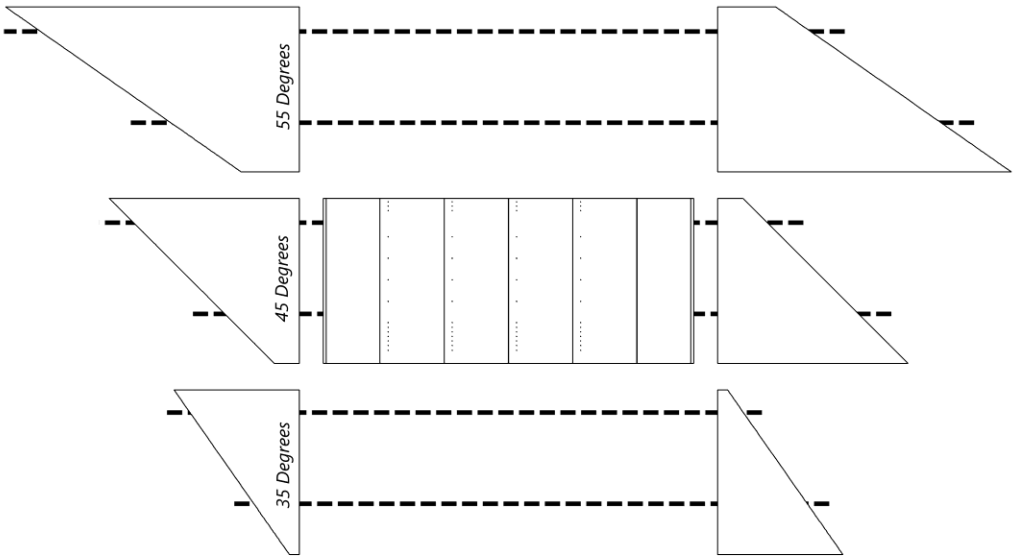

Figure 38: Conceptual Illustration of the Replacement of Plastic End Pieces to Adjust Sweep Angle.

3D printed plastic was selected as the manufacturing process for these parts, in part due to the current reliability of the technique for producing complex geometries but also due to the associated cost rationality. Overall, with this thesis research included, this model is anticipated to be tested with four different sweep angle configurations. That calls for four sets of plastic parts to be produced—eight parts overall with some as large as two feet in span. To continue making those eight parts out of the 3D printed aluminum would make for an unreasonable financial commitment. Since the parts would already be out of the infrared camera's region of interest due to the impingement of wall effects, plastic was able to serve as a suitable selection. This allows the plastic end pieces to maintain the three-dimensional aerodynamic profile of the model from wall-to-wall without being concerned with the thermodynamic burden of being used for infrared thermographic study.

7.5 Test Section Layout

The wing model developed for this research was designed to share test section placement with the previous infinite wing model used by the Cal Poly LSWT [23] in order to reuse the fixtures already integrated at that location. The leading edge would be positioned around 36% down the length of the test section (see Figure 39), marked by where the cross-section of the

wind tunnel remains constant. This location was where the only wooden ceiling panel exists within the Cal Poly LSWT, making it an idea mounting location for a model of this geometry. The electrical wiring and pressure tubing was designed to route through the model and out an opening through the wooden ceiling panel, as described in Section 7.8.

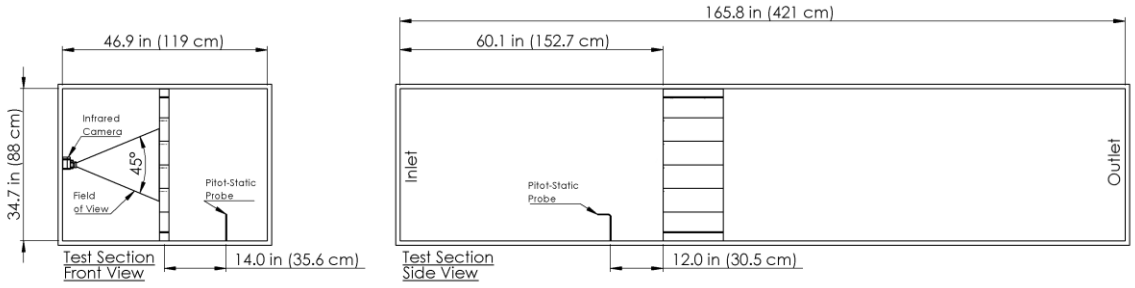

Figure 39: Schematic of the Wing Model, Infrared Camera and Pitot-Static Probe within the Cal Poly LSWT.

The infrared camera used for this research was to be mounted on the inside of the test section, height-centered on the wall closest to the control room. The camera's 45^{o} field of view allowed it to see most but not all of the wing model's aluminum center section at any given moment. An external pitot-static probe was eventually mounted through the test section floor during the pressure measurement process. Its positioning was set close to the wing model without seeing noticeable influence from the generated pressure field. The specific function regarding the use of that probe is further explored in Section 12.2.1.

7.6 Heating Element Placement

As originally discussed in Section 5.4, this model was set to utilize internal silicon-rubber heating pads as its primary means of pre-heating before use in infrared thermographic testing. This approach has been utilized by similar aluminum wing models utilized for infrared thermographic testing in the past [9] and thus was considered a strong option for the design of this model. The manner by which the aluminum center section was partitioned into multiple sections set the precedent for how these internal heating elements would be sized and positioned. To start, the aluminum center section was split into a sum total of six individual parts, where the space require to install the four static pressure rows would act as physical barriers divvying up the

internal surface area of the model. This meant that six separate heating pads could have been integrated into the design in order to maximize the amount of surface area pre-heated for testing. In the end, only the central four locations were utilized (reference Figure 40).

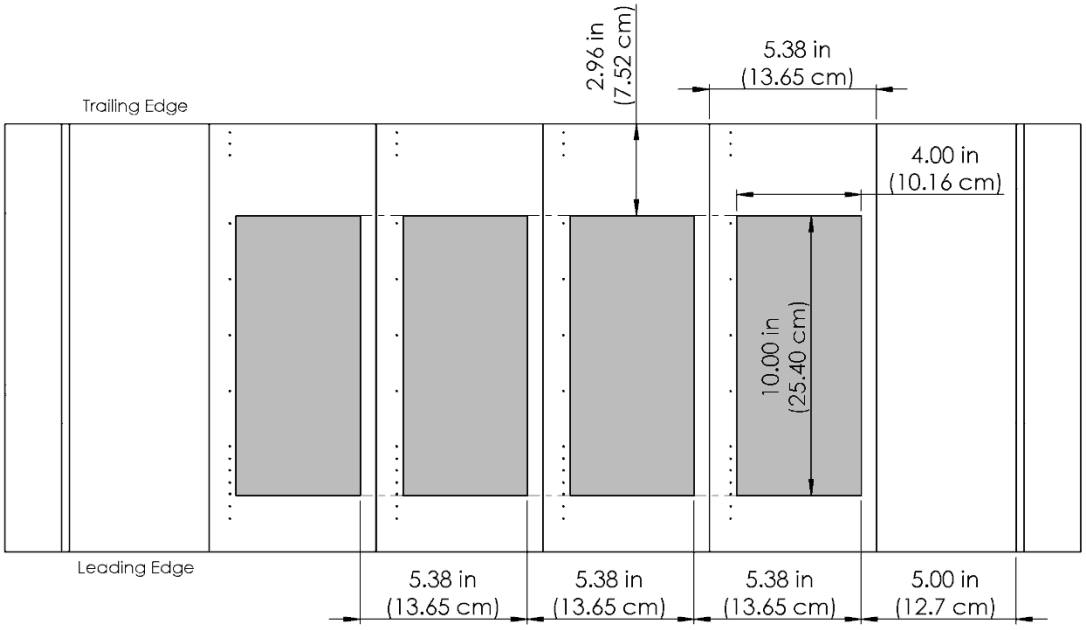

Figure 40: Position and Sizing of Internal Heating Elements within the Aluminum Center Section.

The heating pads selected were BriskHeat SRW Series products, since they were the only product series which could readily produce the designed dimensions necessary to cheaply accommodate this model. Based on an interior arch length of 13 inches between the leading edge and the filled section of the trailing edge, the closest available length for purchase at the time was 10 inches. This paired with a 4 inch width, resulting in a heating pad which was able to cover the majority of the upper interior surface area of each aluminum print section. The pads would be ordered with a pressure-based surface adhesive to allow them to be permanently bonded to the aluminum for all future testing. That feature in itself overcomes one of the main shortcomings experienced during the testing of the Validation Model and the Ducted Nacelle Model, as discussed in Sections 4.1 and 4.2.

The pads are rated for a maximum input voltage of 120V and a power density of 5 W/in^2. The rated operating temperatures exceed double the design goal of 180^{o}F, so their power density was not a driving detail since they would be operated far below maximum capacity. The rationale was that a slower, more-uniform heat application would be preferable for infrared thermography than a higher-power approach which might not be able to distribute heat as evenly to the leading and trailing edges beyond the heating pads contact.

7.7 Insulative Coating

A thermally insulating outer layer is critical to the successful execution of an infrared thermographic test. Such a conclusion was based on the results discussed in Section 4.3.1 as well as the approach taken by another aluminum infinite wing model designed for infrared thermography testing [9]. Prior testing with the models discussed in Sections 4.1 & 4.2 demonstrated the impact of adding exterior vinyl wrap to aid in the thermodynamic and emissive properties of the model. Since this model was already being designed with a lot of new and unproven functionalities, the decision was made to keep this aspect consistent with the already-proven approach. Two layers of 3M 2080 Series matte black automotive vinyl wrap was used to coat the exterior of the model once manufactured. With the vinyl implemented as a thermal insulator, only the aluminum center section was wrapped as it was the only region of the model capable of pre-heating and being used for the planned infrared thermographic studies. The final material stack-up of the model with all elements included is illustrated in Figure 41.

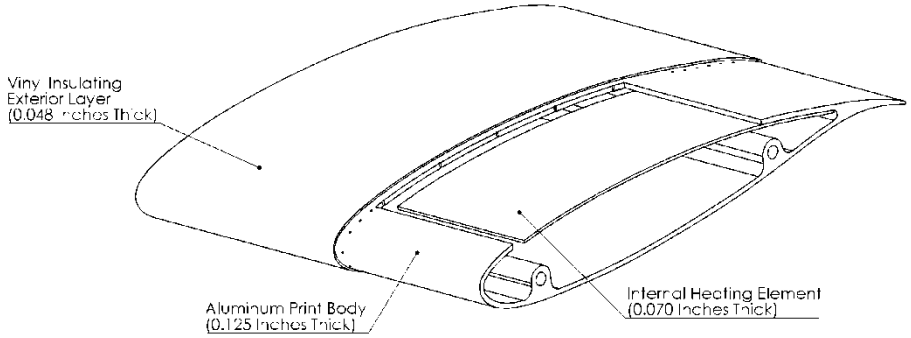

Figure 41: Three-Dimensional Representation of the Model Material Stack-Up Representing the Aluminum Wall, the Internal Heating Elements and the External Vinyl Wrap.

7.8 Support and Structure

Part of the design and analysis efforts for the structural support of this model is attributable to the undergraduate student team who initially kicked off this project. The solution presented for the wing model was a set of two steel rods which would run the entire span of the model and compress all of the aluminum, cork and plastic sections together. The protrusions discussed in Section 7.1 were integrated to accommodate these two structural rods. The intent of these parts would be to support the model's rigidity under the stress of the aerodynamic loads experienced during wind tunnel testing.

Due to the necessity of the wing model to be re-configurable for swept angle testing, the support rods were originally designed to be contained fully within the span of the plastic end pieces. Straight counter bore recessions were designed into the plastic parts to allow a standard-size hex nut to thread onto the end of the support rods. However, for this thesis research where the model would only be tested with no sweep angle, the support rods were modified for additional functionality.

The final solution for the structural support rods was a concentrically-threaded approach. The end of each steel rod featured external 5/16-18 UNC threads which allowed hex nuts to compress the elements of the wing model together into a unified assembly. The location of those hex nuts was instead moved away from the plastic end pieces and inwards to just the aluminum center section. That resulted in the two support rods becoming permanent fixtures of the center section once the aluminum print parts were aligned and bonded together. Recessions were made on the outer two aluminum sections to accommodate the thickness of the hex nut without it protruding into the plane of the cork insulators. The added functionality came in the form of an interior thread tapped into the end of those rods concentric with the external threading. This was used to allow sets of smaller threaded rods to screw into the main two and secure the plastic end pieces in place.

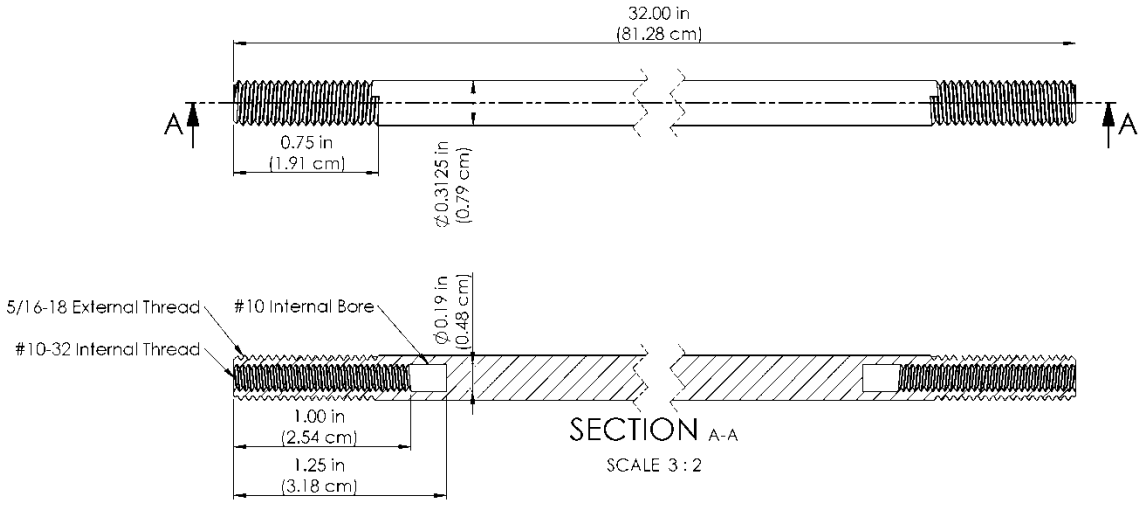

Figure 42: Representative Drawing of the Primary Support Rods.

The interior thread was sized to a #10-32, keeping the major diameter as large as possible while keeping the wall thickness to the 5/16-18 threads at a reasonable tolerance. In the end, the two primary support rods—the ones designed to be permanently integrated into the aluminum center section—were cut with both a 5/16-18 external and a #10-32 internal thread at both ends. The secondary rod extensions, as shown in Figure 43, were designed to be turned to a reduced diameter and tapped with a #10-32 external thread on one side and a 5/16-18 external thread on the other. The 5/16-18 threads still allowed for hex nuts to secure the plastic end pieces into place while the #10-32 threads allowed the secondary rod extensions to be interchangeable, swapping for different lengths which match the length of the plastic end pieces being installed.

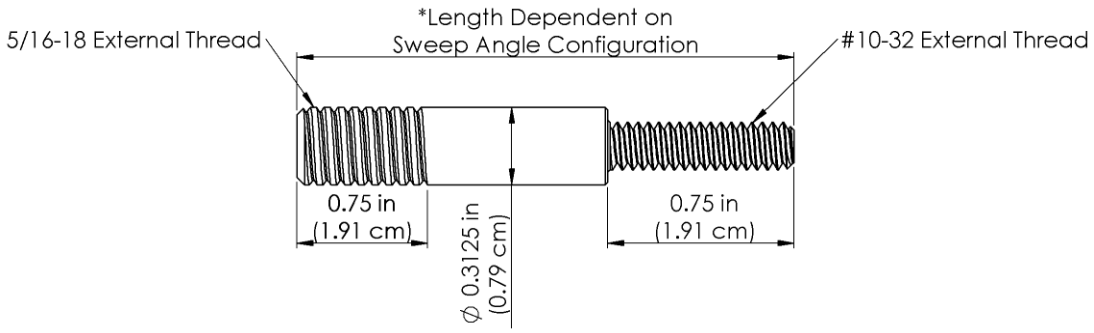

Figure 43: Representative Drawing of the Secondary Support Rod Extensions.

The estimated lengths of all four sets of extensions are illustrated in Figure 44. A complication with the selected design resulted in the requirement for two different length extensions per sweep angle configuration, since the triangular shape of the part adjusted the relative length of the support rod at each chordwise location.

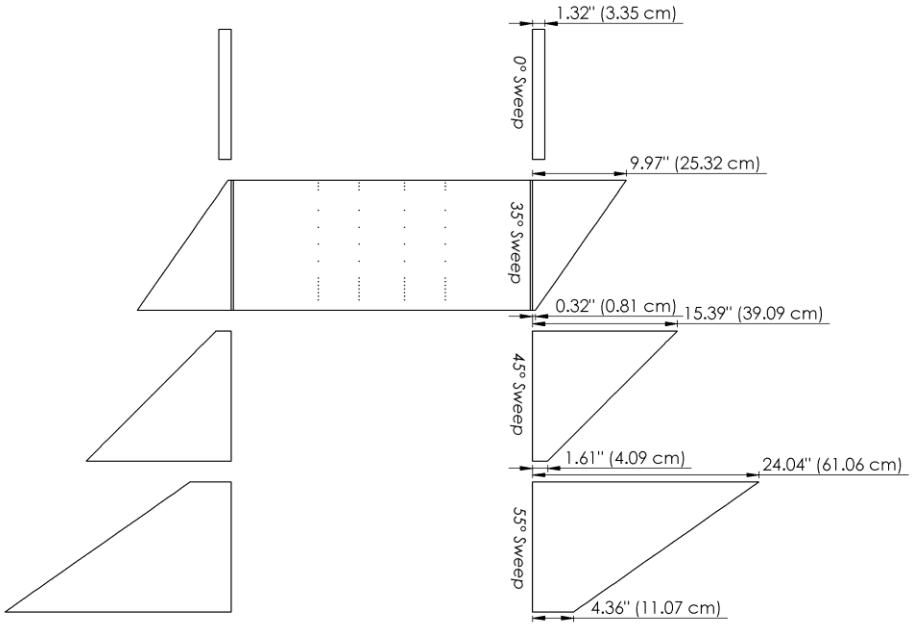

Figure 44: Comparison of Secondary Rod Lengths Based on the Plastic End Pieces Being Used.

For the 0^o sweep configuration, the secondary rod extensions were over-sized in length to exceed the span of the plastic end pieces. With the supports oriented perpendicular to the test section walls, they could simply be extended in length to pass through the walls and secure from outside the test section instead. This approach the model was, at the time of this writing, intended specifically and solely for the 0^o sweep configuration. The positive sweep configurations were still designed to run supports only up to the plastic end pieces and not through the test section walls. The revised approach made the mounting and pitch-adjustability of the model significantly simpler rather than routing through the inserts described in Section 7.8.

7.9 Model Mounting & Pitch Adjustment

The plastic end pieces described in Section 7.3.3 were designed to be manufactured with a set of two blind recessions sized to accommodate brass heat-set inserts. Those inserts were intended accommodate a pair of bolts which would secure both the top and bottom sides of the wing model to the test section. An exception was included for the 0^o sweep configuration, where the steel support rods carried through the test section walls and fix directly to the wooden panels without the use of the heat-set inserts. For reference, the vertical mounting scheme of the wing model was selected solely due to mounting concerns, where a horizontal alignment would have required tapping into the acrylic window panels—an action which was a necessity to avoid. Instead the floor and ceiling panels, both made of wood, were selected as the fixture points for the wing model. The chosen location of the wing's mounting also overlaps with the mounting location for the other infinite wing model utilized by the Cal Poly LSWT [23] since part of the infrastructure developed for that project could be repurposed for this one.

A rotating wooden plug was designed as the upper mounting point for the wing model. That would be the means by which pitch angle would be adjusted since a discrete rotation of the wooden plug would rotate the wing model the same amount. In order for it to have worked properly, the central point of rotation for the wooden part had to be aligned with the mid-point between the wing model's two steel support rods. The bottom support extensions ran through the wooden floor of the test section while the upper extensions ran through the wooden plug and bolt through directly. The design also called for a central pocket—matching the size and shape given to the upper plastic end pieces—to be cut into the wooden plug to allow the electrical connections and pressure tubing within the model to route outside the test section without exposure to the free stream flow.

In order to change the model's angle of attack (pitch angle), the wooden plug was un-bolted from the test section ceiling panel, turned by the corresponding angle delta, and then re-attached the same as before. While this operation was performed, the bottom support extensions of the model only had to be loosened to allow them to slide freely within the pre-cut grooves; re-tightening once the model was set into place.

7.10 Preston Tube for Skin Friction Measurement

The successful integration of a Preston Tube requires the presence of both static pressure taps and a total pressure probe. A probe was designed from scratch to specifically accommodate the infrared wing model. Using the assumption criteria listed in Poll [16] and Patel [15] for laminar and turbulent boundary layer flows respectively, a probe was sized to be designed with an outer diameter between 0.024 inches maximum and 0.0043 inches minimum. The process used to determine those values stemmed from the conditional requirements for the values of x* and y* as discerned in the works of Poll [16] and Patel [15]. The upper and lower limits for the all laminar and all turbulent assumptions were back-solved to find a value for inner diameter, using an approximate value of local wall shear stress (τ_w) based on the Blasius flat plate assumptions.

The requirements outlined in the two papers state that the size of the Preston tube only needed to fall within the bounds of the minimum/maximum criteria, rather than sit explicitly at either edge. Stainless steel tube stock of 0.012 inch outer diameter with a 0.006 inch inner diameter was selected for use in this project. The fragility of a part so small required a special mount to keep it fixed to the wing model such that it could be kept properly aligned with the flow, fully pressed against the surface of the model and easily adjustable to shift location. A custom 3D printed plastic mount was designed to act as the body of the probe used in the Preston Tube setup, as illustrated in Figure 45 below.

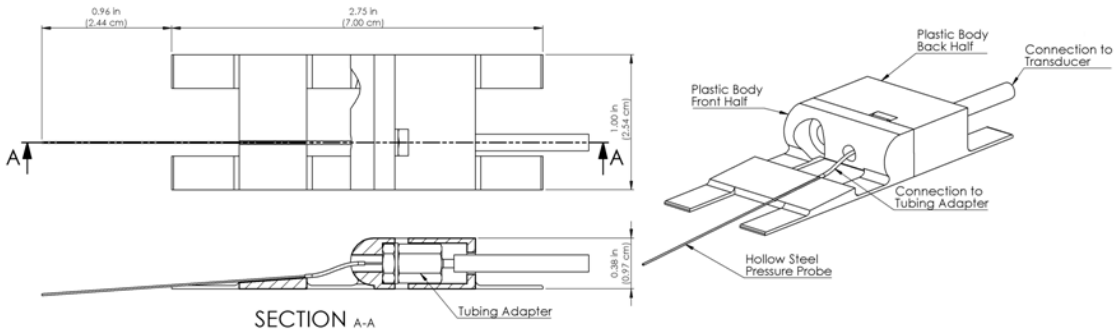

Figure 45: Multi-View Representation of the Preston Tube Mount and Assembly Design.

The probe mount body was designed with two primary sections. The first was the rearwards block which would house the tubing adapter which converted the inner diameter of the flow tubing from the probe's 0.012 inch outer diameter to the 0.0625 inch inner diameter compatible with the lab's digital pressure transducer. The probe mount body was split into two sections at that spot, where the two halves were joined together with a single button head bolt to sandwich the steel adapter into place. Spatial accommodations were added into the plastic body to account for the rubber gasket ring in the adapter as well as openings to externally route tubing to and from. The rearward block section was sized as small as possible to minimize its aerodynamic influence on upstream boundary layer flow.

The second half of the probe body was the sloped frontal plate where the stainless steel tube attached to gather measurements from the upstream boundary layer flow. The probe body was designed with a small groove in line with the adapter for the steel tube to nest into place. In addition, the plastic at that area was sloped downwards by 4^{o} to allow the probe to push against the surface of the model and ensure it was kept at the bottom-most region of the boundary layer possible. The extremely small size of the hollow steel tube required that was simply taped into place on the plastic body, since a mechanical fastener would have been too intrusive on the flow and/or risk collapsing the walls of the tube when tightened into place.

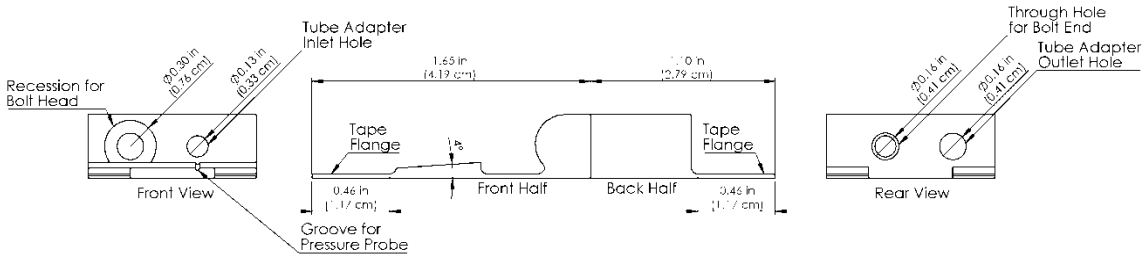

Figure 46: Focused View of the Two Sections of the Preston Tube Mount Body.

The rectangular rearward block and the sloped forward section were designed to be connected by thin, flat plastic tabs. The two tabs joining the sections at the middle gave the probe body the flexibility required to conform to the surface curvature of the wing model. Additional tabs were integrated at the front and rear of the probe to allow for a contact point where tape secured it to the wing model during use. Although tape was not the most efficient fastener for the probe body, it was the cheapest solution present and the least intrusive method on the exterior of the wing model's surface. Any form of mechanical fastener would have created disruptions or discontinuities in the wing model which would prematurely disturb the boundary layer flow. Alternatively, the use of the Cal Poly LSWT's traverse mechanism was a potential solution option, although the burden and risk of using the clunky system quickly outweighed any benefits it might have provided.

7.11 Infrared Camera Interior Mount

One final detail regarding the mechanical design of the experimental setup utilized for this thesis involved the placement of the infrared camera inside the wind tunnel test section. Any previous infrared thermography test to occur prior to this research was done so with the infrared camera located outside the wind tunnel peering through a viewport in the wooden ceiling panel—the same one that this wing model is intended to mount.

However, the wing model was inherently incompatible for use with the viewport due to its mounting location and orientation. Since acrylic window panels are distortive to infrared energy that passes through, the camera had to be mounted inside the test section to avoid that obscurity. Another plastic printed part was designed to fulfill this purpose and is visualized in Figure 47.

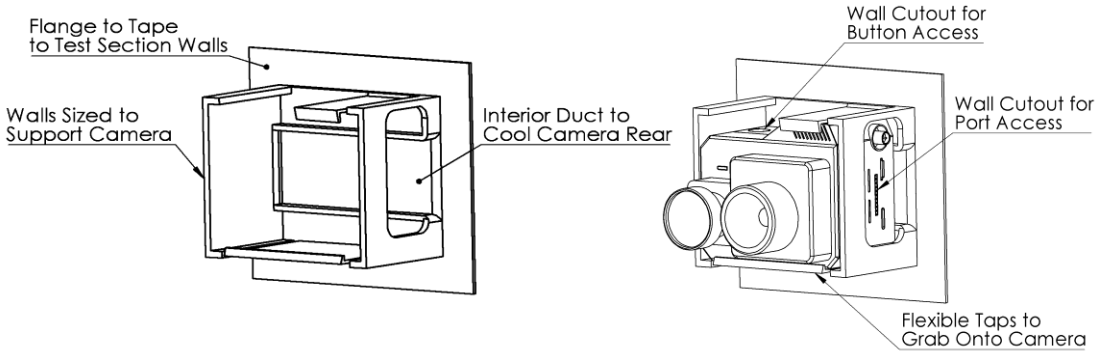

Figure 47: The Plastic Printed Part Used to Mount the Infrared Camera Inside the Test Section.

The custom encasing was designed specifically to accommodate a FLIR DuoProR: the infrared camera designated for use with this research project due to its known success in prior projects. Plastic walls were designed to snuggly fit around the camera body while leaving openings to access any buttons or connector taps. A large plate extended in all four directions at the backside of the mount, allowing for sufficient surface area for the mount to be taped to the interior of the test section wall. That allowed it to be placed freely at any location and take aim at any region of interest on the wing model. An additional feature was added to the mount in the form of a low cutout, where oncoming free stream flow could be channeled through the mount and pass by the cooling vents of the infrared camera.

Chapter 8

MODEL MANUFACTURING

In order to accommodate all the complexities of the model a variety of manufacturing methods had to be employed. In addition, the novelty of the aluminum 3D printing process resulted in errors which had to be solved and corrected to maintain a strong final outcome for the model. All the incremental steps required to produce the wing model and its system are outlined in the following sections.

8.1 Printed Parts Deformation

The parts for the aluminum center body were printed using a Selective Metal Laser (SLM) power bed system. Due to an error in the way the print process was set up, the raw parts all displayed notable amount of deformation in their cross-sectional profile along the spanwise direction. More specifically, the center of the parts had bowed inwards from the edges (Figure 48). In addition, when any two parts were stacked against each other, the two end profiles being misshapen relative to each other (Figure 49).

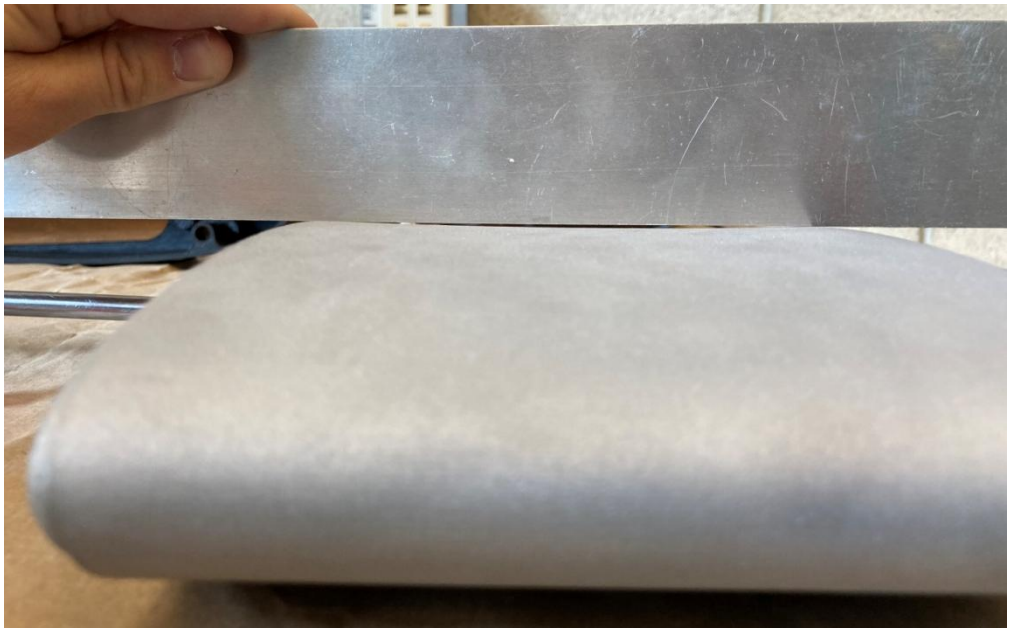

Figure 48: Visualization of the Inconsistency between the Cross-Sectional Profile of the Raw Aluminum Printed Parts.

Figure 49: Profile Mismatch between End Profiles of the Raw Aluminum Printed Parts.

The deformation was measured to only be on the order of half a millimeter in magnitude, which appears small upon visual inspection but would be absolutely detrimental to the aerodynamic performance of the model. The discontinuities along the span of the model's surface would be more than capable of prematurely forcing boundary layer transition. Sections 8.2 and 8.7 cover the steps that were taken to remediate this issue and restore the smooth, undisrupted surface finish of the model as originally desired.

8.2 Expanding the Aluminum

A crude yet functional solution to address the profile mismatch issue of the parts shown in Figure 50 was to expand the parts internally using an improvised turnbuckle system. One-inch long steel standoffs were purchased that featured a left-hand internal thread on one end and a right-hand internal thread on the other. Coupled with bolts of the respective thread type, turning the standoff would allow it to extend the bolt heads outwards and increase its length. The aluminum printer parts were just elastic enough to allow for these turnbuckles to expand their profiles outwards and mate flush with the next connecting aluminum part.

Figure 50: The Turnbuckle Mechanism Used to Forcefully Expand the Aluminum Parts and Remove the Discontinuity Created When Joining Them Together.

The turnbuckles, visualized in Figure 50 above, were placed on the side of the span where the male end of the wall key was located, such that it would be pressed up into the female end and held in place. A result of this process was artificial expansion of the airfoil profile to feature more camber than was designed originally.

8.3 Support Machining

The structural support rods described in Section 7.7 were manufactured from long low-carbon steel solid rod stock. They were cut to length using a simple chop saw and given their thread details on a manual lathe (documented in Figure 51). Once the primary steel support rods were finished, they were tested for fit and length with the six aluminum center section pieces. Figure 52 presents an image taken from that test, where the parts were put in compression and the recession built into the outer two aluminum parts to accommodate the hex nut can be seen. As for the secondary support rod extensions, the length to which these parts were cut varied with the length of the plastic end pieces they paired with (reference Figure 44).

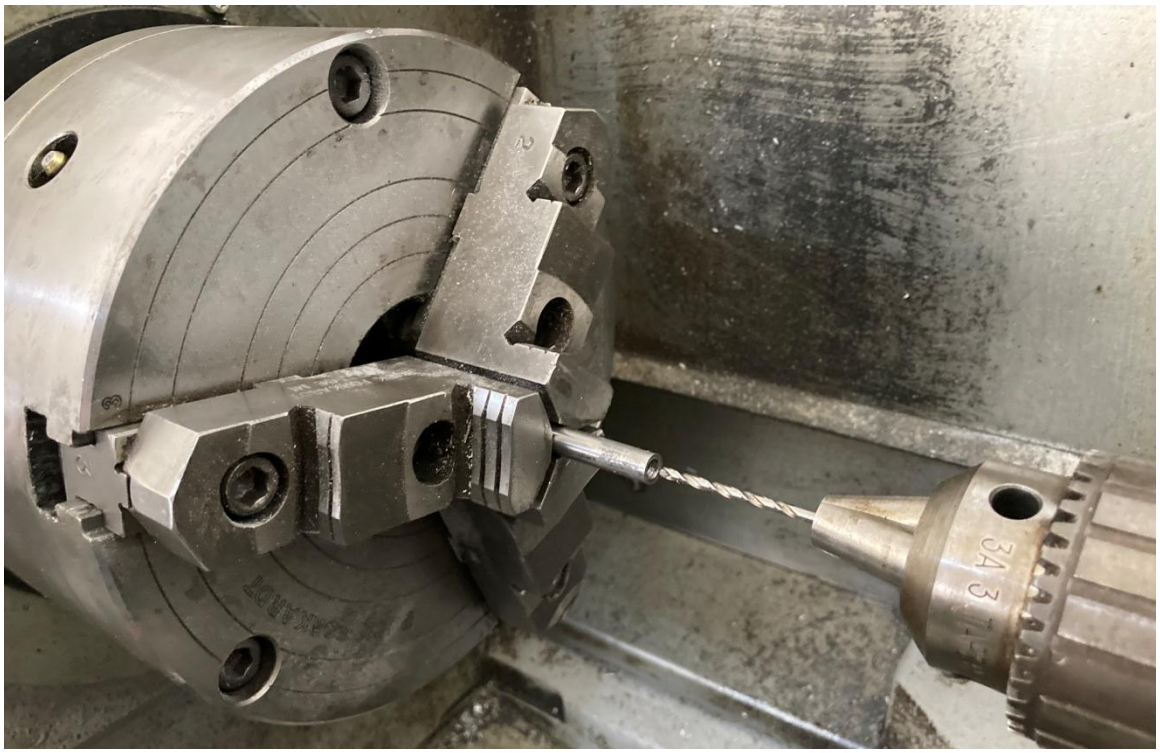

Figure 51: Center Boring the Central Steel Support Rods.

Figure 52: Testing the Fit and Length of the Primary Steel Support Rods.

All operations which relied on the manual lathe to turn a reduced diameter were done so using a spindle rate of 1,000 rotations per minute (RPM) and a feed per revolution rate of 0.0050 inches. The depth of cut was set lower to a value of 0.0030 inches to avoid chatter which was poorly mixing with the softness of the steel in use. A set of secondary support rod extensions were originally manufactured to the length where they would fit within the span of the 0^{o} sweep plastic end pieces and then a second set which were given another 1.50 inches in length to allow them to extend through the walls of the test section, as described in Section 7.7. The final result of the concentric threaded design is visualized in Figure 53.

Figure 53: The Final Manufactured Result of the Concentric Threaded Design of the Primary Support Rod and the Interchangeable Secondary Rod Extension.

Immediately following the completion of manufacturing for the structural support rods and their extensions, the design was statically tested to ensure its functionality. The concentric threaded design was un-simulated before manufacturing, so concerns lingered that it could have been too thin to hold up to the aerodynamic loads expected of the model. Before risking the integrity of the model by running it in the wind tunnel, a simple external test was performed to stress the supports.

The support rods were positioned on a table with a few of the aluminum print parts included to maintain the alignment and fixture points representative of the full model. A wooden tray was suspended from the four corners of the rods from some twine, with the contact point of

the twine located at the most distant span of the extension rods to generate maximum deflection. 60 pounds worth of steel weights were positioned on the wooden tray to simulate the maximum predicted lift force generated by the model. A visual of this setup is presented in Figure 54. The results of the quick test revealed no concern regarding the soundness and security of the structural support rod design.

Figure 54: The Setup Used to Statically Load the Wing Model's Structural Support Rods.

8.4 Static Pressure Tap Repair

As a benefit of using an additive manufacturing approach for producing the aluminum center section parts, the pressure barbs were pre-manufactured into the raw print of the parts. This meant that the protrusion inside the surface of the part, where the air-tight pressure tubing would mate to, was printed into the structure of the metal with the routing for the tap hole designed into the thickness of the aluminum's wall. Designed and tolerance properly, it would have completely removed the necessity to cut and install separate hollow tubes to act as pressure bards, as has always been done with student model in the Cal Poly LSWT. The finished product of those barbs are shown in detail in Figure 55, where the hollow opening can be seen at the tip which would route to the hole placed on the outer part surface.

Figure 55: The Static Pressure Tap Barbs Printed Into the Structure of the Aluminum Center Section Parts.

Unfortunately, the problems incurred with the SLM printing process did not end with the profile deformations. The overwhelming majority of the in-printed pressure barbs were blocked and non-functional upon inspection of all six parts received (four for use in the model, two created as spares). Overall, between the 96 taps printed throughout the six parts, only 19 of them could pass compressed air flow without blockage or restriction. This resulted in the necessity to strip away from aluminum printed barbs and install new ones. The individual steps that cumulate to the full repair process are outlined in the following sub-sections.

8.4.1 Static Tap Drilling & Alignment

The aluminum pressure barbs were forcefully removed by hand using a set of pliers, where thankfully the softness of the metal allowed them to be broken with only minor effort. After the majority of the barb and its support structure were picked away, a metal file was used to grind down the remaining material down to the surface of the interior wall. Inspection of the printed barbs after their removal showed that the blockage issues encountered seem to originate at the

elbow, where the barb would curve upwards and merge with the wall of the part. It is likely that the hole designed for these barbs was too small relative to the tolerances of the SLM machine used and as such could not be properly manufactured in the areas of high curvature.

A brief search through published recommendations for tap sizing suggested that any static tap with an inner diameter greater than 1 mm (0.039 inches) would have too much influence on the boundary layer flow to not disturb the onset of transition [5]. To size according to that reference, stainless steel hollow tube stock of 0.025 inch outer diameter and 0.013 inch inner diameter was selected for use in replacing the static pressure tap barbs. Once the original aluminum barb material was cleared, the surface holes had to be over-bored to match the diameter of the stainless steel tube stock.

A manufacturing jig was created which took inspiration and resemblance from the methods used to manufacture the static pressure taps on the other infinite wing model [23]. This involved placing the aluminum airfoil part on a rotating mount (Figure 56) where it could be locked into any angle of rotation desired. This technique was important to ensure the holes drilled into the wing model surface would always be kept truly normal to the local curvature. A small drill press was used to support the 72 size drills required to bore 0.025 inch holes through the aluminum wall. A digital level was incorporated to ensure the part was set to the right angle of rotation before each drill operation was performed. The angles used can be referenced in Table 5, which were extracted from the original CAD representation of the part.

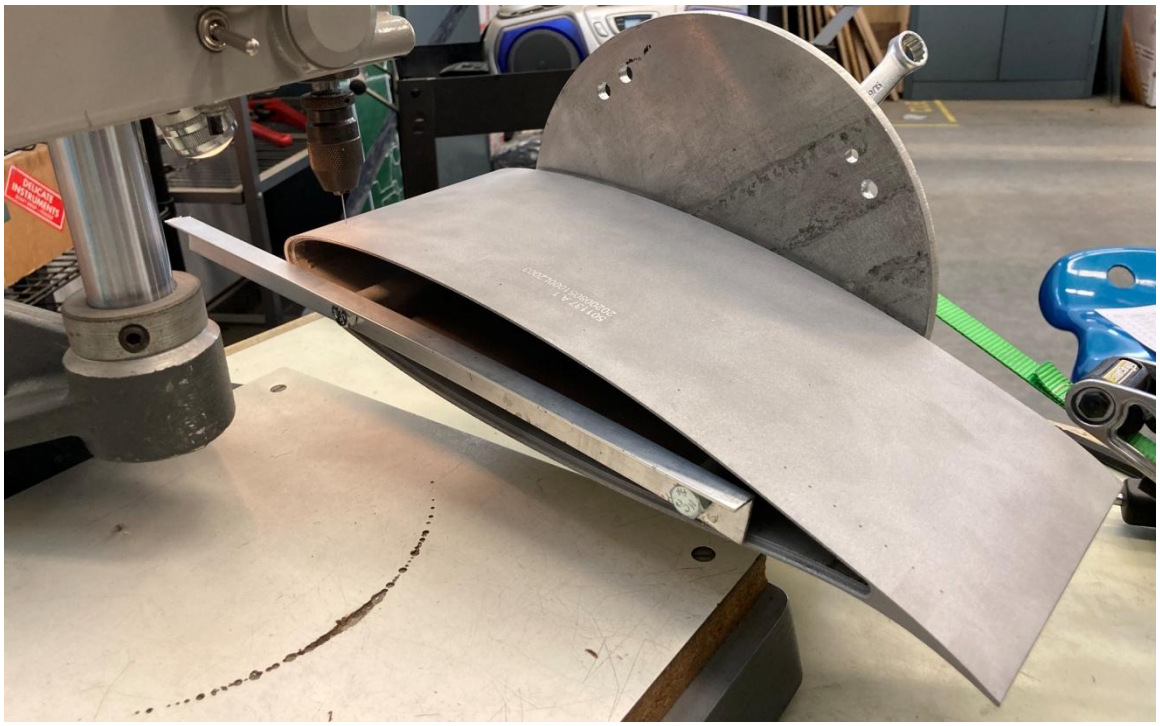

Figure 56: The Rotating Assembly Jig Used to Drill Pressure Tap Holes Normal to the Part Surface.

Due to the hardness associated with drilling into metal, the miniature-sized drill bits being used for this process were extremely prone to breaking under stress. As a result, some of the pressure tap locations were not able to be drilled out successfully. The final distribution of repaired taps amongst the four parts used for the aluminum center section assembly is listed in Section 8.4.3.

8.4.2 Barb Cutting, Cleaning & Installation

No documentation existed within the Cal Poly LSWT for a model that had integrated static pressure taps as small as 0.013 inches inner diameter before this project. The traditional technique for cutting pressure barbs is to snip the stock to length with wire cutters and then reduce the edges back to shape on an abrasive wheel grinder, since the mechanism of the pliers naturally deforms the thin walls of the material. However, attempting this process with the stock purchased for this project revealed a flaw in the approach: the inner diameter was small enough where the debris generated from the grinding wheel would get lodged inside the tubing and clog it up. To remediate this issue, a new technique had to be developed from scratch.

Safety wire ended up being the savior of this stage in manufacturing for the reasons about to be described. To start, safety wire of 0.010 inches outer diameter was slotted into the stainless steel tubing before being cut, as seen in Figure 57.

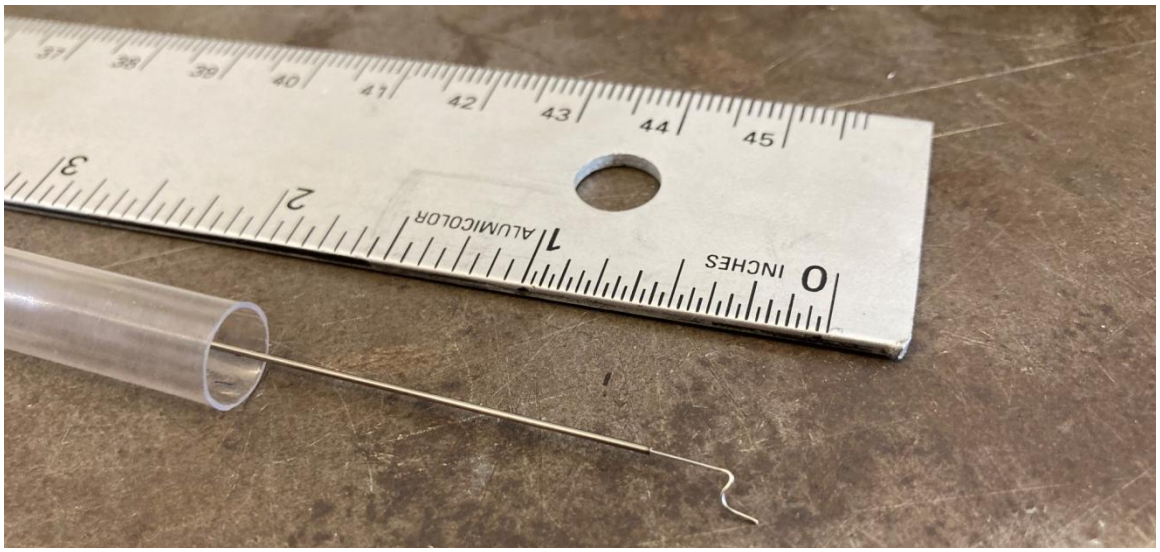

Figure 57: The Insertion of the Safety Wire into the Interior Thickness of the Stainless Steel Tube.

Although the walls of the tube would still be crimpled out of shape, the safety wire would help add to the effectiveness thickness resisting the shearing force. When the tubes containing the safety wire were pressed against the grinding wheel, the safety wire would prevent the debris from blowing back into the tube, avoiding the aforementioned issue. Grinding the second opening of the pressure barb would loosen the safety wire through the vibrations of the wheel's contact (reference Figure 58) and allow it to be easily removed by hand or with small pliers.

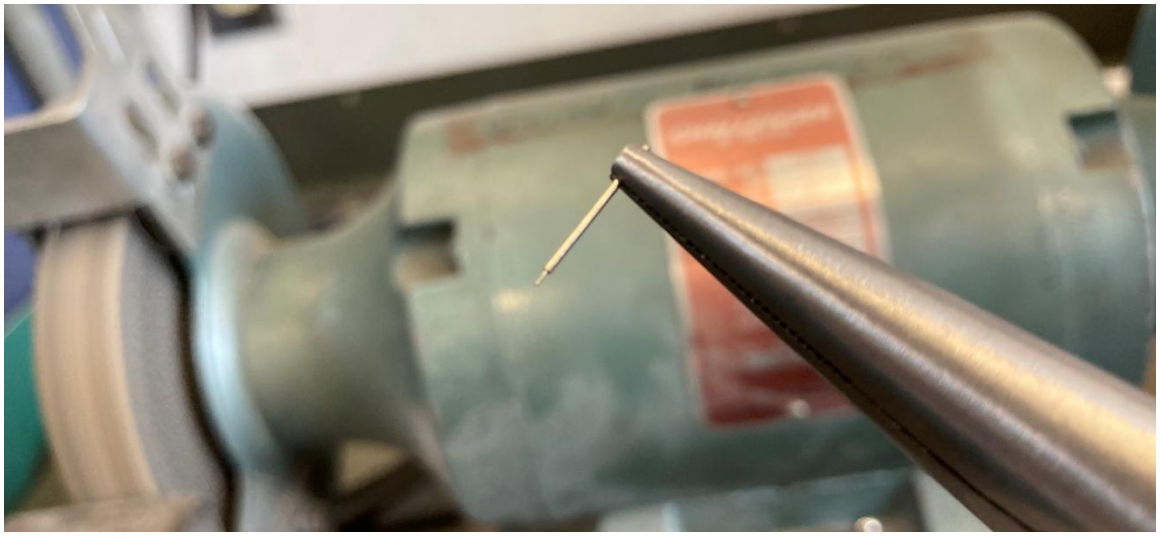

Figure 58: Visualization of the Loosening of the Safety Wire from Grinding the Second Side of the Stainless Steel Tube.

Following the removal of the safety wire, each cut and ground barb was still cleaned internally of any remaining potential debris using a second strand of safety wire. The process of pre-filling with safety wire was not a perfect method, but the success rate of machining the barbs increased substantially with the use of this technique. Once a barb was cleaned and checked for blockage using compressed air, it was deemed functional and good for installation into the model. To install into the aluminum center section parts, the barb would simply be press-fit into the drilled hole until its end face was flush with the outer surface of the aluminum. Each barb was also given a small perimeter coating of epoxy resin at the union with the interior of the aluminum wall, to ensure it would have a more permanent installation through the future.

8.4.3 End Result

Of the four aluminum center section parts converted to implement the new pressure barbs, not all 64 of the static tap locations could have their functionality salvaged in the end. Taps 14, 15 and 16 (the ones designed to run through the solid wall thickness at the trailing edge) were unable to be converted due to issues with accessibility in such a tightly-enclosed area. All four of the stagnation taps (Tap 2) were also unable to be bored open for an unknown reason, as multiple drill bits had broken in the attempts given. A similar issue was encountered with 5 other

locations amongst two of the parts. In the end, 43 of the original 64 taps were recovered in functionality following the printing errors encountered early on. The distribution of taps functional versus irreparable is illustrated in Figure 59, where the green regions marked those that had barbs installed and the red where barbs could not be successfully installed.

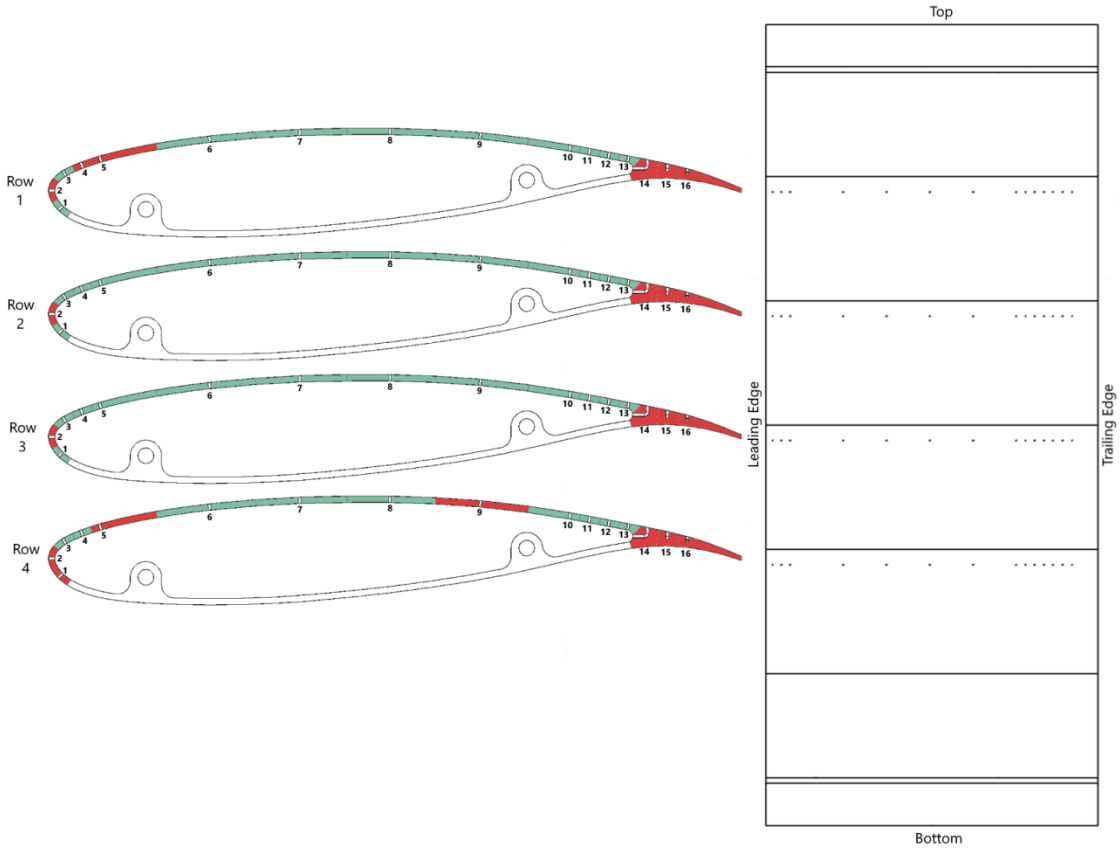

Figure 59: Distribution of Functional (Green) Versus Irreparable (Red) Static Pressure Taps at All Four Spanwise Locations.

8.5 Pressure Line Adapters

The digital transducer used by the Cal Poly LSWT had a connection manifold to its sensors made from 0.0625 inch outer diameter steel barbs. The barbs used on the interior of the wing model were much smaller in diameter, so an adapter had to be integrated to merge the two different sizes of pressure tubing together. Very few options were found online that could adapt down to as small of a size being utilized in this project and the cost to obtain a few dozens of those would've exceeded a reasonable working budget. The decision was followed to manufacture custom adapters specifically for use within this project.

8.5.1 Part Design

The final iteration of the pressure line adapters were made from 3D printed plastic, where the infill specification was set to 100% to create a solid plastic item. A conical protrusion with an end diameter of 0.0625 inches was designed into a square flange at the base. The conical part was where the pressure tubing connecting to the transducer attached while the square flange was added to make the part easier to hold and work with by hand. The attachment point for the smaller pressure tubing was not made from plastic, since the size was smaller than the tolerances of the printer in use. Instead, an additional set of the hollow stainless steel barbs (reference Section 8.4.2) was manufactured for use in the adapters. Overall, 96 steel barbs were made while 48 of those were used to make the adapters.

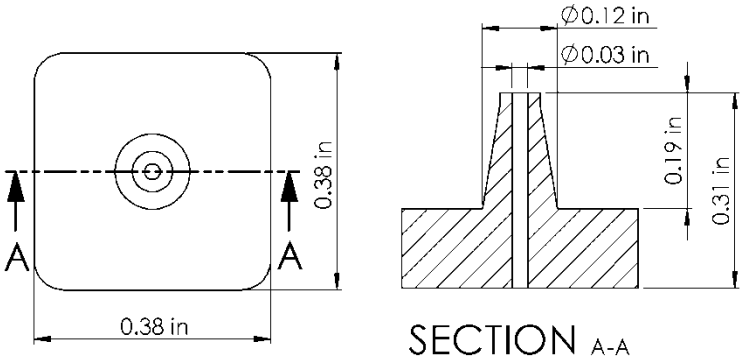

Figure 60: Cross-Sectional Drawing of the Custom-Made Plastic Adapter Body.

8.5.2 Printing & Assembly

The metal barbs were integrated by being press-fit into the plastic adapter bodies. First, a central hole was drilled through the plastic (see Figure 61) using the same sized drill bits seen in Figure 56. Once any debris plastic was cleaned out, the stainless steel barb was pressed in until it poked out slightly beyond the conical protrusion, leaving around half of its length to stick out below the opposite side of the square flange. With this approach, the pressure tubing coming from the model static taps connected to the stainless steel barb which carried all the way into the larger pressure tubing. As long as the seal between the larger pressure tubing over the conical protrusion was tight, it would create a leak-free means of adapting the pressure tubes from one diameter to another. A small drip of glue was added to the bottom of the square flange around the union of the steel barb and the plastic to maintain an airtight seal between the two. The dried glue also served helpful as a makeshift flange for the smaller pressure tubing to expand and seal itself around once pressed into place.

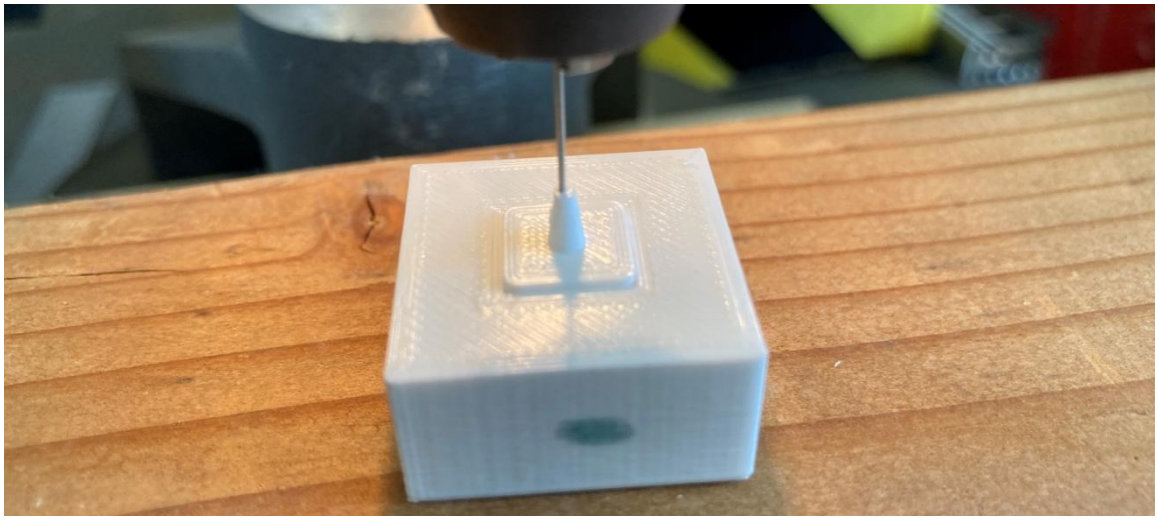

Figure 61: Drilling the Central Through Hole in the Plastic Adapter Body Using a Custom Made Jig to Keep the Part Secured in Place and Aligned with the Drill Press.

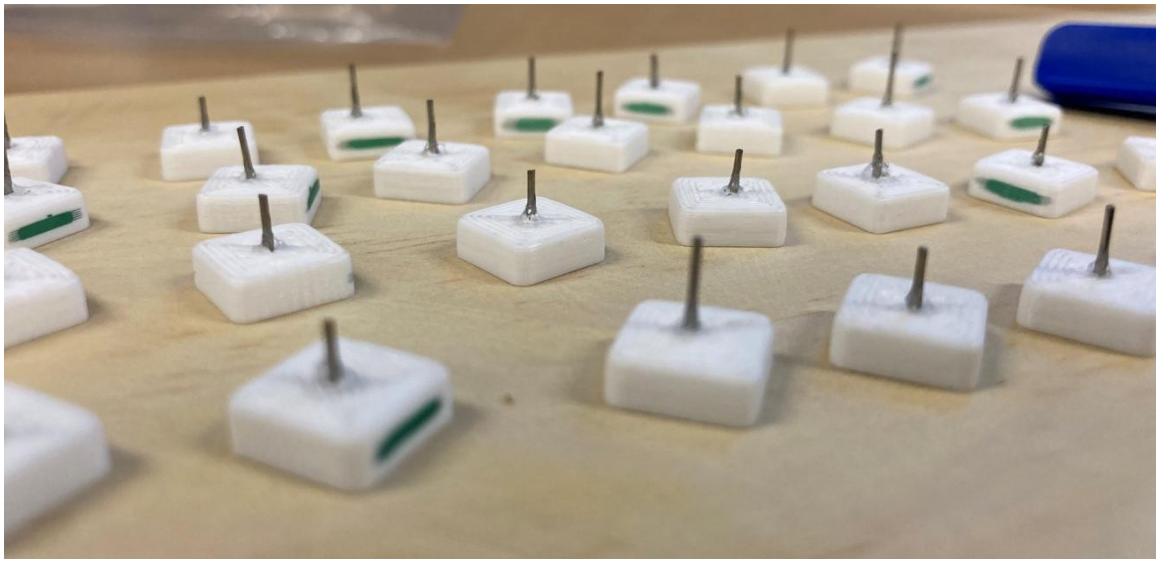

Figure 62: Sealing the Bottom Union of the Plastic Adapter Body and the Stainless Steel Barb with Glue.

8.5.3 Quality Check

Each individual adapter manufactured was tested for both the retention of compressed air flow (Figure 63) as well as the ability to hold pressure under pull of vacuum (Figure 64). If the manufactured adapter passed both of the quality checks, it would be marked with a dash of green marker to indicate it is cleared for use on the wing model. Any that displayed issues during the checks would be taken back to clean out and re-seal until they were functional or if unable to be salvaged: thrown out.

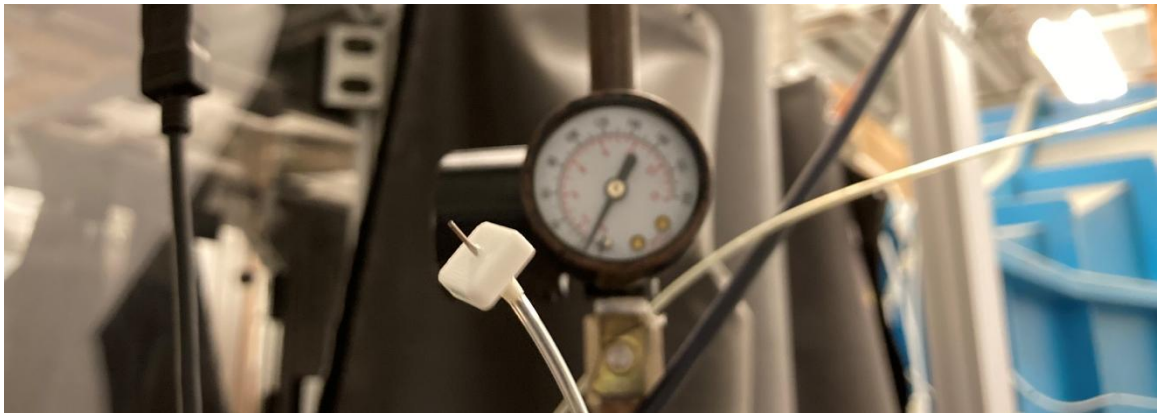

Figure 63: Checking the Pressure Adapter for Blockage by Passing Compressed Shop Air Through It.

Figure 64: Checking a Pressure Line Adapter for Leakage Using a Hand-Held Vacuum Pump.

8.6 Center Section Assembly

Following the repair of the aluminum center section parts to address the profile discontinuity issue and the static pressure barb issue, they were ready to be merged together to create the unified center section. The heating elements, pressure tubing and adapters would be installed into the individual pieces while still separate and accessible. At last the central structural support rods displayed in Section 8.3 would be used to align and compress the six parts together. From there, they would be permanently bonded together along the wall line.

8.6.1 Heating Pad Installation

The pre-coated adhesive backing on each heating element bonded strongly with the upper interior of the 3D printed aluminum surface, which was cleaned with acetone before application. The heating elements were aligned with their short edge pressed against the solid-filled region of the trailing edge, and the long side pushed as close to the row of pressure barbs possible without covering the epoxy glue at their base. The details of the placement are visualized in Figure 65 below and also match what is shown in Figure 40. Only the central four aluminum sections had heating elements installed. It was concluded that the outer span of the aluminum center section would not be used for infrared thermography during this research and,

as such, installation of the heating pads at those locations was not necessary. Should future students wish to re-configure the wing model to include the fifth and six elements, they will be easy to reach and integrate from the edge of the model.

Figure 65: The Placement of the Internal Heating Element within an Individual Aluminum Print Part.

Each heating element came with two wire leads which allowed for current to flow through the array of wiring within the pad. The initial decision was made to wire all of the heating pads in series with one another, with the idea that the higher resulting resistance of the system would allow it to heat at a slower and more uniform rate. Since the maximum temperature of the elements far exceeded the operation limits of the wing model, that seemed like a reasonable approach at the time. The wire leads between heating pads were joined using screw-on wire connectors, as seen in Figure 67. The total wire path was checked for continuity and once the center section was permanently merged together, only two open leads remained to allow for a 3-prong wall plug to be fitted as the model's built-in electrical connection.

An issue arose when the heating pads were tested for heat functionality after the center section was bonded together and vinyl wrapped over (reference Section 8.10). Given the high resistance of wiring the elements in series, the maximum temperature they were able to produce at the surface of the vinyl wrap was only around 80^{o}F, as measured with a laser thermometer. The reduced power of the pads was expected, but for the heat capacity to be that low was unplanned. The interior of the model had to be accessed to re-wire the pads into a configuration which would create less overall resistance to the current flow. All four elements were not able to

be placed in parallel with each other, because the ergonomics of accessing the connectors between the middle two pads was not feasible. This resulted in an unusual configuration where the upper two elements were wired in parallel, the lower two elements also in parallel and then those two group put in series. Figure 66 shows a simple schematic for how the final wiring scheme between the four elements was settled. The total resistance of the system was lowered by a magnitude of four, and the maximum surface temperature attainable was raised to around 130^{o}F to 140^{o}F when supplied with 120V of alternating current.

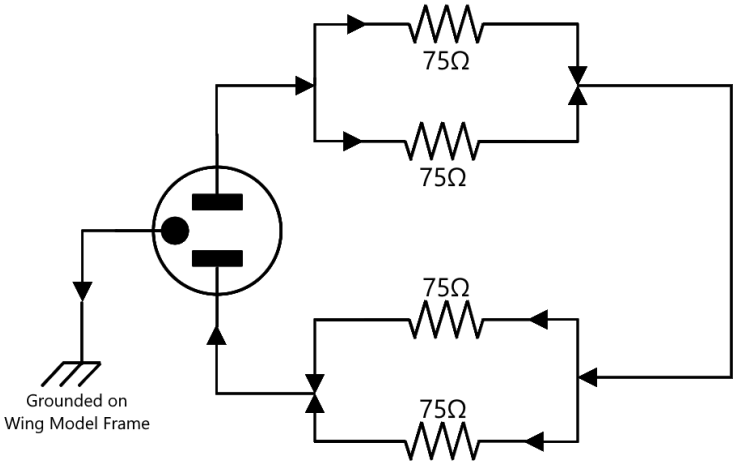

Figure 66: Final Internal Heating Element Wiring Scheme.

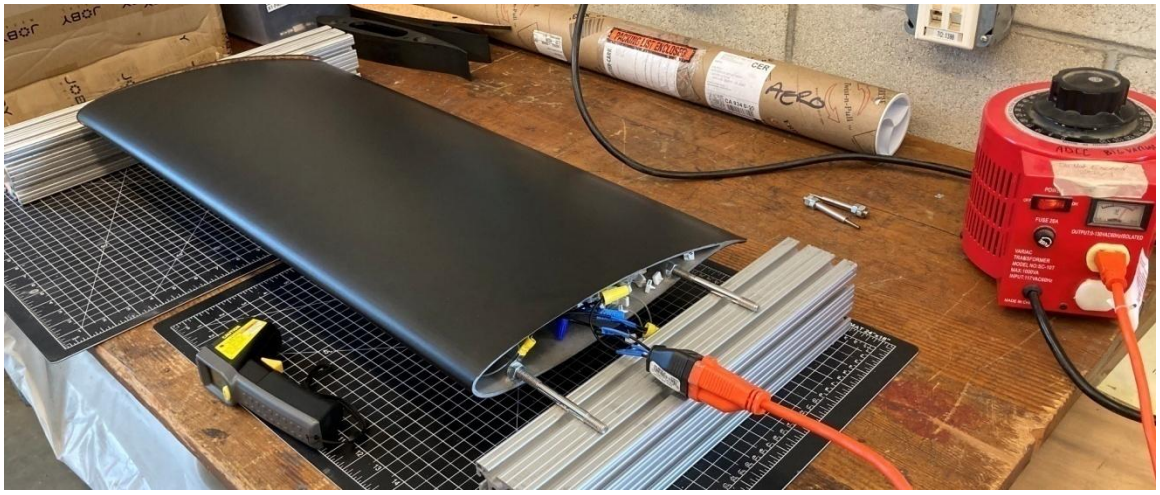

Figure 67: Image of the Revised Wiring Arrangement Being Connected Through the 3-Prong Plug and Tested for Maximum Attainable Steady-State Heat Capacity.

8.6.2 Pressure Tubing Arrangement

The spanwise distance from each pressure tap row to the outer edge of the top cork insulator was measured and used to cut the 0.025 inch inner diameter silicon tubing to length for each of the 48 static taps installed on the wing model (reference Figure 35). The tubes were fitted onto each of the hollow stainless steel barbs inside the upper aluminum wall with the custom-pressure adapters (reference Section 8.5) fitted to the opposite free end of the tubing.

As mentioned prior in this document, the row of static pressure taps with the span position closest to the top of the wing would be referred to as Row 1, whereas the furthest away would be Row 4. The tubing installed into each row were bundled together loosely using a plastic zip tie and labeled near the adapters with a paper tape flag to denote which row number they belonged (see Figure 68). Once all four sets of tubing were organized and the heat pads installed, the center section would be ready to be bonded together.

Figure 68: The Arrangement of Pressure Tubing, Adapters and Heating Pad Wires Before Bonding the Aluminum Print Sections into the Unified Center Section.

8.6.3 Bonding Together

To ensure that the aluminum parts would remain permanently affixed to each other, acrylic glue was lined along the interior walls of each part before compressing them together using the central support rods. In specific, ClickBond CB200-40 Acrylic Structural Adhesive was applied due to its known favorable properties with metallic surfaces. The glue fit nice in between the keyed grooves of the aluminum part walls, adding to the contact surface area of the adhesive and also helping serve as volume filler for the remaining gaps between parts. A 24 hour period was allowed for the glue to fully set and dry before being worked on, as described in Section 8.7.

8.7 Surface Preparation

The non-uniformity in the cross-sectional profile, as exhibited in Figure 48, still remained in all six of the aluminum parts now comprising of the unified center section. Material on both the upper and lower surfaces of the wing model had to be removed to lower the wall thickness to a height where the inconsistency was no longer apparent. This operation was performed using a Vixen file (reference Figure 69), which was used to shave material from all exterior surfaces.

Figure 69: The Vixen File Visible with the Aluminum Center Section at the Early Stages of the Coarse Material Removal Process.

No protection was provided to the static pressure taps during this process. It was unknown at the time if the filing process would permanently damage the stainless steel barbs. Once the filing process was complete, time was taken to hand-sand the surfaces of the model using 200 grit sand paper to remove any blemishes and scratches created by the vixen file. A final pass of 400 grit sandpaper was performed to help polish the surface of the metal and prepare a better surface for the vinyl wrap to be applied over. The final result of the aluminum center section after all filing and sanding is visible in Figure 70 below.

Figure 70: The Final Exterior Quality of the Aluminum Center Section after Filing and Sanding.

8.8 Vinyl Layup

With the aluminum center section instrumented internally, bonded together and sanded down to a fine uniform surface quality, it was ready to be covered in the vinyl wrap. A 60 inch by 36 inch roll of 3M 2080 Series Matte Black vinyl wrap was purchased—enough material to cover the surface of the model twice. A wet layup process was performed using silicon-based adhesive spray fluid. Once the first layer was applied and smoothed out of any wrinkles or bubbles, it was left for 48 hours to fully dry and adhere. The second layer was laid up just like the first, although the friction generated by the vinyl-on-vinyl contact made it much more difficult and tedious to

smooth out than the first time around. A small wrinkle formed on the leading edge of the model, near the center span region, which could not be flushed out (see Figure 71). The final look of the aluminum center section with the vinyl layers applied and trimmed to size is viewable in Figure 72. Any surface imperfections or seams previously seen in the metal surface could not be identified or felt by hand through the vinyl coating.

Figure 71: The Crease in the Second Vinyl Layer That Formed on the Leading Edge of the Model.

Figure 72: The Wing Model With the Vinyl Coating Applied and All Accessory Parts Installed.

8.9 Cork Insulator Preparation

The cork insulator sheets described in Section 7.4.2 were manufactured using a laser cutting machine. The computer numerical capacity of the machine meant that it would produce a cut with far more accuracy than could be achieved by hand. Four identical copies of the parts were cut from a single large sheet of 0.25 inch thick cork.

Figure 73: Image of the Cork Insulators After Being Produced by the Laser Cutting Machine.

Perforations were hand-punched in the top cork piece to allow the electrical connectors of the heating elements and the pressure tubing of the static taps to pass through. The perforations were positioned in a way that would help keep distance between each set of tubing to maintain organization throughout the model's endured use. The holes accommodating the two structural support rods were created by the laser cutter during the starting operation.

Figure 74: Organization of the Electrical Wiring and Pressure Tubing Through the Perforations in the Cork.

8.10 Mounting & Alignment

The methods by which the wing model was installed into the tunnel replicate that which were planned and described in Section 7.8. The zero-sweep configuration of the model, as required by the objectives of this thesis research, had the special benefit of extending the structural support rods through the outside of the test section to be secured in place. The process by which the model was initially installed and checked for pitch-angle alignment is covered in Section 9.10.1 while the rotating plug used to control the pitch angle is reviewed thereafter.

8.10.1 Alignment Templates

The first time installation of the wing model focused on identifying and marking where the zero pitch angle position would be located. After being centered with the wooden ceiling panel above using the early cutout of the rotating support (reference 8.10.2), the wing was tilted side-to-side until it was as vertically aligned possible. That process involved taking hand measurements of the distances from the wing's leading and trailing edges—at both the top and bottom of the span—to the walls of the wind tunnel test section. The model was considered vertically aligned when the top and bottom measurements were equal and considered at its zero pitch position when the leading edge and trailing edge measurements were equal.

Once the rotating support detailed in Section 8.10.2 was fitted around the support rod extensions, the model was rotated so that different pitch angle measurements could be located and marked. A plastic template was manufactured on a 3D printer which centered itself on the two support rod holes drilled into the test section floor. Markings for different angles of attack between -6^{o} and 6^{o} were designed into the template such that sharpie markings could be drawn on the test section floor near the trailing edge of the model (see Figure 75). The trailing edge of the model bore the closest resemblance to a sharp point and as such made for the easiest discrete indicator for pitch angle measurement. Measurements were marked on the floor as small black dots in increments of 2^{o} such that the model could readily be rotated about its upper support to change the pitch angle configuration during testing.

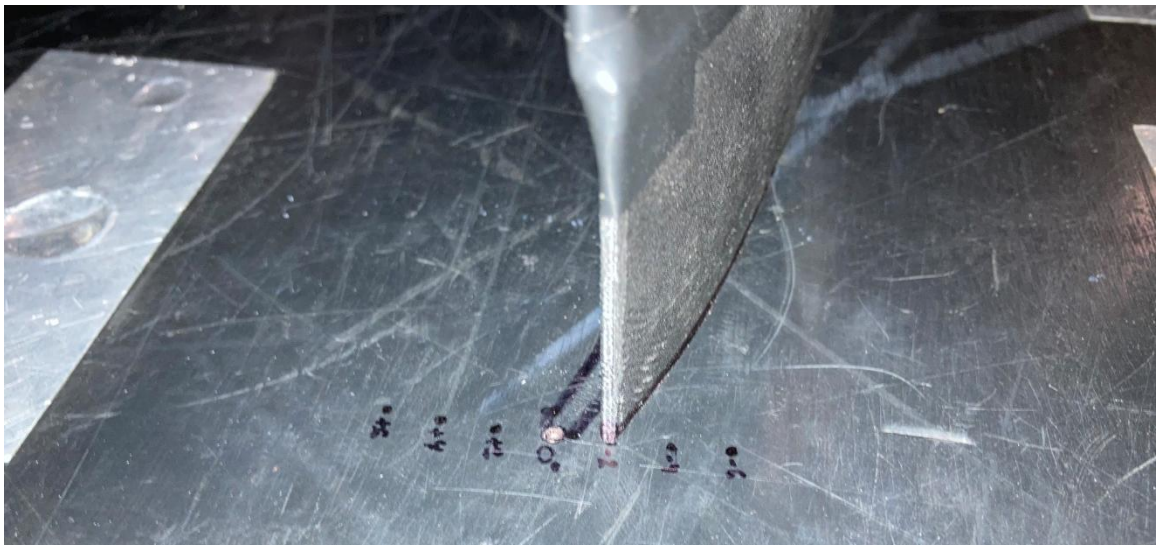

Figure 75: The Trailing Edge Pitch Angle Markers Made on the Test Section Floor Using a Plastic Template.

This assumed that the model was properly centered around the rotating wooden support and that the vertical tilt of the model would not deviate during adjustment. All testing performed with this model exhibited no evidence towards those concerns and the data collected at each position appeared to be strongly repeatable in the event of being repositioned in between tests.

8.10.2 Rotating Support

The circular wooden plug is the part which mediates support from the wing model through the wind tunnel test section. The use of circular plugs within the wooden ceiling panel of the Cal Poly LSWT is derived from the mounting scheme implemented by the designers of the lab's original infinite wing model [23]. After the process for locating the zero pitch angle orientation of the model, the wooden plug was drilled through to the wooden ceiling panel to add bolts which would permanently identify that location going forward. As each new pitch angle location was settled, another set of threaded insets would be added into the ceiling panel for bolts running through the plug to fix into. The two sets of holes were hand-marked with their corresponding angles, as visualized in Figure 76. The two steel support rod extensions can be seen fastened into place at the center of the assembly on either side of the opening which routes to the inside of the top plastic end piece.

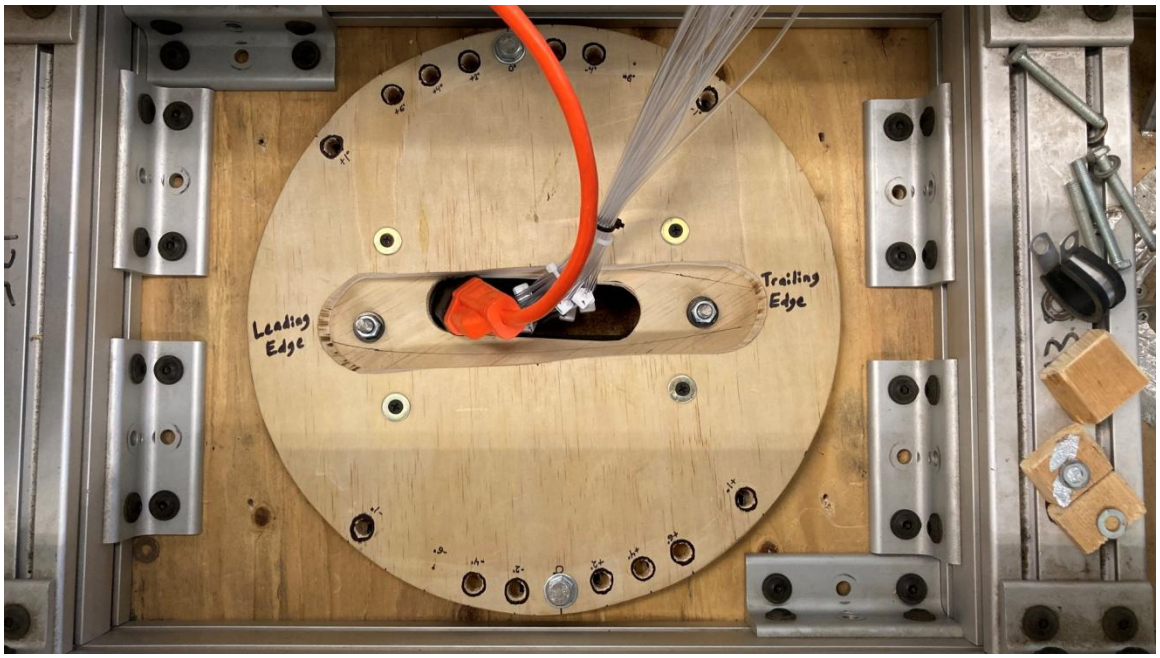

Figure 76: The Final Design of the Rotating Support on the Top of the Test Section with the Electrical Connection and Pressure Tubing Routed Outside the Model through its Central Cavity.

The system implemented where the wing model is secured to the rotating plug and the plug secured to the test section by the pair of marked bolts and inserts made for a convenient and easy to use system during testing. The specific steps for adjusting the pitch angle configuration of the model are outlined in Section 10.1. When the wing model is eventually adapted for use during swept wing testing, the functionality of the rotating support should not require any further modification or improvement.

8.11 Static Pressure Tap Inspection & Cleaning

As described earlier in Section 8.10 and visualized through Figure 72, the original vinyl layup completely covered the entire surface of the aluminum center section—including the static pressure taps. At the time of operation, no known solution was present to locate and accurately expose the static pressure taps through the vinyl without damaging the surround bits of coating. The chosen method to restore functionality to the static pressure taps was simply to cut away a strip of vinyl wrap at the corresponding spanwise locations. This process did not occur until after the infrared imaging tests were concluded.

Based on the successes had during the static tap repair process (reference Figure 59), the two rows with the most amount of salvaged tap were placed in the center of the aluminum center section to become Rows 2 and 3. Vinyl was only cut to expose those central two rows since they would together be sufficient in fulfilling the testing goals of this thesis. The process of cutting the vinyl involved carefully measuring a region which measured 0.75 inches in span away from each side of the static pressure tap row and marking it with tape, as seen in Figure 77.

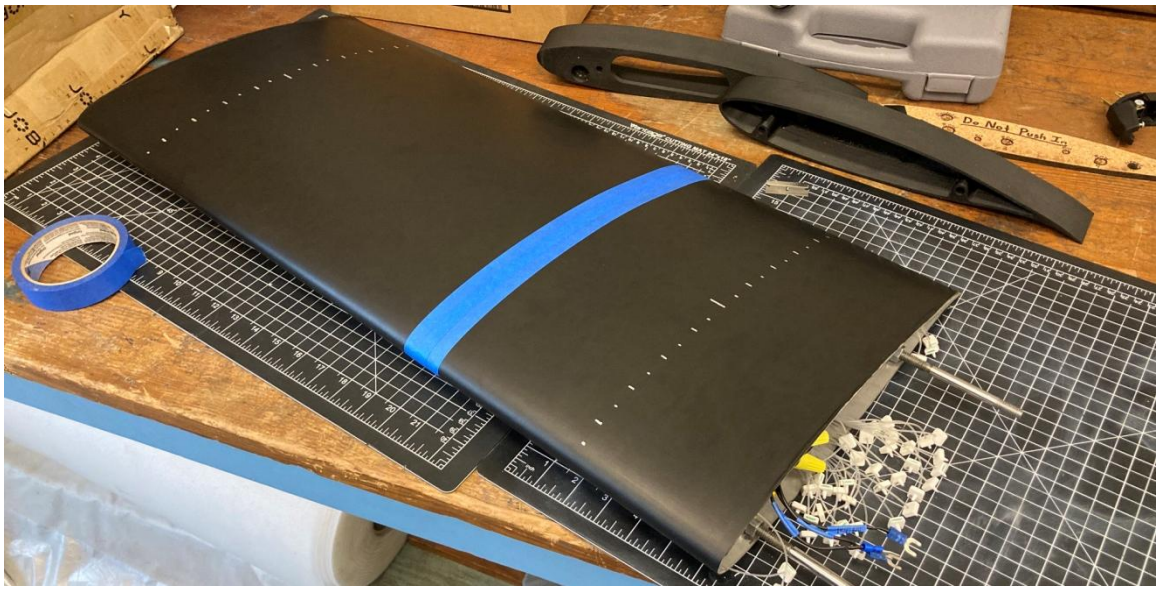

Figure 77: The Tape Marking Which Identified Where the Vinyl Coating Was Cut to Expose the Static Taps.

With the tape laid in place, the vinyl was cut by hand using a razor blade tracing along the edge thickness of the tape. This resulted in a clean cut which did not result in any tearing or deformation of the vinyl at the edges of the removal. The chordwise depth of the cut on the lower surface of the wing model only extended two inches behind Static Tap 1, since it would be unnecessary to further remove material where static taps are not located. The final look of the removed vinyl over Row 2 is visible in the following image of Figure 78.

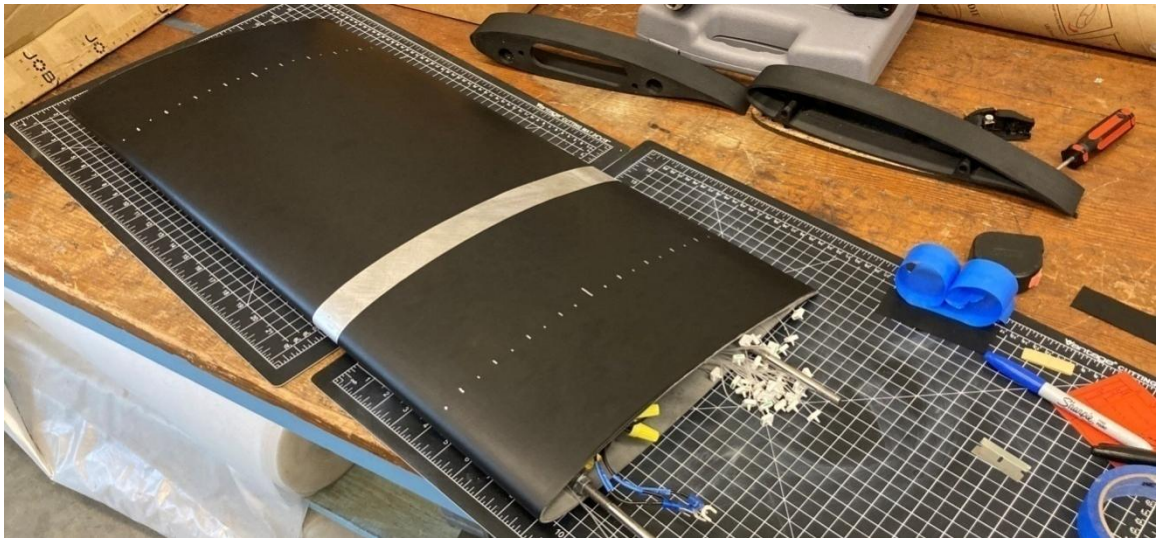

Figure 78: The Exposure of Static Tap Row 2 Following the Removal of the Vinyl Covering in That Area.

After the two vinyl strips were removed, it was uncertain whether the static pressure taps had survived the process of filing and sanding (reference Section 8.7). Initial checks performed by channeling compressed air through the adapters revealed that most of the taps were still fully functional or at least partially functional. Use of the 0.010 inch diameter safety wire originally purchased to manufacture the pressure barbs was used to clear debris stuck in the problematic stainless steel tubes pushed there during the material removal process earlier on. This simple method proved extremely effective as the debris was able to be dislodged and pushed through the interior end of the pressure barbs, opening them up to free flow when re-tested with compressed air. Each tap was also re-tested with the handheld vacuum pump to identify any leakage concerns in the system. Overall, all but two of the originally salvaged static pressure taps (Tap 6 on Row 2 and Tap 8 on Row 3) survived the manufacturing process in the end. The visualization of the final operation static pressure tap distribution for Rows 2 and 3 is represented by the graphic shown in Figure 79.

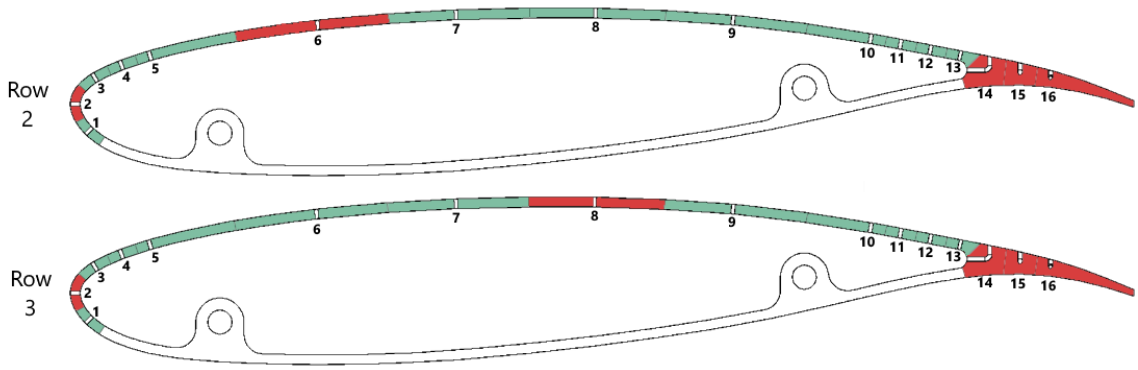

Figure 79: The Final, Operation Distribution of Functional (Green) Versus Inoperable (Red) Static Pressure Taps at the Central Two Spanwise Locations.

8.12 Preston Tube Assembly

To the hollow steel tube stock for the Preston Tube, the 0.012 inch outer diameter tubing was taped perpendicularly to a piece of T-slot aluminum. From there, a high-speed Dremel could chop through the hollow steel stock over one of the gaps to achieve the desired length. For future reference, the process of using a Dremel was attempted with the 0.025” outer diameter stock and

did not produce the same level of reliable results. The cut stock was then tested for flow and leakage using the necessary steel tubing adapter as shown in Figure 80.

Figure 80: Tabletop Assembly Used to Flow Test the Internals of the Preston Tube.

Following the successful testing of the cut tubing and its accessories, they could be integrated into the body of the Preston Tube. The plastic body was 3D printed to match the design reviewed in Section 7.10. From there, a hand drill was used to bore the bolt hole to its 0.25 inch specification and fasten the two halves together. The stainless steel barb was set into the groove at the front of the plastic body and secured into place with some electrical tape. The steel adapter was fitted with both sets of pressure tubing and compressed between the two halves of the plastic body. In the end, a robust assembly (Figure 81) was created which could be easily attached to the wing model and further re-configured just as easily.

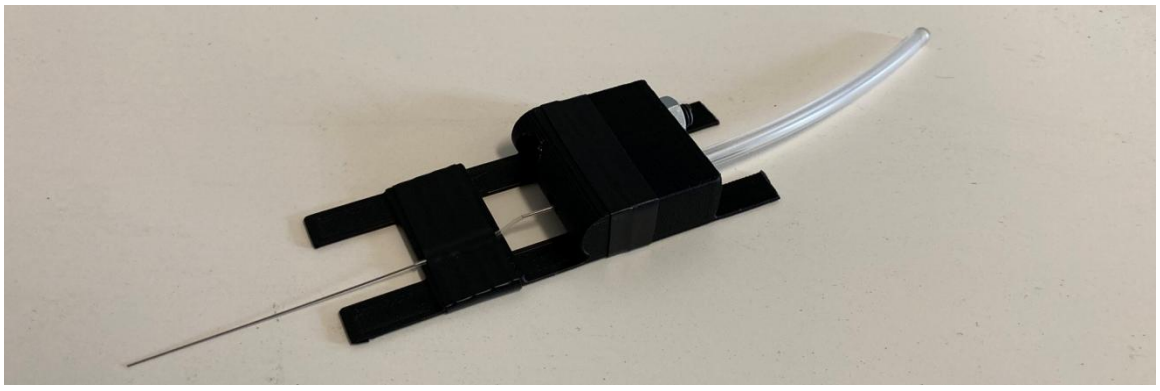

Figure 81: The Final Assembly of the Preston Tube.

Chapter 9

DESIGN VALIDATION & CHARACTERIZATION

9.1 3-D Scanning

Following the manufacturing of the aluminum center section, due to the addition of the turnbuckles and the material shed during the filing process, the assembly was no longer perfectly representative of its designed aerodynamic profile. Between, it was likely that the profile would change. The question to follow was how that could be measured and quantified. A visual light-based 3D scanning system was borrowed to measure the three-dimensional profile of the aluminum center section. This process was performed following the completion of the filing and sanding process but before the vinyl layer was applied.

The aluminum center section was suspended vertically by its support rods with its trailing edge lying on the table top. Numerous black and white circular stickers were applied over the model, the table and the support jig. These served as trackers which the 3D scanning software is familiar with and help enhance the way it extracts depth and orientation from the points its scans in real time. Lastly, the model was also coated in fine-quality baby powder, to help reduce the reflectivity of the bare aluminum surface from inducing error in the light-based measurements of the scanning system.

Figure 82: The Setup Used to Take 3D Scan Measurements of the Aluminum Center Section.

The hand-held camera sensor—specifically the Peel 3D product—was slowly traversed around the setup while the data is collected and analyzed was displayed real-time on a nearby laptop. In the end, a point cloud file was developed which the software was able to isolate the geometry of the aluminum center section—the part of interest in this process—from the supports holding it upright and the table it rested on. The OBJ data file produced after reducing the data was analyzed in SolidWorks to the results discussed in the following sub-sections.

Figure 83: Image Taken During the Process of Scanning the Aluminum Center Section Using the Hand-Held Sensor Provided Alongside the Rendering Software.

9.1.1 Airfoil Profile Comparison

The 3D scan point cloud was reduced to the cross-sectional profile at the same spanwise locations where static tap rows 2 and 3 are located, since that would be the region on the model where pressure measurements would eventually be taken. When comparing the scanned profile at both locations, the data suggested the two were functionally identical to each other. This was a reassuring discovery since it meant that the aluminum center section was able to maintain a consistent profile along its entire span despite all the reparation work that was performed on it prior. Figure 84 illustrates the comparison of the scanned profile, reduced to a singular outline, to the original design profile intended for the model.

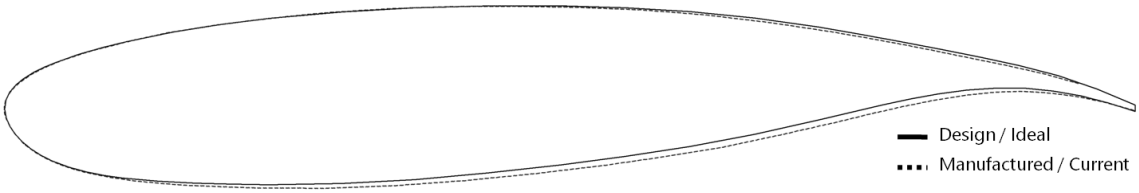

Figure 84: Comparison of the Measured Airfoil Profile (Dashed) to the Original Design Profile (Solid).

As expected from the addition of the turnbuckles described in Section 9.2, the measured profile is slightly expanded relative to the original design. The increase in camber is expected to change the flow qualities of the model, although likely not by much based on the findings of the data presented above.

9.1.2 Center Section Deflection

The 3D scan measurements were also useful in quantifying the degree of spanwise deflection the model picked up throughout the manufacturing process. The end profiles, at the top and bottom edges of the model, appeared to show no concerning deflection with only a magnitude of 0.02 inches end-to-end. The main concern is found at the center span instead, where the leading edge of the model deflects upwards by 0.16 inches from the end profiles and the trailing edge deflects 0.08 inches upwards (reference Figure 85). The data generated from the testing process would go on to not provide any conclusive indications that the deflections presented in this sub-section would negatively modify or inhibit the flow qualities of the model.

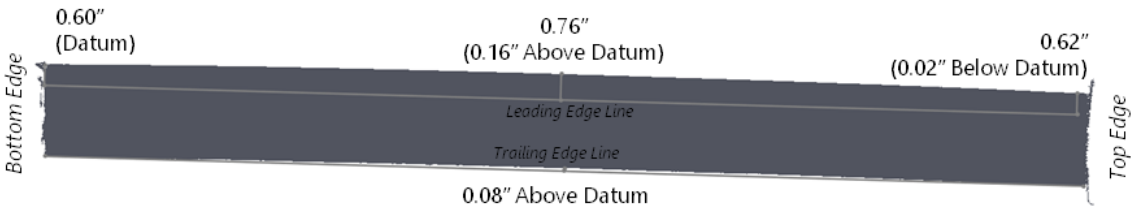

Figure 85: Characterization of the Spanwise Deflection of the Aluminum Center Section Based on the 3D Scan Measurements.

9.2 Surface Roughness Quantification

A Mitutoyo SJ-210 surface roughness sensor was used to aid in the characterization of the surface quality of the model. These details find more relevance with a project like this where boundary layer flow is the emphasis of the testing and can be highly susceptible to different magnitudes of surface roughness. The sensor works by using a small metal stylus with an extremely fine point that, when set to operate, will slowly retract in a linear motion and measure the vertical deflection experienced by the stylus as it traverses the surface its measuring. Greater magnitudes of vertical deflection—or inconsistent profiles measured along the path—seen by the stylus will correlate to a higher reported surface roughness value. This specific sensor reports its data in the value of µin which is the commonly regarded standard unit of measurement for surface roughness.

Figure 86: The Mitutoyo SJ-210 Surface Roughness Sensor Seen During its Calibration Procedure Using the Precision Sample Provided Alongside It.

The surface roughness sensor was utilized at various different points along the wing model's manufacturing timeline. In the end, surface roughness was able to be quantified for four different states of surface preparation encountered throughout this research project. Table 6 below lists the average recorded measurement for the following surface preparations:

- Raw 3D Printed Aluminum of the Individual Center Section Parts
- Filed and Sanded Aluminum of the Center Section
- Vinyl Wrapped Aluminum of the Center Section

Figure 87: Use of the Surface Roughness Meter to Measure the Raw Printed Aluminum (Left) and the Vinyl Covered Aluminum (Right) of the Wing Model Center Section Parts.

The measurements presented in the following table are averages reduced from a series of two to three measurements taken on each material type. In addition, the table presents the measured surface roughness value in both the chordwise and spanwise directions. Due to the anisotropic structure of 3D printed aluminum, the value for surface roughness is expected to vary depending on the orientation being measured along. This trend is confirmed in the following data, where the spanwise values are consistently higher than the chordwise values since that was the direction which the aluminum parts were grown by the SLM printing machine.

Table 5: Comparison of Surface Roughness for Different States of the Wing Model Material Surfaces.

Surface Type	Un-Sanded Aluminum	Sanded Aluminum	Vinyl Covered
Chordwise Direction	259.8 µin	52.5 µin	47.8 µin
Spanwise Direction	354.6 µin	53.3 µin	52.1 µin

While no specific usage was identified for the data presented in Table 5, a qualitative look at the information helps gauge the effectiveness of the surface preparations in reducing

roughness. In addition, the data also helps provide some insight into the similarity of surface roughness between the vinyl and the sanded aluminum, suggesting that the quality of flow over the two surfaces should not be concerned by comparably equal measurements taken, as would become relevant in Section 11.3.

9.3 Vinyl Layer Thickness

When the strips of the vinyl coating were removed during the process recounted in Section 9.11, one of those samples was kept to take a quick measurement on. A digital micrometer was used to measure the thickness of the two-ply vinyl exterior coating (Figure 88) to get a qualitative impression as to how much thickness is present in the insulation layer.

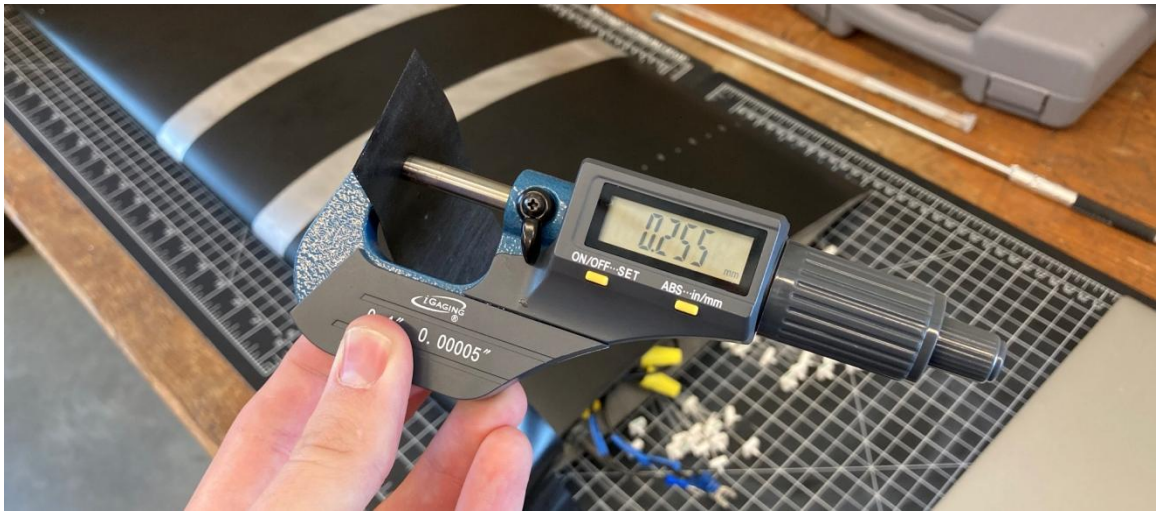

Figure 88: Measuring the Layer Thickness of the Exterior Vinyl Wrap Coating.

This question had come up during the initial design phase of the model to potentially supplement some transient thermal simulation work being planned. Even though the prior two infrared thermography models used an identical material and layup approach to this wing model, the thickness of the coating was never measured during the previous test campaigns. The removal of the vinyl strips during the latter portions of this research revealed that the effective thickness of the vinyl insulative layer is 0.01 inches (0.255 mm).

9.4 Internal Element Heat Distribution

During the design phase of the wing model, it was uncertain how well the aluminum structure would allow the heat generated by the internal elements to uniformly settle across the entirety of the upper surface. The four internal elements could only cover so much surface area and as such, portions of the model would have to rely on conductive heat transfer throughout the wall thickness of the aluminum to be pre-heated before testing.

When measured with an infrared thermometer, the center-chord of the aluminum center section will stabilize at a surface temperature between 130^{o}F and 140^{o}F after 10 minutes worth of pre-heating from starting at ambient temperature. The time required to heat the model was extremely consistent and repeatable, so much so that it helped influence the operational standard described in Section 10.3.1. Measurements made using the infrared thermometer indicated that, at steady state conditions, the leading and trailing edges would not exceed any more than a 20^{o}F temperature differential from the center where the heating elements are located. That translates to an upper model surface which exceeds a surface temperature of 100^{o}F, a value already greater than what was achieved and made successful during the Validation Model (Section 4.1) and Ducted Nacelle Model (Section 4.2) tests.

Images taken by the infrared camera during the pre-heating process clearly visualize where the underlying heat sources are positioned within the model (Figure 89). However, after a minute or two of heating, the visual temperature gradients are no longer identifiable.

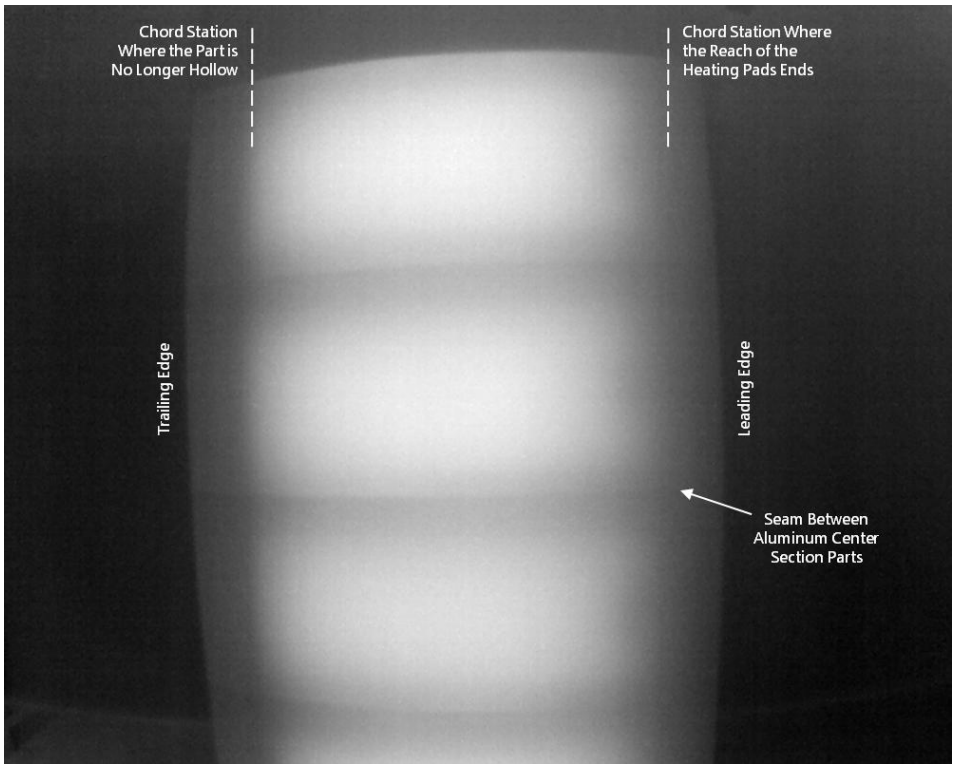

Figure 89: Infrared Image Taken Approximately 30 Seconds After Powering On the Internal Heat Elements.

The seam between each of the individual print parts of the aluminum center section can still be identified along with the chordwise position where the model is no longer hollow inside. Despite that, the impact on the resulting infrared images that visualize boundary layer transition (as reviewed in Section 11.1) did not suggest any issue was present with the pre-heated thermal gradient of the model. While the information may be useful for future design studies, the discrete sizing of the internal heating elements did not inhibit the quality of results gathered.

Chapter 10

TEST METHODOLOGY

Based on the design decisions made regarding the manufacturing of the model, it had to undergo a few minor configuration changes throughout the testing process to accommodate all the planned goals. The biggest change was the removal of some of the vinyl wrap layer to expose the static pressure taps, since it was initially installed to cover the entirety of the wing model's surface. Outlined in the following list are the order by which the model was tested and the modifications that were made to it with each step.

1.) Collect infrared images to show location of boundary layer transition with vinyl wrap and internal heating elements. Run tests for various angles of attack and air velocities, ultimately selecting three pitch angles which clearly demonstrate a change in boundary layer transition onset.
2.) Collect Preston Tube total pressure data over the vinyl wrap. Sweep the probe along the chordline at increments of 0.10 x/c for each of the three pitch angles and velocities tested in Step 1. Run infrared tests with the probe forward and ahead of the transition line to check for influence on the surrounding flow.
3.) Cut center two sections of vinyl wrap away to expose central two rows of static pressure taps. Perform full Preston tube testing incremented at each static tap location for all three pitch angle and velocity condition pairings selected in Step 1.

Following the completion of work detailed by the end of Step 3, the testing objectives for this thesis research would be satisfied.

10.1 Adjusting Pitch Angle

The pitch angle of the wing model was controlled through the rotating support discussed in Section 9.10.2. Adjustments to the angle of attack are very simple to make once mounted into the wind tunnel. The rotating support has a row of through-hole markers on both its top and bottom side, where each pre-determined angle corresponds to one marker within each row. The

support was originally manufactured to include positions for pitch angles of -6^{o} to 6^{o} in increments of 2^{o}. However, after testing the model and visualizing boundary layer transition appear with more sensitivity than expected, increments for -1^{o} and 1^{o} were added. For visual reference, Figure 76 shows the model secured at its zero pitch angle configuration.

In order to change the pitch angle of the model, the two bolts secured to the through-hole markers of the rotating support were removed. Then the hex nuts on the underside of the model's supports (below the test section floor) were to be loosened. The model was rotated along the arc-grooved cutouts until the trailing edge was aligned with the markings made on the test section floor. Following the rotation, the respective set of through-hole markers on the support should be aligned with the threaded inserts located beneath. The two bolts removed at the beginning can be re-installed at the new location and the under-floor hex nuts hand tightened again. Those few steps were all that was required to adjust the model's pitch angle—greatly reducing the time required to perform configuration changes during testing.

10.2 Visual Surface Markings

Once the vinyl wrap layer was applied, a necessity for visual chord-length indicators arose to track the location of boundary layer transition onset during infrared testing. The suggestion was made to use a silver Sharpie to draw markings on the surface, since the pigment in the ink comes off as reflective when viewed by an infrared camera. A similar approach was taken by the infrared wing model discussed in the background section of this document [9].

An arc length of 14.25 inches (36.2 cm) was measured between the stagnation point and trailing edge of the wing model's profile. This value was divided by 20 and used as the spacing value such that every 5% of the chord length could be identified with every tick mark drawn. Similar to the format used on a standard ruler, the height of each tick mark was varied to denote the value of its increment. The smallest tick marks correlate to a 5% value while the larger ones correlate to increments of 10%. The largest mark was placed at the center to easily distinguish the half-chord point on the wing model.

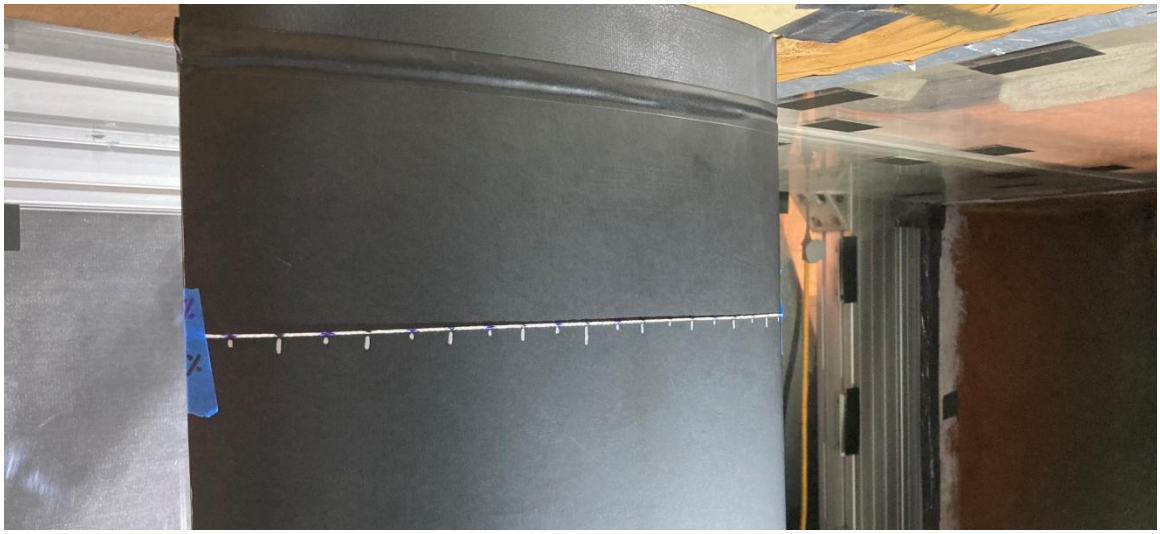

Figure 90: The Measurement Method Used to Mark the 0.05 x/c Indicators on the Model Surface.

To ensure the markings would remain equidistantly spaced and parallel to the span, a strand of twine was first marked using a set of calipers and then taped to the wing model, as seen in Figure 90 above. From there, the silver tick marks were made by hand at the locations marked on the twine. This was done on both halves of the model surface, just outside the spanwise location of the outer-most internal heating elements. The presence of the markers provided a clear visual reference during the remaining infrared imaging tests, helping to quantify the location of boundary layer transition onset (see Section 11.1).

10.3 Infrared Imaging Process

The infrared thermography process was the heart of this project and one of the two main testing goals established from the start. In thanks to the design and manufacturing efforts put into the model up front, the testing process is far more streamlined than ever before in the Cal Poly LSWT. There are essentially three phases to infrared thermography testing: setup and pre-heating, image collection and image processing. Each of those is covered in more detail in the following sections.

10.3.1 Pre-Heating the Model

As discussed in Section 7.6, the wing model was designed to implement a set of internal heating elements. These heating elements were installed and wired in such a way that they could be activated with the flip of a simple electrical switch. Characterization tests of the wing model demonstrated that the heat pads very consistently took around 10 minutes time—when starting with an ambient temperature model—to reach steady-state temperature. The aluminum center section of the model would be warmed to a temperature between 130^{o}F and 140^{o}F by the end of the 10 minute period, a more-than-sufficient value for infrared testing. Given the usual weather conditions at the Cal Poly LSWT, this would provide a starting temperature gradient between 50^{o}F and 60^{o}F, especially when tested at night. Current flow to the heating pads was controlled through the use of a variable alternating current (AC) power supply. The use of this device helps regulate the power output by the heating elements to ensure the model is not heated beyond a safe operating limit, as dictated by its material properties.

10.3.2 Image Collection Process

Once the model reached the desired starting temperature, the variable AC power supply was turned off and disconnected to prevent the heaters from running during the image collection process. The wind tunnel fan would be started immediately thereafter to minimize the ambient thermal losses of the model before usage. As the tunnel fan was ramping up in speed, the camera would be set to collect images on an interval timer of 2 seconds. For reference, the DuoProR camera used in this research was controlled through a Bluetooth phone application connection called *FLIR UAS*. The DuoProR owned by the Cal Poly LSWT was custom-modified by its manufacturer to implement a 45^{o} field-of-view lens, providing view of the majority of the aluminum center section's area but not all of it (reference Figure 39). The position was biased slightly upwards from the center-height of the test section so that it could see the silver tick marks implemented onto the top side of the model, as discussed prior in Section 10.2.

Images were collected with the white-hot temperature gradient and without any other special configuration changes made through the controlling software. The application was used to tell the camera to save images simultaneously as both JPG and Radiometric TIFF file formats. The special feature of the TIFF files were that each pixel within the picture contained meta-data for the temperature recorded by the sensor, allowing for the images to be better adjusted in post-processing. That process is better discussed in the following sub-section.

A small monitor screen was connected to the infrared camera to allow real-time view of the state of the model. The developing temperature gradient created by boundary layer transition was clearly visible through the screen during testing and used to discern when the desired images were taken and the test run could be ended. The setup used is visible in Figure 91 below, where the wing model and infrared camera are seen in the test section with the screen and variable AC supply in the foreground.

Figure 91: Infrared Thermographic Test Setup As Seen from Within the Control Room.

At the start of every test run performed with the infrared camera, multiple values about the model's condition and ambient setting would be recorded. Table 6 lists those values which were recorded into a simple text file to be stored with the raw image files after they were extracted at the end of the day's testing process.

Table 6: Example Table of Values Recorded for Each Run During Infrared Thermographic Testing.

(Date of Test)	Model Temperature	Ambient Temperature	Air Velocity	Air Density	Pitch Angle	Start Time
Run 1	130^{o}F	13.9^{o}C	43 m/s	1.223 kg/m^{3}	0^{o}	2:49 pm
Run 2	130^{o}F	13.8^{o}C	32 m/s	1.223 kg/m^{3}	0^{o}	3:50 pm

The infrared thermography process produced its best results at night. Day testing revealed unavoidable ambient scattering of sunlight throughout the wind tunnel would be seen through the infrared camera. While boundary layer transition could still be visible, the contrast and quality of the images collected were noticeably more washed when collected during daytime. This could also have been a result of the cooler ambient temperatures encountered at night, increasing the differential of the model compared to daytime operation. Nonetheless, all the images shown in Section 11.1 were accordingly taken at night to get the best quality possible. In addition, all lights in the lab and control room would be turned off while the camera was recording to further reduce reflections seen by the camera through the acrylic windows in the background.

10.3.3 Image Enhancement & Annotation

The radiometric TIFF files were imported into a program called ResearchIR (a FLIR product designed for use with their cameras) to process the images taken during testing. The only modification made to the images was a simple contrast enhancement, where the temperature histogram was right-shifted to offset the lowest value pixels. This process would narrow the minimum and maximum temperature difference presented within the picture, enhancing the shading and contrast of the gradient captured on the model surface. The benefit of this process is visualized through Figure 92, which shows the difference between the raw and enhanced image alongside the corresponding histograms. For note, the numerical values listed within the histograms are the digital save-state of the temperature readings seen by the camera sensor but were not displayed in the form of an actual temperature value.

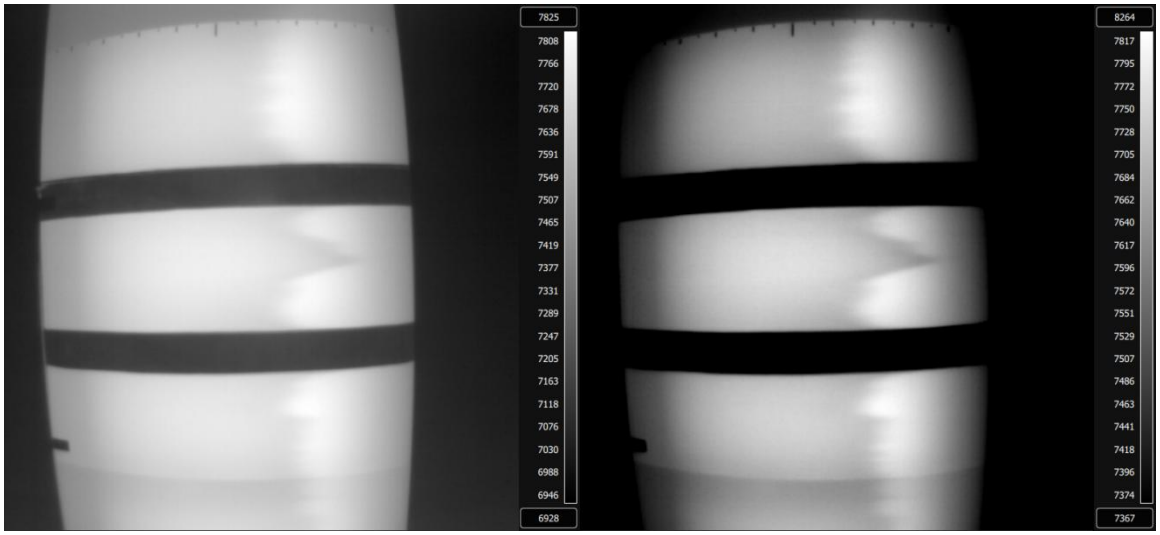

Figure 92: Comparison of a Raw Image (Left) to a Contrast Enhanced Image (Right).

With the contrast enhanced on the images to increase the visibility of the surface effects, they would be exported from the program as a simple PNG file. A template outside of ResearchIR was developed to add text annotations to each exported image, as seen in all the Figures displayed in Section 11.1. The annotations would highlight some of the tick mark chord-line values, the direction of free stream flow, the flow velocity and temperature conditions as well as the pitch angle configuration of the model. Those values were transcribed from what was recorded during the live testing process, as stated prior in Section 10.3.2.

10.4 Pressure Measurement Process

The process of collecting pressure data on the model was far more tedious and time consuming than the infrared imaging testing process. Pressure measurement was done in two stages: the first where solely the static pressure distribution was measured and the second phase where the Preston Tube was implemented and utilized. This Section, 11.4, discusses the process by which pressure data was recorded through the digital pressure transducer. The methods presented within the following sub-sections were held consistent for both the aforementioned phases of pressure testing. Section 10.5 below discusses the specific processes by which the Preston Tube system was implemented to the model and changed between testing.

10.4.1 Sampling Configuration

All pressure measurements collected through the Cal Poly LSWT were done so using a Scanivalve ZOC33 digital transducer. The instrument had 64 open sensor ports on it, with the specific setup use for the static distribution testing illustrated in Figure 93. By default for all tests in the Cal Poly LSWT, the tunnel's built-in total and static pressure taps occupy the first two ports on the transducer. Ports 3 through 26 on the transducer were occupied by the tubing connected to the wing model. All the static taps for Row 2 were connected first and in ascending sequential order—leading edge to trailing edge—with the same for Row 3 to follow. Even though two taps between rows 2 and 3 were damaged during the filing and sanding process, as discussed in Section 9.11, they were still connected to the transducer for better organizational sake.

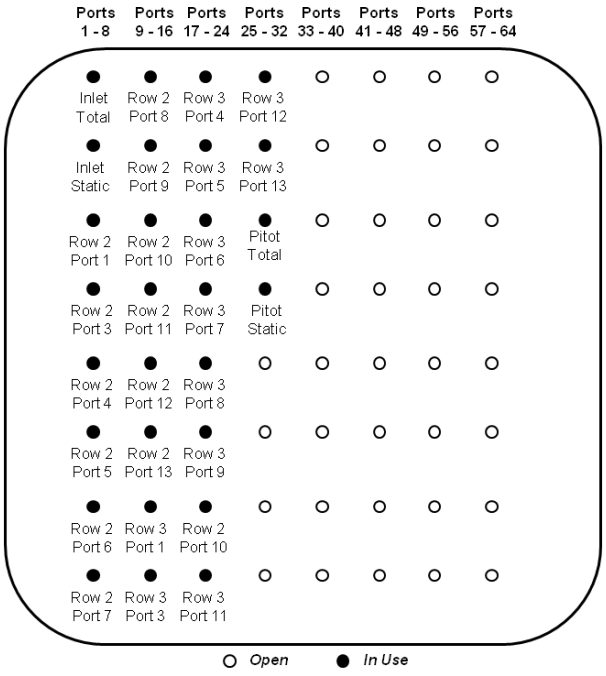

Figure 93: Digital Pressure Transducer Connection Scheme for the Static Pressure Distribution Testing.

The pitot-static probe installed through the floor near the wing model was connected to ports 28 and 29, 12 inches upstream and 14 inches away from the leading edge. All data reviewed in Section 12.2 would utilize this probe for both velocity calculations and as the static-pressure reference.

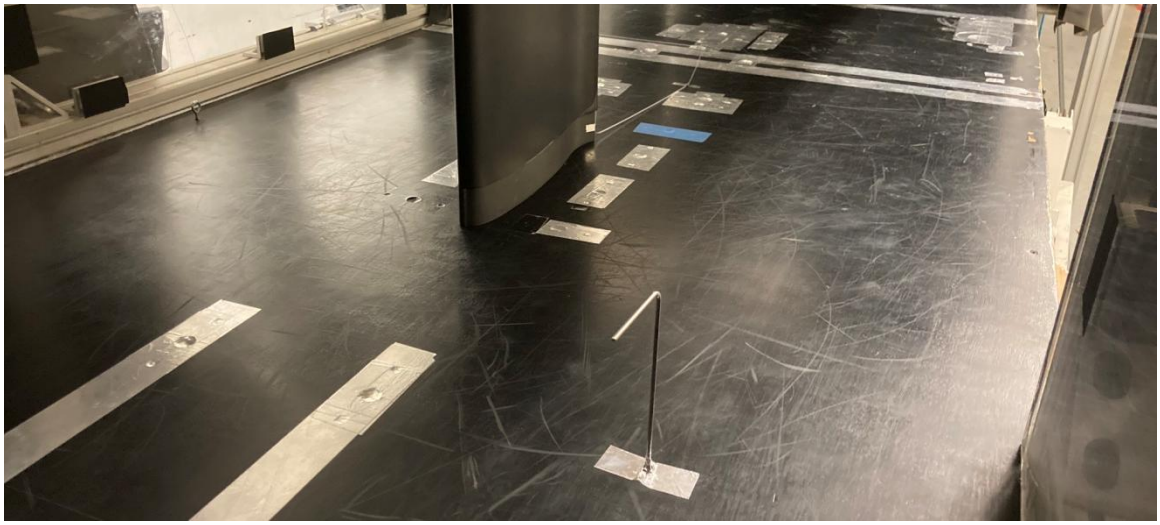

Figure 94: View of the Pitot-Static Probe Installed in the Test Section Floor Near the Wing Model.

Pressure measurements were collected through the use of the LabView UI developed for the Cal Poly LSWT. For each set of data, 250 points were collected with an interval period of 250ms. Each data point was set to average 10 frames of data, which implied that the transducer would sample 10 times within the 250ms period and average all the values together to output the single value recorded. Data for each run was exported of .mat file type for later reduction through a custom-written MatLab script.

10.4.2 Collection Pattern

For every mechanical configuration set in the test section—pitch angle and Preston tube location—data was always collected in the same sequence. Three different free stream velocities would be run and recorded with each mechanical configuration. Those velocities would be collected twice back-to-back to ensure that the repeatability of the data could be checked and quantified later during the reduction and analysis stage of the project. Table 7 shows the run-by-run process by which data was collected. This process would be repeated every time the Preston Tube was relocated (see Section 10.5) or once all data for a given pitch angle was successfully acquired. The pitch angle would then be adjusted and the entire process repeated.

Table 7: Sequence of Data Collected for Each Mechanical Configuration Tested.

	Run 1	Run 2	Run 3	Run 4	Run 5	Run 6
Air Velocity	40 m/s	30 m/s	20 m/s	40 m/s	30 m/s	20 m/s

10.5 Use of the Preston Tube

The structure of the Preston Tube was designed to be secured to the model with tape. The half-inch long pair of flanges at the front and rear of the plastic body provided adequate contact area for the tape to adhere the probe to the model's surface. Aluminum tape had to be used as it was the only type adhesive enough to securely attach the probe body without causing any damage to the vinyl material. During the full Preston Tube pressure testing process, the was traversed along the chordline of the wing model at each static tap location. Only static taps 3 through 13 were tested, since the probe was not designed to reach into the leading edge and taps 14-16 were non-functional anyways.

Figure 95: Preston Tube Secured to the Surface of the Wing Model.

The Preston tube was positioned on the wing model in such a way where the tip of the hollow steel tube was aligned with the reference static tap in the chordwise direction. The probe could not be positioned with the tube directly behind or overlapping the static tap, as it was found

the two would interfere with each other and produce skewed readings. This positioned the head of the probe 0.40 inches (1.02 cm) away from the static taps in the spanwise direction.

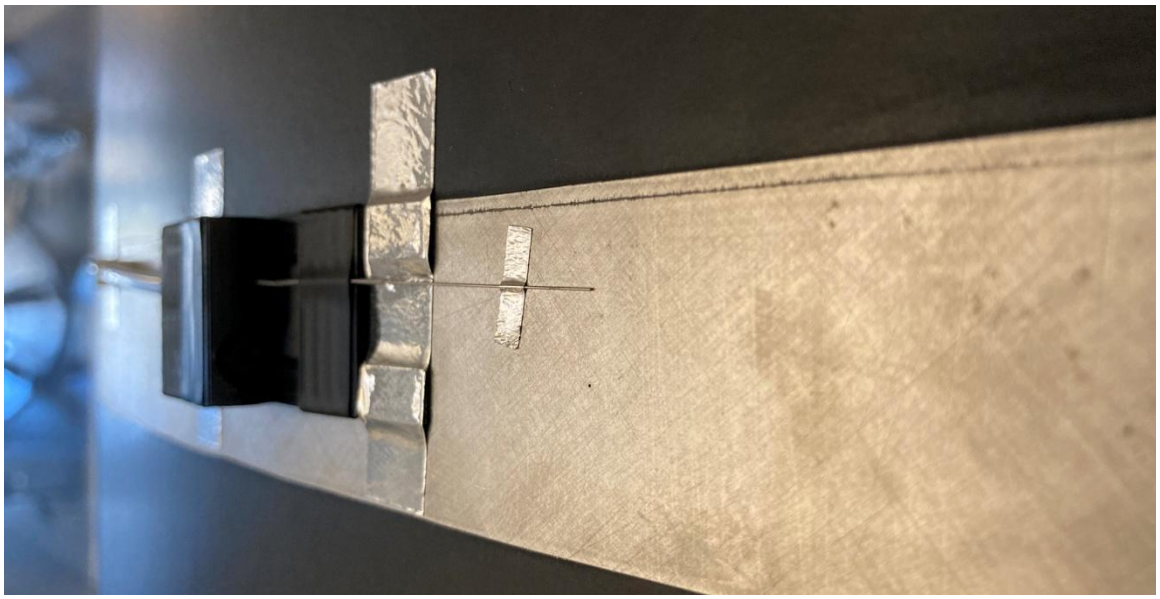

Figure 96: Close-Up Image of the Preston Tube Mounted with the Probe Tip Above a Static Pressure Tap.

The Preston Tube would always have a small piece of tape attached to the hollow steel probe head. This served the function of ensuring the hollow steel tube would always be pressed down against the surface of the wing model in assistance with the angled plate of the plastic body. That specific issue was only ever a concern at static tap 3 where the geometric curvature was still relatively high. In addition, it likely helped prevent the extremely light-weight probe head from lifting off the surface when exposed to maximum velocity air flow. Should the opening of the probe end not be resting on the model surface, it would no longer be capturing the surface interaction of the boundary layer and thus measure incorrect and unusable data.

On occasion where the Preston tube was being tested alongside static pressure taps beyond the 76% chordwise station, the plastic body would hang off the trailing edge to make the accommodation functional. The front flanges would still be taped to the surface as normal but a large section of tape would be applied over the top of the plastic body and wrapped around to the underside of the wing model. This process quickly proved easy to setup and just as secure as any other position's normal setup.

Chapter 11

RESULTS & ANALYSIS

11.1 Infrared Thermography Testing

Following the processes outline in Section 10.3, infrared testing was performed on the wing model at multiple pitch angle configurations. This testing was performed before the vinyl wrap was cut to expose the static pressure taps, allowing infrared imaging to occur through the entire span of the aluminum center section. The pre-marked angles from -2^{o} to 2^{o} were the only pitch range where boundary layer transition could be visualized. Any angle exceeding 2^{o} appeared to be fully turbulent while any angle below -2^{o} appeared fully laminar.

The pitch angles where boundary layer transition was visible were between 0^{o} to 4^{o}. This was due to the discovery that the geometric angle of attack was not equal to the effective aerodynamic angle of attack experienced by the airflow over the model. For reference going forward, all infrared images shown in this section have annotations marking the effective aerodynamic angle of attack and not the geometric angle. Figure 97 below shows the image taken during the 0^{o} effective aerodynamic angle testing, where boundary layer transition appears to begin around the 0.75 x/c location. This agrees strongly with the original design predictions for the airfoil profile used by the model.

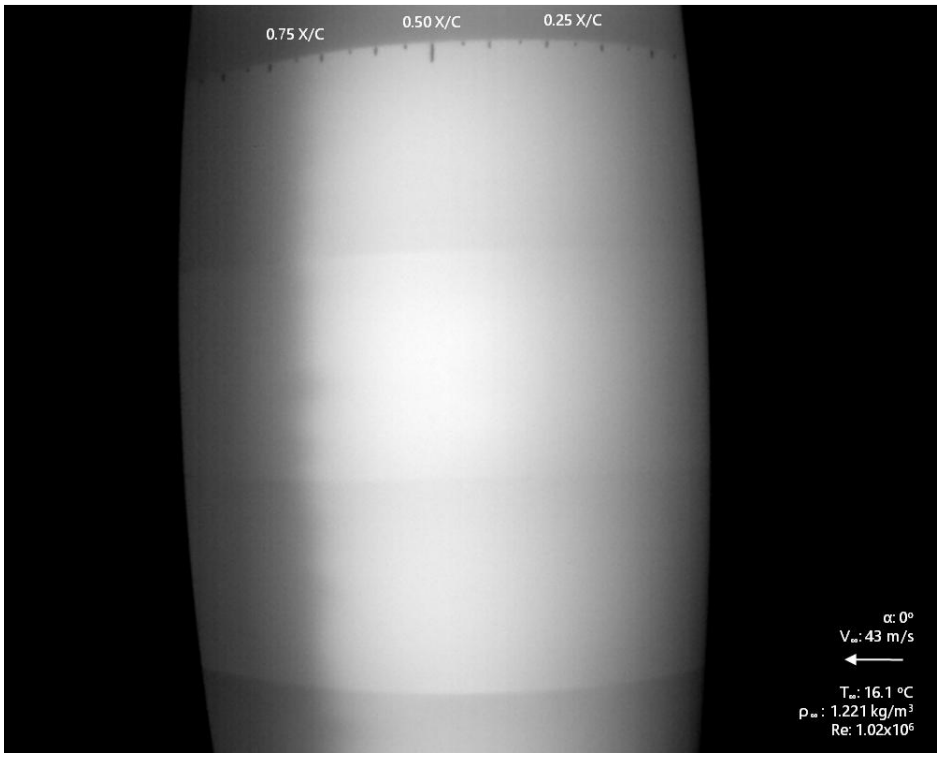

Figure 97: Infrared Thermographic Image of the Wing Model at an Effective Aerodynamic Pitch Angle of 0^o.

Based on the observations made with the infrared camera, three separate pitch angles were selected to become the baseline for analysis throughout this thesis testing: 0^o, 2^o & 4^o. Those values are listed as the effective aerodynamic angle, not the geometric angle. The reason those were selected was due to the ability to visualize a distinct shift in the onset of boundary layer transition between the three configurations. This fulfilled the primary testing goal of this research regarding the use of infrared thermography on the wing model. Figures 98 and 99 below show the image results for the 2^o and 4^o configurations which suggest the onset of transition occurs at 0.40 x/c and 0.15 x/c respectively. The turbulent wedge seen in the images directly correlates to the deformity within the vinyl layer, as shown in Figure 71 prior.

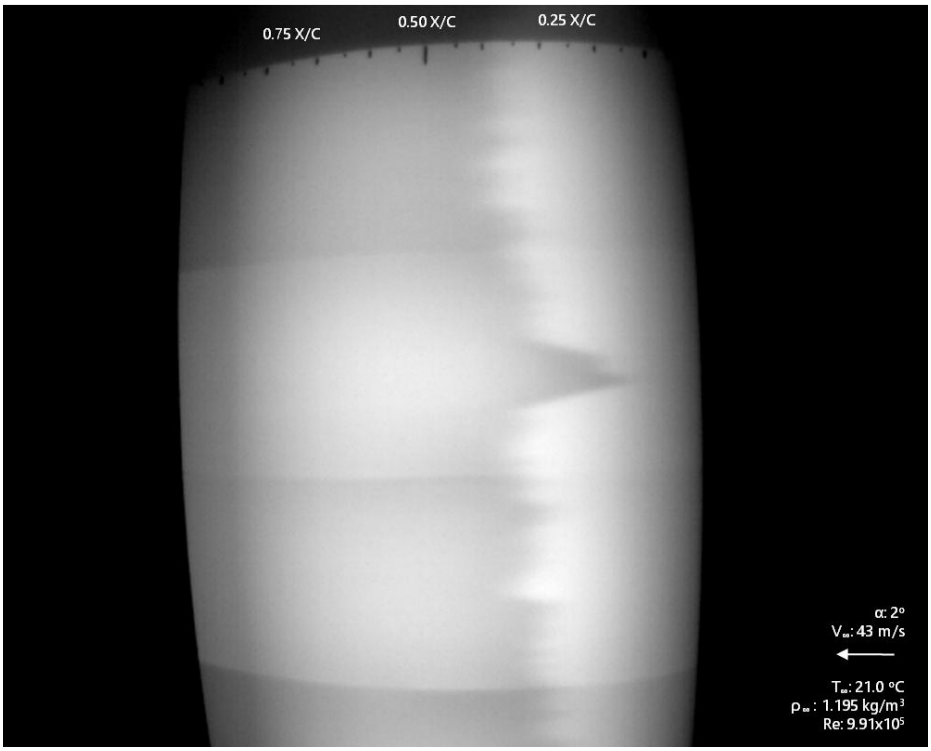

Figure 98: Infrared Thermographic Image of the Wing Model at an Effective Aerodynamic Pitch Angle of 2^{o}.

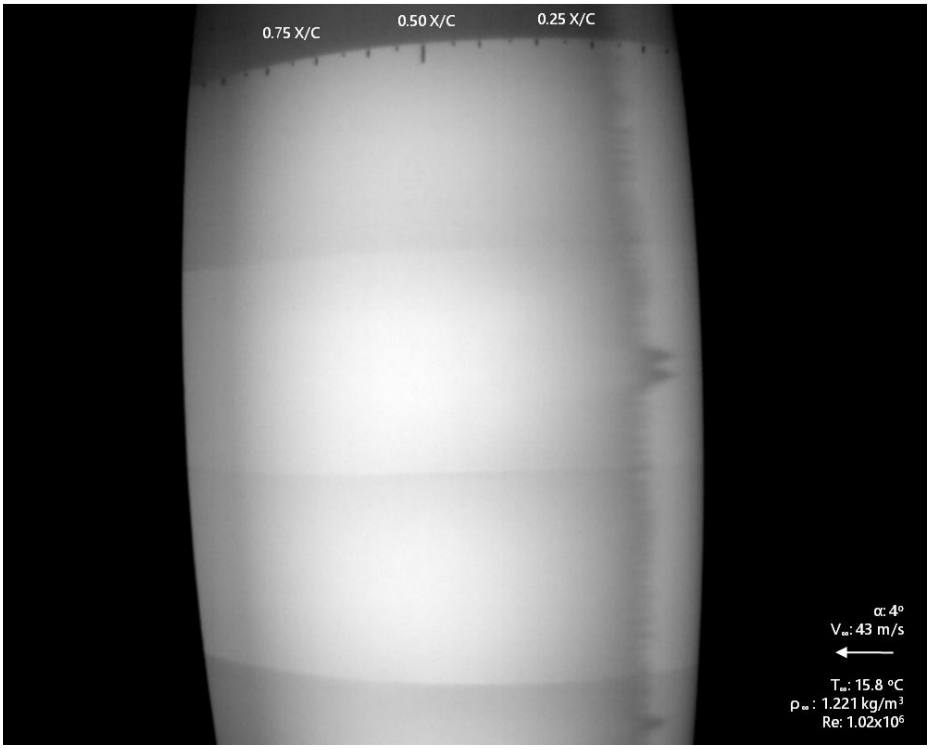

Figure 99: Infrared Thermographic Image of the Wing Model at an Effective Aerodynamic Pitch Angle of 4^{o}.

11.2 Static Pressure Distribution

Pressure testing was performed on the wing model for each increment of pitch angle shown in Section 11.1 prior. All the data for the static pressure distribution and Preston Tube was done angle-by-angle. This was to ensure the model would always be in the exact same position for all data collected at that condition. The consequence of this approach was when the Cal Poly LSWT unexpectedly encountered mechanical issues during the onset of the 4^{o} pitch angle testing. As a result, the data for the third condition could not be collected within the time frame of this research and is not discussed in the following sections.

Before implementing the Preston Tube setup, the wing model was tested at its design velocity of 40m/s to gather data on the static pressure distribution along its surface. This was measured from the central two rows of static pressure taps (Rows 2 and 3) using the methodologies outlined in Section 11.4. The data presented in Figures 100 and 101 below show the comparison of the experimental data to the numerical CFD predictions (reference Section 6.2). Coefficient of Pressure values were calculated using Equation WW, where the velocity value was collected through the pressure differential measured by the pitot-static probe and density from the digital weather station located in the lab's control room.

$$C_p = \frac{p_s - p_\infty}{\frac{1}{2}\rho V^2} \tag{4}$$

Each experimental data point is the average value taken between the two taps in Row 2 and Row 3. An exception was set for Taps 6 and 8, where that location was only functional with one of the rows and thus was not averaged.

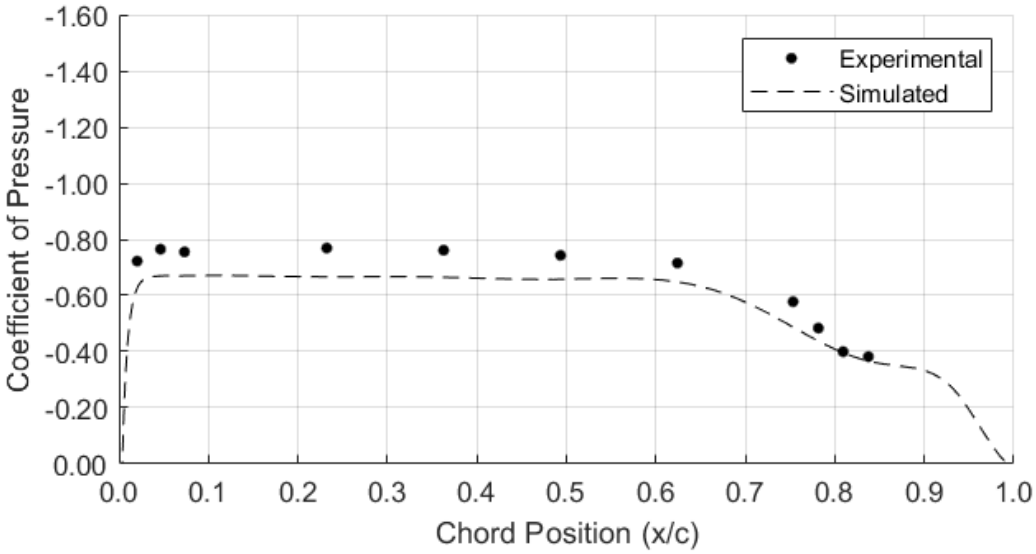

Figure 100: Distribution of Coefficient of Pressure Along the Upper Surface of the Wing Model at an Effective Angle of Attack of 0^{o}.

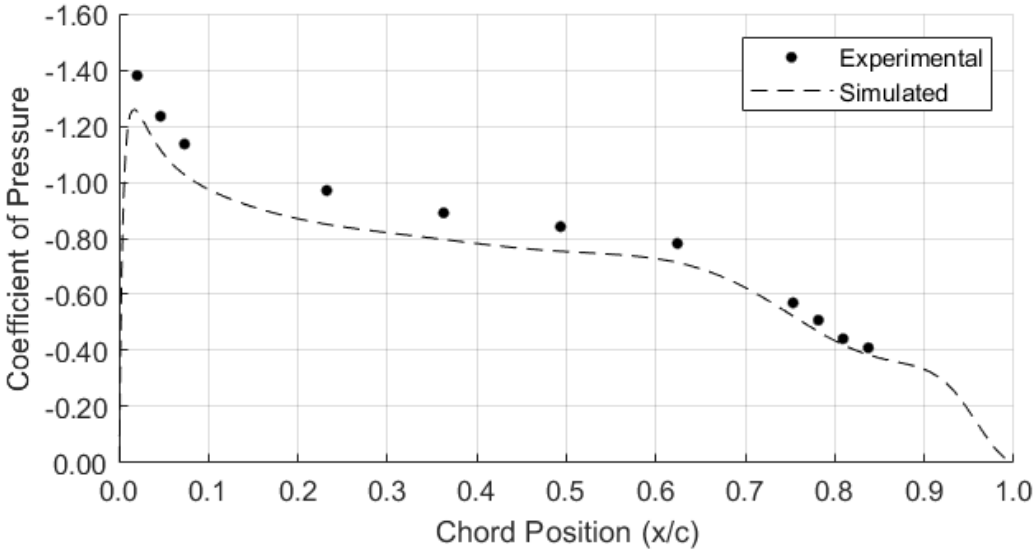

Figure 101: Distribution of Coefficient of Pressure Along the Upper Surface of the Wing Model at an Effective Angle of Attack of $+2^{o}$.

The data presented from the static distribution testing shows a strong and reassuring agreement with the numerical predictions. The use of the pitot-static probe (reference Section 11.2) generated a large improvement in aligning the experimental and numerical data together. The relative distribution of pressure from tap-to-tap is near exact to the predicted values. The

increased magnitude of suction was expected to be a result of two factors. The first being the static reference, despite the improvement from the pitot-static probe, which was still not an ideal far-field representation of what was generated in CFD. The second reason, as visualized in Section 9.2.1, the airfoil profile of the model is not exact to the design expectations and was expanded slightly in camber during the manufacturing process. The added camber from this result was expected to increase the degree of suction generated by the wing model, correlating to the results visualized in the aforementioned data.

The use of the pitot-static probe shown in Figure 94 helped reduce the magnitude of offset between the experimental measured data and the numerical simulated prediction. Figure 102 below visualizes a comparison of the data with and without the use of the pitot-static probe. The open-colored points were calculated using the static taps at the inlet of the tunnel test section while the solid-filled points used the static measurement of the floor mounted pitot-static probe. The comparison is shown for both pitch angles reviewed in the previous section.

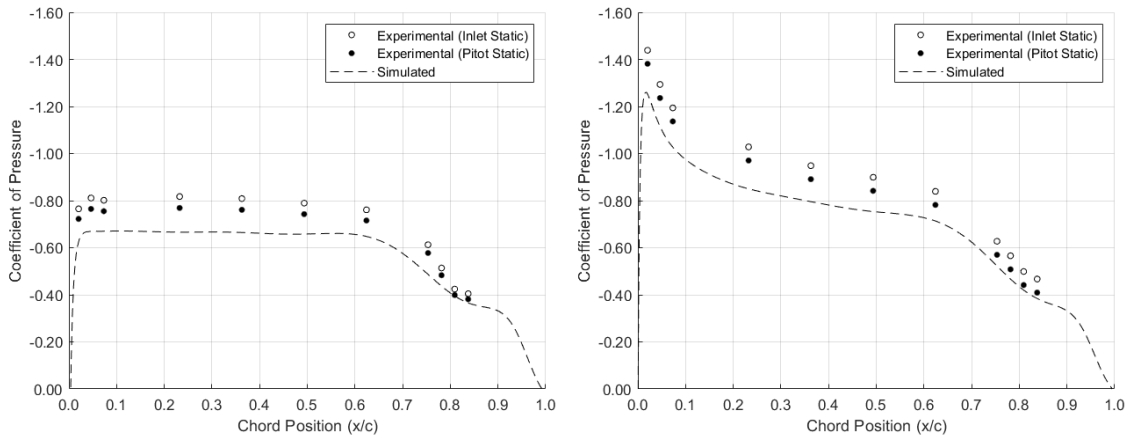

Figure 102: Comparison of Data Using Static Pressure References from the Wind Tunnel Inlet Versus the Floor Mounted Pitot-Static Probe at 0^o (Left) and 2^o (Right) Effective Angle of Attack.

11.3 Estimating Local Skin Friction Coefficient

Through the use of the Preston tube shown in Section 10.5, data was able to be collected for the model to estimate the local skin friction coefficient distribution. Data was collected for the wing model at both the 0^o and 2^o effective aerodynamic pitch angles where the Preston Tube was

traversed at each of the upper 11 functional static tap locations. Each position of the probe resulted in its own set of data being recorded, where only the pressure values for the Preston tube and corresponding static tap were reduced. The probe was only traversed along static row 2, since prior testing showed that rows 2 and 3 read values within 1% of each other. For the non-functional tap on row 2, the static pressure was measured from row 3 instead.

All data collected was processed through both the laminar boundary layer assumptions [16] as well as the turbulent boundary layer assumptions [15]. The process of equations used to perform the laminar calculations is shown in Equations 5 – 7 while the turbulent calculations are shown in Equations 8 – 10. All values for local wall shear stress (τ_w) were processed through the same calculation, Equation 11, which non-dimensionalized the value using the free stream total pressure with the static pressure measured on the model's surface.

$$x^*_{laminar} = \frac{(P_{total,surface} - P_{static,surface})d^2}{4\rho\nu^2} \tag{5}$$

$$y^*_{laminar} = 1.104(x^{*\,1/2}_{laminar}) - 1.896(x^{*\,-1/2}_{laminar}) \tag{6}$$

$$\tau_{o,laminar} = \frac{4y^*_{laminar}\,\rho\nu^2}{d^2} \tag{7}$$

$$x^*_{turbulent} = log_{10}\left(\frac{(P_{total,surface} - P_{static,surface})d^2}{4\rho\nu^2}\right) \tag{8}$$

$$y^*_{turbulent} = 0.8287 - 0.1381x^*_{turbulent} + 0.1437(x^*_{turbulent})^2 - 0.0060(x^*_{turbulent})^3 \tag{9}$$

$$\tau_{o,turbulent} = \frac{410^{y^*_{turbulent}}\,\rho\nu^2}{d^2} \tag{10}$$

$$C_{f,local} = \frac{\tau_w}{P_{total,pitot} - P_{static,surface}} \tag{11}$$

In order for the equations presented above to be valid, based on the assumptions by which their original authors derived them from, a conditional check was applied to see what experimental data fell within the acceptable range. Equations 12 and 13 present the conditions which allowed the laminar assumptions to remain valid, while Equation 14 presents the

alternative for the turbulent assumptions. The non-successful matching of a data point to the assumptions were expected to be a result of probe diameter over-sizing or the break-down in functionality of the system when encountering strong pressure gradients. Those are simple theories which were not tested further within this project but could be explored more in future endeavors which seek to implement a system of this type.

$$x^*_{laminar} > 0.033\left(\frac{dU_e}{\nu}\right)^2 \tag{12}$$

$$U_e = \sqrt{\frac{2(P_{total,pitot} - 2_{static,pitot})}{\rho}} \tag{13}$$

$$1.5 < y^*_{turbulent} < 3.5 \tag{14}$$

The results of the aforementioned calculations results in the correlations shown in Figures 103 and 104. Each plot—one per pitch angle tested—contains the data for all chordwise stations analyzed through the laminar and turbulent boundary layer assumptions. Each data point is set to visualize whether or not it passed the conditional checks required for the assumptions to be valid; a solid-filled point means it met the criteria whereas an open-filled point did not. The CFD data from Section 6.3 is also overlaid on each plot, to compare the experimental data with the numerical predictions for both laminar and turbulent modeling assumptions.

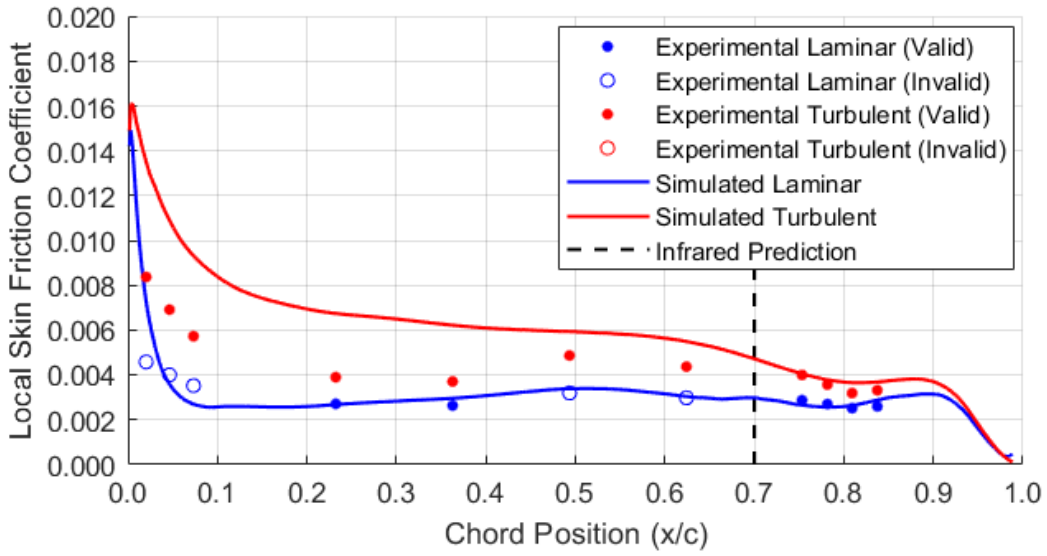

Figure 103: Distribution of Local Skin Friction Coefficient Along the Upper Surface of the Wing Model at an Effective Angle of Attack of 0^{o}.

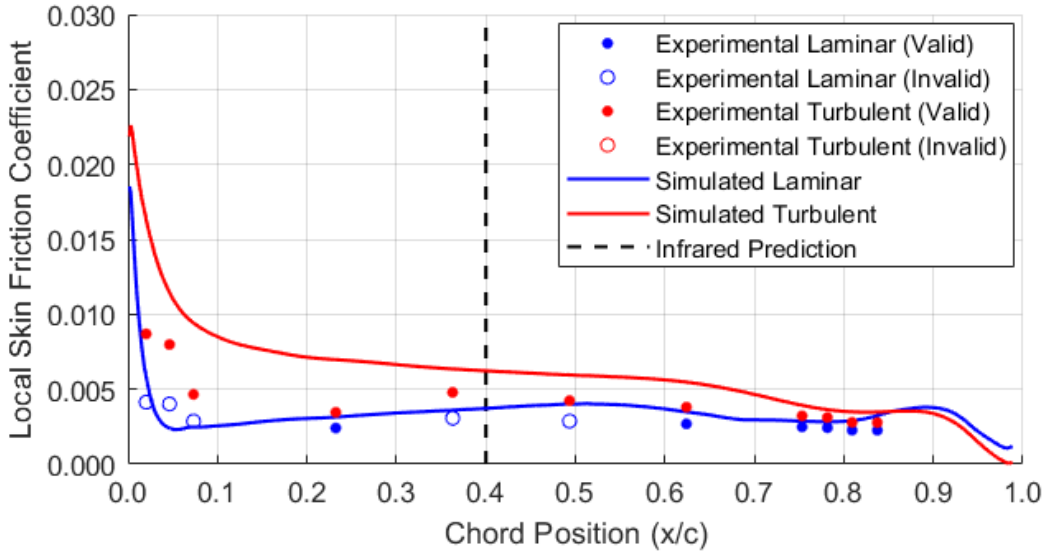

Figure 104: Distribution of Local Skin Friction Coefficient Along the Upper Surface of the Wing Model at an Effective Angle of Attack of 2^{o}.

The purpose of this testing was to use the numerically-simulated data as a reference for the experimental data, visualizing where the measured points along the model show correlation with one versus the other. For the 0^{o} case, the infrared thermography tests suggested boundary layer transition to occur around 0.70 x/c. The measured points, with both the laminar and

turbulent boundary layer assumptions, all show stronger correlation to the laminar numerical distribution. After the 0.70 x/c point, the measured data with the turbulent assumption starts to match the turbulent numerical data. While just a quantitative analysis, it ultimately fulfills the goal of the using the Preston Tube in this situation—confirmation of infrared results rather than precision value measurement. The 2^o case produces a similar suggestion to the 0^o case, although the low-confidence laminar numerical results make the conclusion a bit more obscured.

It should be heavily emphasized that the quality of the CFD data used to compare the Preston Tube results placed a large inhibition to the interpretation of the outcomes. In order for the Preston Tube measurement process to work properly, comparison to accurate and high-confidence CFD data is vital. However, the numerical setup used for this project was unable to readily provide that level of desirability in the skin friction coefficient predictions. That was acceptable for the scope of this project since the data acquired—both experimental and numerical—was still able to suggest correlation as desired. Future work which seeks to expand upon the use of the Preston Tube should take note in employing a more robust numerical system up front to avoid the issues encountered by this project.

11.4 Miscellaneous Infrared Imaging

Due to the simplicity of the infrared testing process when performed with the wing model, additional tests were performed throughout the course of this research. These few tests were setup to check for the quality of flow along the surface of the model as various imperfections or objects were added. While the results are informal relative to that detailed prior in this chapter, they helped to build confidence in the idea that this wing model was capable of generating and measuring laminar boundary layer flow.

The first check performed was done using a trip dot. This trip dot was far-oversized for the boundary layer developed on the wing and would create a larger disturbance in the flow beyond only forcing transition. It was placed in between the leading edge and the visualized location of natural transition onset. Figure 105 visualizes the result that was captured. The influence of the trip dot was seen accelerating boundary layer transition around itself, as

evidenced by the grey-cold color gradient around and behind the object. In addition, the feature of separation can also be seen in between the aft face of the trip dot briefly before the darker-shaded region trails behind. The two noticeable color intensities behind the trip dot represent where the protrusion generated a separated, turbulent wake within the otherwise lower-intensity transitioned boundary layer flow.

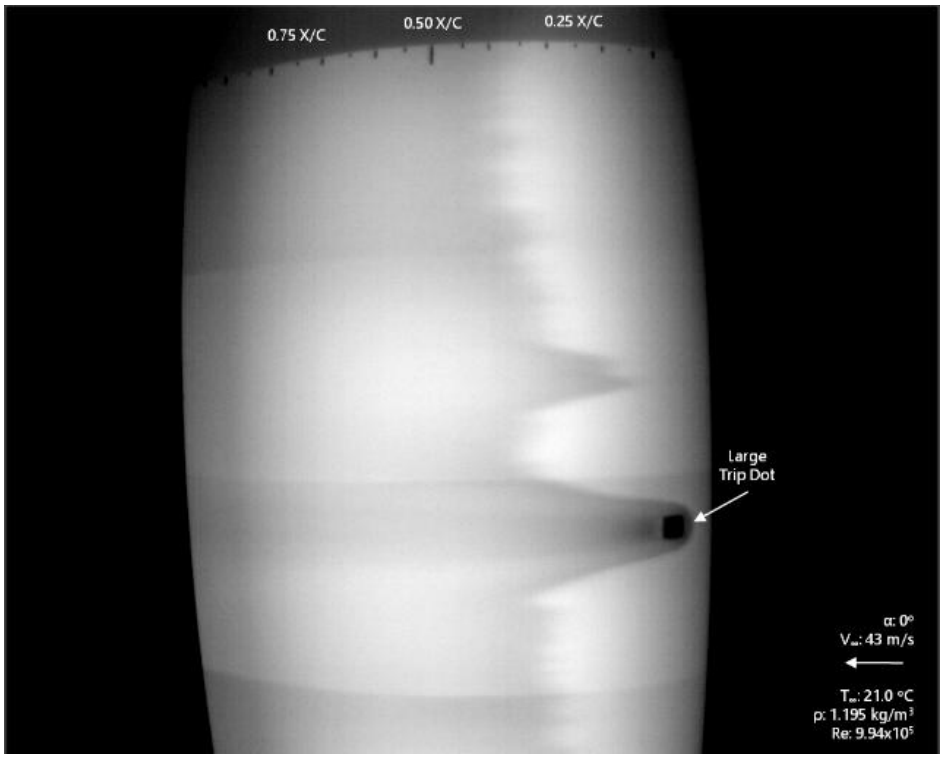

Figure 105: Infrared Image of the Wing Model with the Trip Dot Added to the Upper Surface.

Prior to use of the model's pressure measurement system, an additional test was performed which checked for the influence of the Preston Tube on the boundary layer flow. The following image (Figure 106) suggests that the instrument only forces boundary layer transition where the plastic body is located. The stainless steel tube, which lies within the height of the boundary layer and samples the total pressure at the surface, did not appear to forcefully transition the boundary layer. The turbulent wake generated by the bluff body is also visible in Figure 106 akin to the trip dot in Figure 105. This result was reassuring in minimizing the concern of the probe's design influencing the state of the boundary layer too much to properly use.

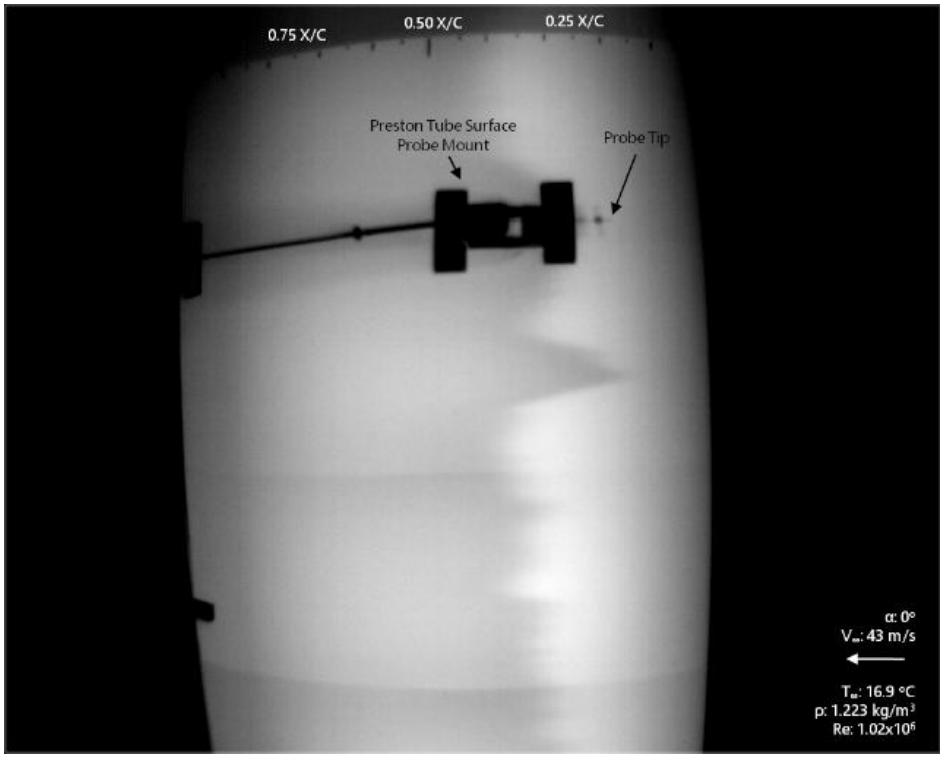

Figure 106: Infrared Image of the Wing Model with the Preston Tube On the Upper Surface Forward of Transition Onset (Left) and Behind Transition Onset (Right).

Once the two strips of the vinyl outer layer were removed prior to pressure testing, it was unknown whether the surface of the aluminum would be smooth enough to support laminar flow. In addition, the removal of the vinyl also imposed the risk of uncovering scratches or imperfections in the metal which could prematurely force boundary layer transition. As such, another quick infrared test was performed after removing the vinyl strips to check the quality of flow afterwards. While the bare aluminum could not be visualized with infrared thermography directly—due to the removal of the vital insulation layer—the quality of flow at the edges of the cut region would be enough of an indication nonetheless. In Figure 107, the gradient line which was expected to correlate with boundary layer transition appears to travel along the span of the model just the same as it did before the vinyl was removed (reference Figure 78). Should the exposed aluminum be prematurely forcing transition, the propagation of disturbed flow along the chordline would impinge on the nearby vinyl-covered area. Without seeing that effect, there was no discernable concern for the quality of the aluminum surface to support laminar flow.

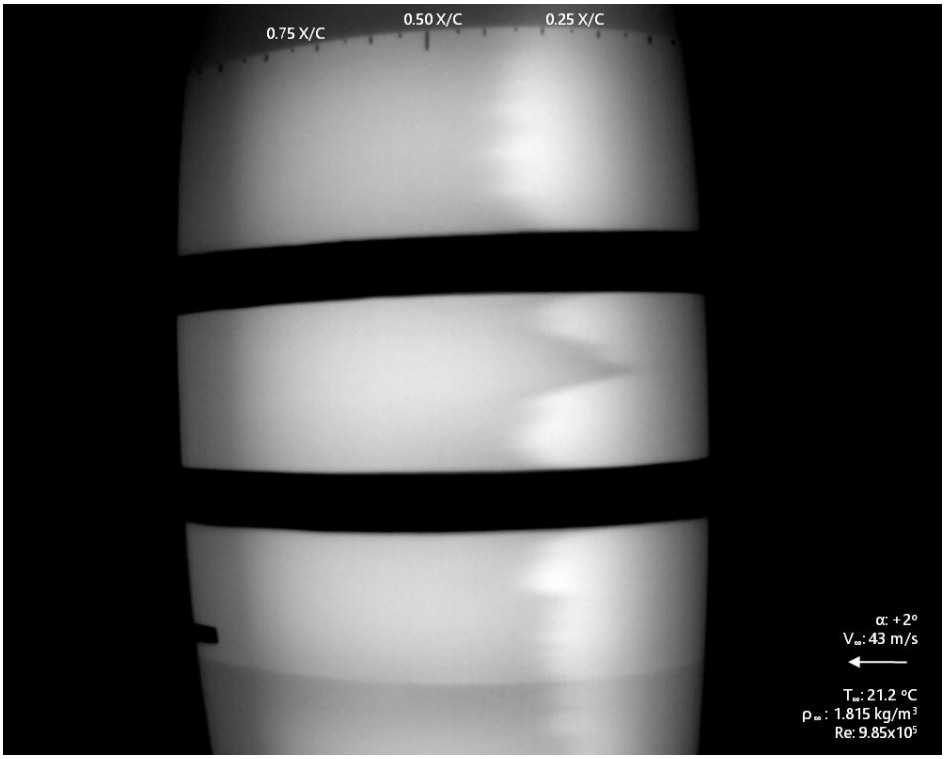

Figure 107: Infrared Image of the Wing Model with the Two Strips of Vinyl Cut to Expose the Pressure Taps.

Chapter 12
CONCLUSION

The infrared wing model was the next step in expanding that legacy of knowledge for the practical usage of infrared thermography at the Cal Poly LSWT. Using materials and instrumentation common to the Cal Poly LSWT, a model was designed and developed which could reliably measure boundary layer transition in low speed testing conditions. The all-aluminum body, outfitted with internal silicon-rubber heating elements and a vinyl wrap exterior layer, was able to produce the thermal conditions for successful infrared thermography to occur. The selected heating method allowed for a uniform and easy-to-operate means of pre-heating the model and generating the temperature differential which could correlate a distinction between laminar and turbulent boundary layer flow.

Natural boundary layer transition was visualized by the infrared camera on the suction side of the wing model and seen shifting in chordwise location as the pitch angle was varied. Static pressure taps on the surface, sized and installed to avoid premature boundary layer transition, measured a pressure coefficient distribution with strong agreement to numerical simulation expectations. From there, a Preston Tube system was implemented to sample the flow characteristics of the internal boundary layer flow. Skin friction coefficient values interpolated from published empirical relations were coupled with numerical simulation expectations to suggest the onset of boundary layer transition in agreement with the infrared images taken prior.

With the model successfully fulfilling the research objectives outlined by this thesis, it will continue its life through another infrared thermography testing campaign which heavily influenced the design and preparation phase all the way through. Overall, the wing model was able to demonstrate and expand upon the practical knowledge of low-speed wind tunnel-based infrared thermographic testing.

Chapter 13

FUTURE IMPACT

The origin and primary motivation of this research was to expand the knowledge of infrared thermography within the practical context of the Cal Poly LSWT. Many aspects of this model's design and experimental setup sought to incorporate on the lessons learned from prior tests in addition to expanding upon some vacancies in knowledge that were yet to be solved. The successful development and testing of the wing model helped to expand on two core areas of the infrared thermographic process: rapid, uniform heat application as well as results validation. The information which was gained in those two areas created a stronger foundation for future infrared projects at Cal Poly. Other practical gains—specifically from the manufacturing phase—which were previously unknown or undocumented within the context of the Cal Poly LSWT will also provide useful legacy knowledge to future wind tunnel model developments.

The next step for the wing model is expected to follow shortly after the publication of this paper. As mentioned prior, the model was developed with two separate research scopes in mind, the second of which revolved around the swept angle testing. A goal for using the model for this research was that it could be tested and characterized to allow for a more efficient and productive testing process during the swept angle campaign. Based on the successful results and proof of effectiveness by the model for both infrared testing and pressure measurement, the swept angle testing can eventually commence with a much higher degree in results confidence than if the model were developed from scratch right before hand. This concept doubles back to the benefit of developing the model with mutual interest from Joby Aviation—such that the resources from each participant could benefit and raise the quality of work for the other.

There is also hope that this model, due to the versatility of its design and efficiency of operation, can find a long-term benefit through use in an undergraduate lab curriculum. Given all the time and monetary investment put forth into the model's development, it would be unfortunate to see it fall into disuse after fulfilling its original research objectives. A push has been made to integrate the model into the curriculum of the same undergraduate class which utilizes the other

infinite wing model; the one which had served as a ready point of inspiration many times throughout this research. Although the eventual fate of the infrared wing model is still uncertain, this research has ended with optimism that it can continue to provide and benefit the Cal Poly LSWT for many more years to come. Students looking to expand upon the research initiated by this project could benefit from more sophisticated development regarding the use of the Preston Tube to gather more accurate and confident data. Another option would be to explore the use of more sophisticated image processing techniques to expand on the quality and complexity of data which can be generated from infrared imaging techniques. Regardless of the idea pursued, the hope is that this research can carry onwards to provide a strong starting point for expanded research of all varieties and complexities through the future.

REFERENCES

[1] Crowder. “Infrared Cameras for Detection of Boundary Layer Transition in Transonic and Subsonic Wind Tunnels.” *AIAA 90-1450*, 1990.

[2] Garbeff & Baerny. “A Qualitative Investigation of Selected Infrared Flow Visualization Image Processing Techniques.” *AIAA Aviation Forum 2019-2907*, 2019.

[3] Garbeff & Baerny. “Recent Advances in the Infrared Flow Visualization System for the NASA Ames Unitary Plan Wind Tunnels.” *AIAA SciTech Forum 2017-1051*, 2017.

[4] Gebbink, Wang & Zong. “High-Speed Wind Tunnel Test of the CAE Aerodynamic Validation Model.” *Chinese Journal of Aeronautics 31(3): 439-447*, 2018.

[5] Goldstein. “Fluid Mechanics Measurements.” *Hemisphere Publishing Corporation*, 1983.

[6] Goodman, Lipford & Watkins. “Boundary-Layer Detection at Cryogenic Conditions Using Temperature Sensitive Paint Coupled with a Carbon Nanotube Heating Layer.” *MDPI Sensors 16 2062*, 2016.

[7] Hall. “Advances in Infrared Imaging Analysis Techniques for AEDC PWT/VKF Wind Tunnel Applications.” *AIAA 2018-4048*, 2018.

[8] Herbert. “Boundary-Layer Transition Analysis and Prediction Revisited.” *AIAA 91-0737*, 1991.

[9] Joseph, Borgoltz & Devenport. “Infrared Thermography for Detection of Laminar-Turbulent Transition in Low-Speed Wind Tunnel Testing.” *Exp Fluids 57:77*, 2016.

[10] Klein, Yorita & Henne. “Boundary Layer Transition Detection on Wind Tunnel Models During Continuous Pitch Traverse.” *AIAA 2019-1180*, 2019.

[11] Klein, Henne & Sachs. “Combination of Temperature-Sensitive Paint (TSP) and Carbon Nanotube (CNT) for Transition Detection.” *AIAA SciTech Forum 2015-1558*, 2015.

[12] Lillywhite. “Microphone-Based Pressure Diagnostics for Boundary Layer Transition.” *California Polytechnic State University – San Luis Obispo*, 2013.

[13] Minkina & Dudzink. “Infrared Thermography: Errors and Uncertainties.” *John Wiley & Sons*, 2009.

[14] Narashima. “The Laminar-Turbulent Transition Zone in the Boundary Layer.” *Progress in Aerospace Science, Vol. 22, pp. 29-80*, 1985.

[15] Patel. “Calibration of the Preston Tube and Limitations on its Use in Pressure Gradients.” *Journal of Fluid Mechanics, Vol. 23, Part 1, pp. 185-208,* 1965.

[16] Poll. “A Note on the Use of Surface Pitot Tubes for the Measurement of Skin Friction in Laminar Boundary Layers.” *Cranfield College of Aeronautics Report 8307*, 1983.

[17] Preston. “The Determination of Turbulent Skin Friction by Means of Pitot Tubes.” *The Journal of the Royal Aeronautical Society, Vol. 58, Issue 518, pp. 109-121,* 1954.

[18] Purser, Marzocca, Marino & Pook. “On the Use of Infrared Thermography for Boundary Layer Analysis.” *AIAA 2019-2104*, 2019.

[19] Raffel & Mertz. “Differential Infrared Thermography for Unsteady Boundary-Layer Transition Measurements.” *AIAA Journal, Vol. 52, No. 9*, 2014.

[20] Ricci & Montelpare. “A Quantitative IR Thermographic Method to Study the Laminar Separation Bubble Phenomenon.” *International Journal of Thermal Sciences 44, pp. 709-714*, 2005.

[21] Sant, Marchand, Millan & Fontaine. “An Overview of Infrared Thermography Techniques Used in Large Wind Tunnels.” *Aerospace Science and Technology 6, pp. 355-366*, 2002.

[22] Saric. “Physical Description of Boundary-Layer Transition: Physical Evidence.” *Special Courses on Progress in Transition Modeling 51*, 1994.

[23] Winstead, Cox. “The Design and Manufacture of an NACA 4412 Test Section.” *California Polytechnic State University San Luis Obispo*, 1993.